isvr Institute of Sound and Vibration Research

Investigation of an Electrodynamic Actuator for Self-Sensing Active Vibration Control

C. Paulitsch, P. Gardonio and S.J. Elliott

ISVR Technical Memorandum 917

August 2003

University of Southampton

SCIENTIFIC PUBLICATIONS BY THE ISVR

Technical Reports are published to promote timely dissemination of research results by ISVR personnel. This medium permits more detailed presentation than is usually acceptable for scientific journals. Responsibility for both the content and any opinions expressed rests entirely with the author(s).

Technical Memoranda are produced to enable the early or preliminary release of information by ISVR personnel where such release is deemed to the appropriate. Information contained in these memoranda may be incomplete, or form part of a continuing programme; this should be borne in mind when using or quoting from these documents.

Contract Reports are produced to record the results of scientific work carried out for sponsors, under contract. The ISVR treats these reports as confidential to sponsors and does not make them available for general circulation. Individual sponsors may, however, authorize subsequent release of the material.

UNIVERSITY OF SOUTHAMPTON

INSTITUTE OF SOUND AND VIBRATION RESEARCH

SIGNAL PROCESSING & CONTROL GROUP

Investigation of an Electrodynamic Actuator for Self-Sensing Active Vibration Control

by

C Paulitsch, P Gardonio and S J Elliott

ISVR Technical Memorandum N° 917

August 2003

Authorised for issue by
Prof S J Elliott
Group Chairman

ABSTRACT

Active vibration control with an electrodynamic moving coil type shaker at a single degree of freedom (SDOF) system is investigated theoretically and experimentally. By feeding back the integrated output signal of an accelerometer on top of the actuator direct velocity feedback is implemented. Then positive proportional current feedback is investigated by feeding back the voltage across an additional resistance in the electrical driving circuit of the shaker. Finally a bridge circuit is used to feed back only the induced voltage assumed to be proportional to the coil velocity. Velocity feedback measurements correspond well to simulations for small feedback gains and vibration reduction of up to 27dB is found. Proportional current feedback simulations show vibration reduction up to 8dB. Measurements and simulations correspond well for measurable frequency response functions (FRF). Induced voltage feedback simulations indicate that self-sensing may realize vibration reduction similar to velocity feedback if the complex electrical impedance of the shaker is compensated for. In experiments, however, only partly compensation could be realized due to the specific electromagnetic actuator design leading to a reduction at the measurable FRF of about 16dB. Moreover in order to check vibration reduction for proportional current and induced voltage feedback experimentally, a separate primary source is needed.

INDEX

1. INTRODUCTION page 1

2. FREQUENCY DOMAIN MODEL OF THE SELF-SENSING ACTUATOR 7
   2.1 Actuator model 9
   2.2 FRFs of the mechanical, electrical parts and the electromagnetic coupling 11

3. COMPARISON OF MEASURED AND SIMULATED OPEN LOOP ELECTRICAL AND MECHANICAL FREQUENCY RESPONSE FUNCTIONS 17
   3.1 Measured and simulated mechanical frequency response function with short-circuited electrical part 19
   3.2 Measured and simulated electrical frequency response function without primary force excitation 21

4. MEASURED VELOCITY FEEDBACK CONTROL 23
   4.1 Stability and simulation of the feedback control system 23
   4.2 Implementation of velocity feedback control 27

5. CURRENT FEEDBACK CONTROL 29
   5.1 Proportional current feedback theory 29
      5.1.1 Limitations to proportional current feedback 30
      5.1.2 Closed loop simulations 32
      5.1.3 Explanation by the root locus 35
   5.2 Implementation of proportional current feedback control 37

6. INDUCED VOLTAGE FEEDBACK CONTROL 40
   6.1 Induced voltage feedback theory 40
      6.1.1 Limitations to induced voltage feedback 42
      6.1.2 Stability 45
      6.1.3 Closed loop simulations 47
      6.1.4 Explanation by the root locus 50
   6.2 Implementation of induced voltage feedback control 52

7. CONCLUDING REMARKS 59

8. REFERENCES 60

APPENDIX A: Accelerometer response 64
   A.1 Resonant and passive effect of the accelerometer on the electrodynamic system 64
   A.2 Relative displacement as measured system output 67
   A.3 Accelerometer measurement function 68
   A.4 Electrical FRF with accelerometer 68

APPENDIX B: Higher frequency effect at identified electrical FRF 70

1. INTRODUCTION

Vibration control of mechanical structures or machines is important in many fields since excessive vibrations may harm operators, machines and the environment. Legislation and customers' demand make vibration control a necessary feature of more and more applications. In factories and plants noise and vibration impact of machinery on the environment has to be minimized. Also, sensitive equipment has to be protected from ground vibration or other sources of vibration in the plant. In transportation vehicles comfort is improved by reducing vibration and noise disturbances on passengers. Furthermore in order to reduce their impact on the environment noise emission from vehicles has to be reduced. Finally domestic appliances may exhibit a large degree of noise and vibration that also has to be controlled.

There are three ways of improving noise and vibration insulation of structures and machines. First by reducing the sources of noise and vibration, second by acting on the transmitting paths with passive isolation or insulation treatments and third by modifying the receiver system or the radiating elements. Active control means can be implemented in all three stages. For example active bearings could be used to reduce excitations generated by unbalanced high-speed rotors [1]. Active mounts might be used to enhance low frequency isolation of machinery from the basement structure [2, 3]. Active vibration systems could be employed to reduce the structure-borne path in truss structures [4]. Finally active structural acoustic control systems such as smart panels with single input single output (SISO) [5] and multiple input and multiple output (MIMO) [6] vibration control systems could be used to minimize sound radiation of enclosures or partitions.

In general, as discussed for instance in [7], passive vibration control consists of mass and stiffness treatments that do not dissipate vibration energy and damping treatment where vibration energy is lost to the dynamic system through dissipation. Stiffness treatments are effective at relatively low frequencies, however, they require modification of the vibrating system, which is usually impossible without a costly redesign, and in most cases they lead to increased weight due to additional stiffening elements. Additional masses are especially efficient in the high frequency region when mechanical vibrations can be considered as waves. Passive damping elements increase dissipation of vibration energy, but system weight is increased.

Vibration isolators provide good reduction of vibration transmission from one system to another. However, in order to be effective the mounting system must be very soft, and this often is in contrast with the static constraints imposed by the operation of the mechanical part to be isolated [2]. Moreover a new set of low frequency resonances of the mounted system are introduced [8], which degrades low frequency vibration isolation. Increasing the damping effect in the mount could reduce the amplitude of these resonances, but this automatically enhances higher frequency vibration transmission [3].

Finally vibration absorbers or neutralizers could be used to reduce narrowband vibration generation or transmission by tuning the anti-resonance of an additional mechanical system to a resonance of the vibrating structure [9].

Active control systems are used in parallel to or as substitution of passive means, particularly in order to improve low frequency structure-borne sound generation, transmission or

radiation. For instance active vibration systems using inertial actuators could be used to influence vibration generation mechanisms or to reduce vibration of the receiving structure [10]. Active isolators might also be added in parallel to passive mounting elements in order to enhance isolation effects and reduce the amplitudes of the low frequency resonant modes of the mounted system [11]. Finally smart beams or smart panels with integrated actuators and sensors could be used to reduce structure-borne sound transmission of truss structures or noise radiation of enclosures or partitions [12].

In general active control architectures can be divided into two families: feedforward and feedback control systems [13]. Feedforward control schemes are particularly suited for the control of tonal disturbances that are usually identified by a reference sensor. Feedback control architectures do not use reference sensors and are especially advantageous at broadband excitation.

Up to present only SISO feedback control systems have been developed in practice for the solution of particular problems [14] as for example the control of low frequency noise propagation in ventilation ducts [15] or low frequency noise insulation in headsets and headrests [16]. Currently, commercially available active headsets use an analogue feedback control system with a collocated error microphone and loudspeaker actuator for the low frequency noise reduction that could not be controlled by the headset shells only. Also, Active Noise Control (ANC) systems for the reduction of cabin noise in propeller aircrafts have been developed [17]. In this case a MIMO feedforward control system is used where a tonal reference signal is taken from the rotor of the propeller and a relatively large number of control loudspeakers and error microphones are connected. Thus these systems are not suited for controlling wide band excitation and moreover they are affected by a number of drawbacks. Firstly they require a costly and delicate multi-channel controller. Secondly they require a lot of wiring, actuators and sensors, which implies weight, reliability and installation problems. Thirdly MIMO feedforward control systems are sensitive to failures of any single sensor or actuator component so that the controller is constantly updated based on all sensor signals in order to avoid instabilities. Finally due to their complexity multi-channel controllers are usually implemented using digital signal processors (DSP), which limits the control bandwidth because of the time needed for sampling and calculation [18].

As a result during the past ten years scientists have begun to develop Active Structural Acoustic Control (ASAC) systems where structural sensors and structural actuators are embedded on partitions in order to control sound transmission. Initially feedforward control systems measuring a reference signal at the noise source were used to drive the structural actuator to minimize sound radiation into the interior of an enclosure. Therefore systems were still limited to the control of tonal disturbances. However in parallel researchers have also developed feedback control systems where the signals from structural sensors are fed back to the structural actuators in such a way as to minimize the vibration component that contributes to the sound radiation. This has led to the design of relatively complicated multichannel feedback controllers using state space design [6, 19]. Two interesting alternative approaches have been proposed more recently.

The first one uses distributed sensors and actuators that enable control of the principal low frequency radiating components of the panel vibration [20]. In this case it is possible to implement a SISO feedback control system using the classic feedback control design theory

(Nyquist criterion, root locus criterion and frequency domain design). The main problem encountered with this type of system is the design of suitable sensor-actuator pairs for the implementation of ASAC and also a stable feedback control system with a sufficient bandwidth as highlighted in [5, 21].

The second type uses a large number of collocated sensor-actuator systems acting independently from each other with localized feedback control loops [22]. Each control unit implements direct velocity feedback control in such a way as to provide active damping of the panel so that its vibration and sound radiation at resonance is reduced. This arrangement has given very interesting initial simulation results especially for point force actuators that could result in sound reductions of several dBs if the individual control unit is stable. In order for the individual SISO velocity feedback control unit to be unconditionally stable the sensor actuator transfer function must be positive real. This is theoretically guaranteed by collocated and dual sensor-actuator pairs i.e. actuation and sensing must be connected to the same degree of freedom (DOF) of the system to be controlled [23] in the same way [24]. For example even a shaker velocity sensor pair does not give a truly collocated response function as at higher frequencies sensor dynamics interfere. A possibility to obtain better collocation and duality properties could be given by self-sensing actuation.

In self-sensing actuation self-sensing actuators or sensoriactuators sense and act on the same mechanical DOF. Depending on reciprocity many transducers may be used either as sensor or actuator as observed for instance by [25], whereas usually they are designed to be efficient for one function only, the other being a disturbance usually minimized. Several different transducer types based on the magnetostrictive or piezoelectric phenomena have been investigated for their use as sensoriactuators for instance by [26, 27, 28]. Magnetic bearings have also been investigated for instance by [29] to become self-sensing, thus eliminating a special sensor for the rotor position. But also sensorless electric motors can be seen as electrodynamic sensoriactuators where the current is used to obtain information about the motor rotational speed as for example in [30]. Loudspeakers are a popular example for linear, electrodynamic actuators where self-sensing is used to increase damping. In general additional potential advantages of self-sensing actuators for practical applications are the reduced number of transducers, amplifiers and cables, reduced size and reduced risk of failure.

A first widely studied example of sensoriactuators are piezoelectric patches that are used to apply and sense a moment [13] on the structure. There are passive, semi-active and several active ways to influence the structural vibration by piezoelectric sensoriactuators. It has been shown [31] that by adding a passive electrical resistance across the connections of the piezoelectric patch the stiffness of the attached structure is changed. Additionally when manually tuning an electrical inductance in series to the resistance to an optimal value so that it resonates with the natural frequency of the structure passive damping is added at this first natural frequency of an attached cantilevered beam. Using active components to manually tune the inductance this circuit has been applied to the damping of space structures [32]. For the damping of multiple structural resonance frequencies a digital implementation of multiple resonant inductors is more convenient [33]. Additionally a bridge circuit can be used to measure the strain or strain rate using the piezoelectric patch as a true sensoriactuator [34, 35]. Then by feeding back the strain rate damping is added to the mechanical stucture. Due to the balancing problems mentioned in [35] and in order to reduce power requirements [36] semi-

active algorithms have been investigated that actively adapt electrical bridge parameters [37, 38, 39]. Obviously the adjustment of the bridge can be avoided by using separate closely located patches used as actuator and sensor, but perfect collocation is not obtained [40]. An active solution for the balancing problem is to use robust design techniques incorporating parameter changes in the controller design [41]. Finally instead of using positive electrical parameters a negative capacitance amplifier cancels the internal capacitance of the piezoelectric patch [42, 43, 44] so that only the induced signal remains that can be fed back or dissipated over an additional resistance. Once the negative capacitance amplifier cancels the inherent, piezoelectric capacitance over a broad frequency band no electric parameter needs to be tuned to a resonance frequency of the structure so that broadband control is realised. Technically the negative capacitance circuits used are not much different from a bridge circuit with feedback that is interpreted as a negative impedance amplifier [44] or analogue electronics of the Riordan-type are used [43, 45].

As a second example for self-sensing actuators electrodynamic, linear self-sensing actuators apply a point force on the structure and it has been found in [22] that force actuators give better results for ASAC with a multitude of local sensor-actuator pairs than piezoelectric patches. Additionally electrodynamic actuators are more suitable for the control of low frequency vibration as piezo actuators tend to excite high structural modes more efficiently [20]. Self-sensing, electrodynamic force actuators are particularly advantageous when the induced voltage is proportional to the velocity of the mechanical system. Then feeding back their output should be similar to direct velocity feedback resulting in active damping. Other sources of instability such as non-ideal integrators for accelerometers or differentiators for displacement sensors are thus avoided. Electrodynamic self-sensing has been studied for active vibration damping at disk drives [46], high-speed elevators [47], for shunt damping [48], viscosity measurements [49] and extensively at electrodynamic loudspeakers. At this application a signal proportional to the coil velocity has been used to dampen the first mechanical natural frequency. Thus mainly low frequency loudspeaker behaviour is influenced only.

The estimation of the loudspeaker coil velocity by measuring the induced voltage was studied first using a Wheatstone bridge [50]. When feedback of the induced voltage was used to influence the mechanical low frequency behaviour of the loudspeaker the coil inductance usually was neglected [51, 52]. Therefore the necessary balance of the Wheatstone bridge was simple in theory [51], but it was usually restricted to the low frequency region. The upper frequency loudspeaker behaviour was controlled using inductors and capacitors in the bridge circuit [53, 54] in order to improve directly the pressure response rather than the intermediate coil velocity response. But in some cases "in the actual application of the bridge [improving the bridge balance by adjusting of the accessible bridge elements] cannot be applied [...] because the amplifier's internal resistance R_i comes in parallel with the bridge, thus spoiling the correction" [51 p.21].

The adjustment problem can be avoided by feeding back the voltage induced in an additional coil mechanically linked to the primary coil as proposed by [55, 56] since then no compensating bridge circuit is necessary. If the magnetic field of both coils is strongly interacting the resulting transformer coupling also noted by [52] can then be compensated by using an additional analogue circuitry [57]. Alternatively an additional sensor on top of the loudspeaker is used for instance by [58, 59].

Another solution that even benefits from the apparent amplifier resistance R_i is proposed by [60, 61] where a negative output impedance amplifier [62, 63, 64] is used that cancels the internal loudspeaker impedance so that only the induced motional voltage is used for generation of the secondary force. A negative output impedance amplifier can be realised by designing an additional bass compensation stage [73], by mounting the loudspeaker in a bridge circuit [67, 91] or by adding a resistance and using positive feedback [66]. Studies concentrated on reducing the effective loudspeaker resistance [65, 66, 67, 68, 69, 70] by direct positive current feedback or using combined sensor self-sensing schemes [71, 72]. When not also compensating for the coil inductance large vibration amplification at higher frequencies has been noticed by [73]. But as with 'the speaker performance rigidly controlled by the [negative impedance] amplifier, [...] enclosures have little effect on the cone motion and their own resonances may become considerably exaggerated' [73 p.243] further developments that aimed to compensate for the acoustical surroundings have rather compensated only for the coil resistance than also for the coil inductance [74, 75, 76]. However, for instance in order to compensate for the reduction of the high-frequency response [77] or to minimize dissipation in the amplifier output stage [78], inductance compensators nowadays are integrated in the power amplifier leading to the necessity of a combined amplifier-loudspeaker design [79] or may be added at the amplifier / loudspeaker interface [80] using a Zobel compensation. Recently a rather complicated estimator based on positive current and negative voltage feedback compensating for the coil inductance has been presented [81] for active vibration control. It has been used at loudspeakers [82] and in contrast to [63] it uses operational amplifiers. But both studies do not comment on the amplification at higher frequencies when the inductance is not ideally compensated as has been mentioned by [73]. Velocity amplification at higher frequencies might be acceptable for a loudspeaker whose pressure response is dominated by the mechanoacoustic characteristics at these frequencies but for active vibration control the velocity response has to be as small as possible over a wide frequency range.

In this study a shaker, an electrodynamic system, that is frequently used for active vibration isolation is considered. Physical limitations to its possible use as a self-sensing actuator in a simple active vibration isolation system where the actuator reacts relative to a rigid ground are investigated experimentally and theoretically. For this moving coil type actuator the sensor function stems from the back-electromagnetic force (back-EMF) induced in the conductive coil that is moved in a magnetic field whereas the actuator function is based on Lorentz force generated by a current in the coil in a magnetic field. As the back-EMF is proportional to the velocity of the conductor it should give an easy means to measure the vibration velocity of the mechanical system, but already the theoretical model of the open loop gives hints about necessary conditions for self-sensing. In a first step the velocity measured with an accelerometer and conditioning electronics is fed back to the shaker input voltage. In a second step proportional, positive coil current feedback to the shaker input is investigated. Finally the back-EMF is estimated using a Wheatstone or Owens bridge and is also fed back to the shaker input voltage. In order to prevent high-frequency bandwidth limitations only analogue components are considered for the feedback circuitry.

The report is organised in five parts:

- In Section 2 a theoretical model is formulated which explains the coupled electrical and mechanical behaviour of the shaker. The mechanical part of the model consists of the mass of the actuator coil mounted on springs whose velocity is to be controlled and the accelerometer that is used to measure coil velocity in order to realize velocity feedback. The electrical part includes the coil as an electrical system and the electrical connections of the shaker. The mechanical and electrical parts are coupled by the magnetic field in the actuator yoke that result in an induced velocity of the coil mass per unit input voltage (actuation mechanism) and an induced current in the coil per unit velocity of the coil mass (sensing mechanism).
- Section 3 compares two measured and simulated frequency response functions (FRFs): first coil velocity per input voltage and second coil current per input voltage.
- In Section 4 the implementation of velocity feedback control for active vibration damping is analysed using the Nyquist stability criterion. Furthermore the root locus technique is considered to determine a theoretical maximum gain of the closed loop.
- In Section 5 proportional current feedback is studied using the same methods as for velocity feedback.
- Finally in Section 6 an induced voltage feedback circuit is investigated which uses either a Wheatstone bridge compensator for the coil resistance or an Owens bridge that compensates for the coil resistance and inductance.

Simulation predictions and experimental measurements at the said commercial shaker are contrasted in order to understand the physics of the two self-sensing methods.

2. FREQUENCY DOMAIN MODEL OF THE SELF –SENSING ACTUATOR

In this section the components of an electrodynamic, self-sensing actuator depicted in Figure 2.1a with an attached accelerometer are described and their dynamical behaviour is evaluated numerically.

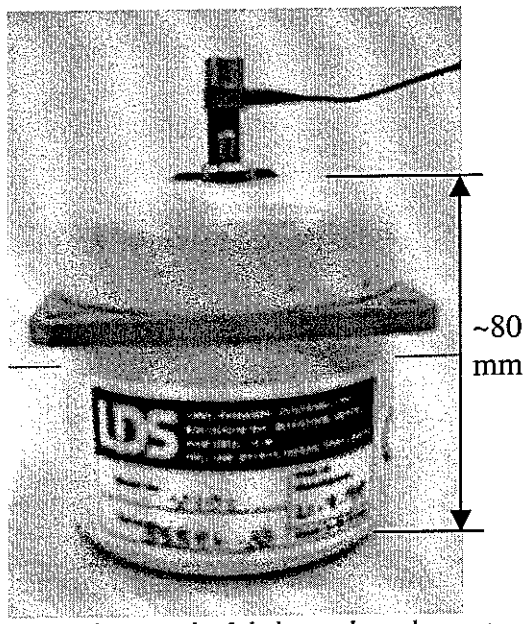

Figure 2.1a: *Photograph of shaker and accelerometer.*

As shown in Figure 2.1b the system studied consists of an electrodynamic shaker with an accelerometer mounted on its armature. The shaker is in its main parts composed of a permanent magnet (1) together with the ferromagnetic housing (2) serving as the stator or yoke and a linearly moving coil assembly (3) that is suspended (4) on the stator. These parts are protected by a rubber dust cover (5) that touches the moving coil assembly. The

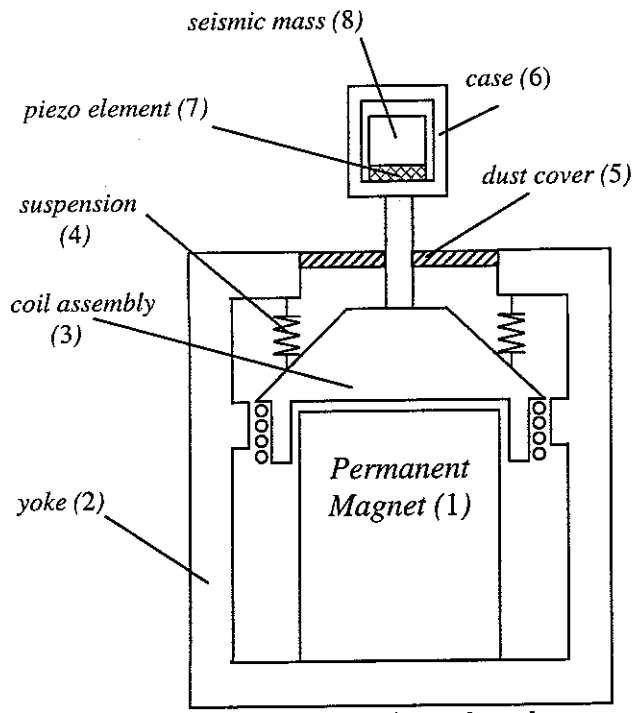

Figure 2.1b: *Schematic view of shaker and accelerometer.*

accelerometer consists of a case (6) and three piezoelectric elements (7) arranged in a triangular shape on which a seismic mass (8) is mounted. The accelerometer is fixed to the top of the coil assembly by a thin layer of wax. This type of device could be used for instance either in parallel with a passive mount isolating the source and receiver systems or as an inertial actuator attached to a flexible structure whose vibration is to be controlled. Due to its relative small force and static stiffness this type of actuator is not adequate to be used in series to a passive mount. When a voltage is applied to the coil the interaction between the coil current and a magnetic field in the air gap generates a Lorentz force in vertical direction between the coil assembly and the stator. The resulting coil displacement then depends on the inertial force of the coil mass and on the elastic forces applied on the coil assembly. Inversely when a force is input to the moving coil assembly it is forced to move at a certain velocity so that a voltage is induced in the coil itself. Following Lenz's law the sign of the induced voltage is opposite to the input voltage.

In order to model all these effects a fully coupled electromechanical system is considered in Section 2.1 assuming the behaviour of all electric, magnetic and mechanical parts to be time invariant and linear. Then in Section 2.2 for a better understanding of the dynamic response of the system the analysis is focused on two subsystems.

First the mechanical subsystem of the actuator is modelled by lumped elements so that the accelerometer case (6), the coil assembly (3), the suspension (4) and the dust cover (5) are considered as a mass supported by a spring and dashpot element in parallel. The actuation is represented by two opposite actuator forces acting on the ground and on the mass.

Second a lumped element model of the electrical circuit of the shaker that consists of a resistance and an inductance is analysed. The electrical and mechanical parts are coupled via the magnetic interaction of the coil assembly (3), the permanent magnet (1) and the yoke (2). The interaction is symbolized by a coupling element that relates the current/voltage parameters of the electrical circuit to the velocity/force parameters of the mechanical part. The fully coupled electromechanical dynamics are analysed by joining the mechanical and electrical models with the electromechanical coupling element.

The splitting up in subsystems enables a better understanding of the self-sensing actuator dynamics which is crucial for the design of a self-sensing actuator that is used to implement velocity, current and induced voltage feedback control as discussed in Sections 4, 5 and 6. The results obtained with the finally coupled model are validated with experimental measurements as presented in Section 3.

Tables 2.1 and 2.2 summarize the geometrical and physical properties of the device studied in this report and shown in Figure 2.1a.

Table 2.1: *Geometry and physical constants for the accelerometer type 4375 [83].*

Parameter	Value, Material, Type
Frequency range 5% tolerance	0.2 – 12000 Hz
Frequency range 10% tolerance	0.1 - 16500 Hz
Capacitance	650 pF
Transverse resonance kHz	18
Piezoelectric material	PZ 23
Magnetic sensitivity (5 Hz – 0.03T)	$30ms^{-2}/T$
Ambient temperature range	-74 to 250°C
Sensitivity	$0.458\ mV/m/s^2$
Weight	2.4 grams
Mounting technique	thin layer of wax
Power amplifier type	B&K 2635
Output impedance	$< 1\ \Omega$
Frequency range	1 Hz – 10kHz

Table 2.2: *Geometry and physical constants for the shaker V101/2 [84].*

Parameter	Value, Material, Type
Sine force, peak	8.9N
Armature resonance frequency	12000Hz
Effective mass of moving element	0.0065 kg
Suspension axial stiffness	3.15 N/mm
Impedance at 500 Hz	3 Ohm
Vibrator mass, base mounted	0.91 kg
Height	89mm
Width	65mm
Length	65mm

2.1 Actuator model

When using the equilibrium of forces for the mechanical part, Kirchhoff's laws for the electrical part and considering coupling between both parts the fully coupled equations of the actuator model in Figure 2.2 are

$$\begin{bmatrix} M & 0 \\ 0 & L \end{bmatrix} \begin{Bmatrix} \ddot{x} \\ \dot{i} \end{Bmatrix} + \begin{bmatrix} D & -\Psi \\ \Psi & R \end{bmatrix} \begin{Bmatrix} \dot{x} \\ i \end{Bmatrix} + \begin{bmatrix} K & 0 \\ 0 & 0 \end{bmatrix} \begin{Bmatrix} x \\ q \end{Bmatrix} = \begin{Bmatrix} f_p \\ u \end{Bmatrix} \tag{2.1}$$

where M, D and K are the mass, damping ratio and the stiffness of the mechanical part, L and R are the inductance and the resistance of the electrical part and Ψ is the electromagnetic transducer coefficient linking the two parts.

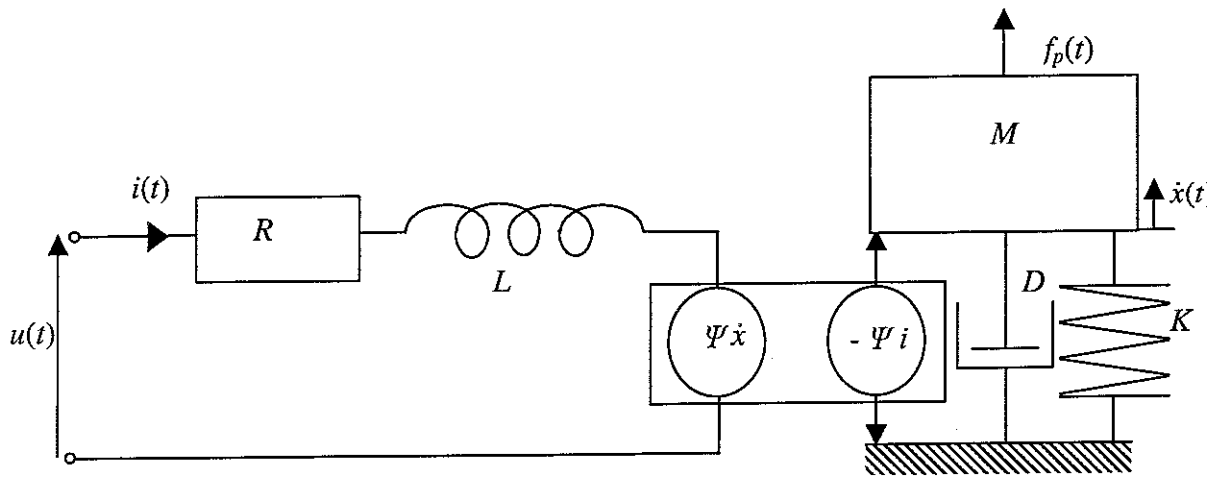

Figure 2.2: *Combined electrodynamic model in sensor and actuator direction*

Both the theoretical and experimental analysis are carried out in the frequency domain in the range between 1 Hz and 50kHz. Therefore, assuming a lightly damped system i.e. $D < 2\sqrt{KM}$ [13], the external force $f_p(t)$, the driving voltage $u(t)$, the coil current $i(t)$ and thus the electrical charges $q(t)$ and the coil velocity $\dot{x}(t)$ are considered to be sinusoidal at frequency ω with time dependence of the form $\exp(j\omega t)$ such that $x(t)=\mathrm{Re}(X(\omega)\exp(j\omega t))$, $i(t)=\mathrm{Re}(I(\omega)\exp(j\omega t))$, $u(t)=\mathrm{Re}(U(\omega)\exp(j\omega t))$ and $f_p(t)=\mathrm{Re}(F_p(\omega)\exp(j\omega t))$. Re(~) denotes real part of ~, $X(\omega)$, $I(\omega)$, $U(\omega)$ and $F_p(\omega)$ are the phasors of the variables and $j=\sqrt{-1}$ is the imaginary number. For simplicity $\exp(j\omega t)$ will be omitted in the mathematical formulation that is derived in terms of the phasors of the variables. Equation (2.1) is therefore rearranged in the frequency domain as follows

$$\begin{Bmatrix} F_p \\ U \end{Bmatrix} = \begin{bmatrix} Z_m & -\Psi \\ \Psi & Z_e \end{bmatrix} \begin{Bmatrix} \dot{X} \\ I \end{Bmatrix} \tag{2.2}$$

where

$$Z_m(\omega) = Mj\omega + D + K/(j\omega) \tag{2.3}$$

is the open circuit mechanical impedance defined as $Z_m = F_p/\dot{X}\big|_{i=0}$ and

$$Z_e(\omega) = R + Lj\omega \tag{2.4}$$

is the blocked electrical impedance defined as $Z_e = U/I\big|_{\dot{x}=0}$.

2.2 FRFs of the mechanical, electrical parts and the electromechanical coupling

Preliminary simulations have been carried out for the electrical and mechanical responses without coupling using plausible parameter values i.e. the two responses have been evaluated from equation (2.2) assuming Ψ=0. Figure 2.3 shows the amplitude and phase plot of the FRF $\dot{X}/F_p|_{i=0}=1/Z_m$ that is characterized by the typical response of a second order SDOF system governed by the parameters that are compiled in Table 2.3. At the resonance frequency the response is controlled by the damping term $1/D$ and the phase plot shows the typical 180 degree phase shift [13].

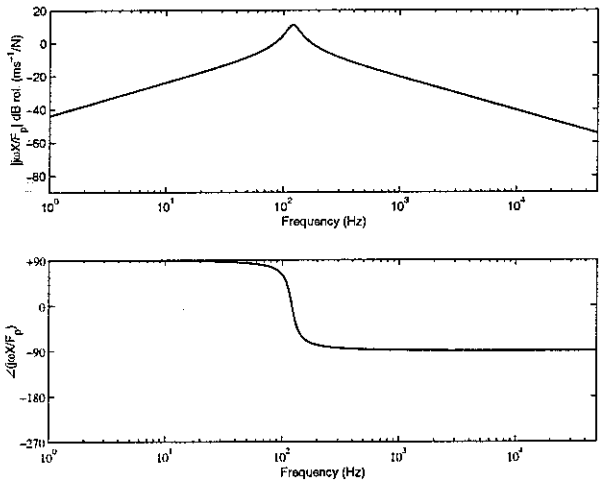

Figure 2.3: *Bode plot of the FRF velocity-force of the mechanical part of figure 2.2*

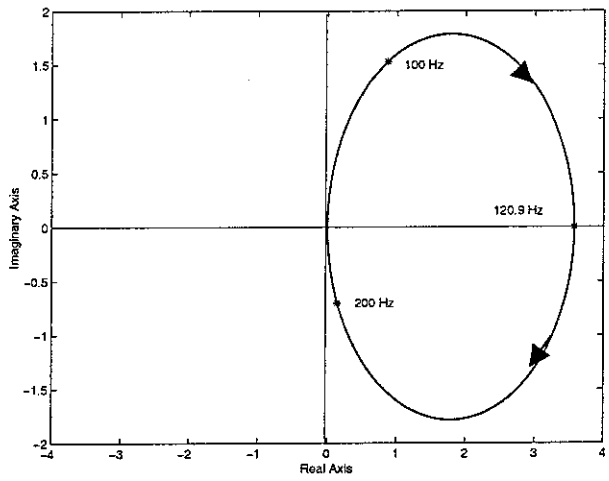

Figure 2.4: *Nyquist Plot of the velocity-force FRF of the mechanical part of figure 2.2 with a resonance frequency at 120.9 Hz*

The Nyquist plot in Figure 2.4 depicts the imaginary part of the FRF Im$(\dot{X}(\omega)/F_p(\omega))$ over the real part of the FRF Re$(\dot{X}(\omega)/F_p(\omega))$ with increasing excitation frequency $f = \omega/2\pi$. The curve starts at the origin for ω=0 at 90 degrees to the real axis and moves into the first quadrant to the intersection point with the real axis in order to come back to the origin at $\omega \rightarrow \infty$ via the fourth quadrant at –90 degrees to the real axis. The Nyquist plot magnifies the area around the natural frequency where the FRF is real and thus damping controlled. The locus intersects the real axis at ω = 0 and at the natural frequency ω_n where Re$(\dot{X}(\omega_n)/F_p(\omega_n))$=1/$D$.

Table 2.3: *Parameters for simulations of the mechanical system*

Parameter		Value
Coil assembly and case mass	M	0.0017 kg
Dust cover stiffness	K	981 N/m
Damping coefficient	D	0.28 Ns/m
Undamped natural frequency	ω_n	120.90 Hz
Damped natural frequency	ω_d	120.19 Hz

The result of the simulation of the blocked electrical FRF $I/U|_{\dot{x}=0}=1/Z_e$ using the parameters that are summarized in Table 2.4 is plotted in Figure 2.5 and shows a first order low-pass filter behaviour with an electrical, characteristic frequency $\omega_e=R/L$ and a maximum phase shift of -90 degrees.

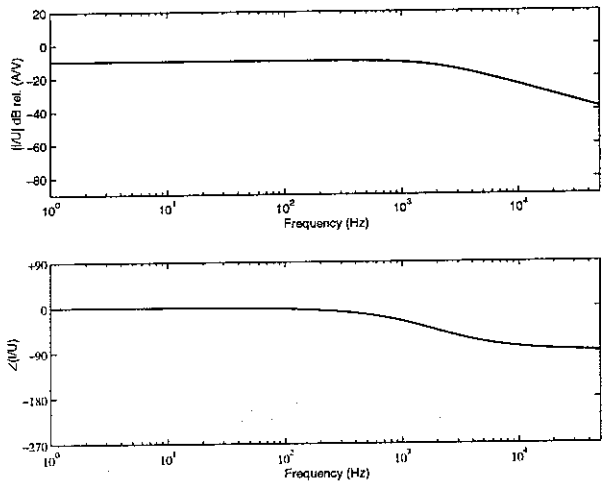

Figure 2.5: *Bode plot of the FRF current-voltage of the electrical part in figure 2.2*

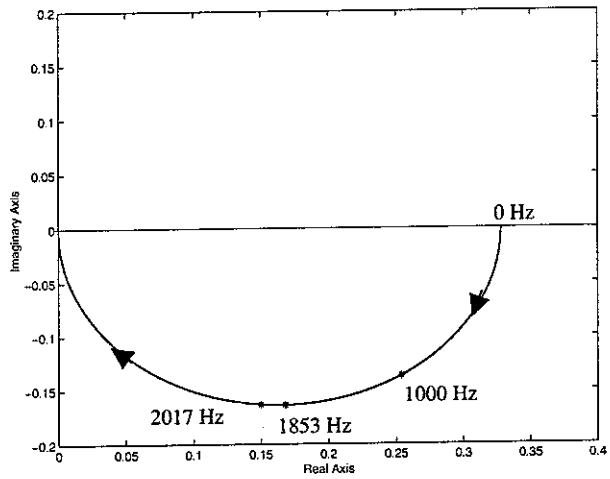

Figure 2.6: *Nyquist plot of the FRF current-voltage of the electrical part in figure 2.2*

The characteristic frequency can also be found in the Nyquist diagram depicted in Figure 2.6 by determining the frequency at which the imaginary part is identical to the real part i.e. the frequency at which the curve intersects with a straight line from the origin of an angle of -45 degrees with the real axis. In addition the crossing with the real axis gives the inverse of the static gain that is the resistance of the electrical circuit. Note that the curve starts on the real axis with $\omega=0$ and goes to the origin for $\omega\rightarrow\infty$ with an angle of -90 degrees to the real axis.

Table 2.4: *Parameters for simulations of the electrical system*

Parameter		Value
Inductance	L	0.262 mH
Resistance	R	3.05 Ohms
Characteristic frequency	ω_e	1852.76 Hz

The coupled response of the electro-mechanical system has been derived from equation (2.2). A motional impedance term as influence of the mechanical part appears in the FRF I/U. It can be used for sensing the mechanical velocity by an electrical circuit. Inversely an electrical impedance term as influence of the electrical part appears in the FRF $\dot{X}/F_p$. Further analysis will show that this term adds damping to the mechanical FRF and may be used for vibration control.

The FRF of the mechanical system when the electrical connections are short-circuited

$$\left.\frac{\dot{X}(\omega)}{F_p(\omega)}\right|_{u=0} = \frac{1/Z_m}{1+\Psi^2/(Z_e Z_m)} = \frac{1}{Z_m + \Psi^2/Z_e} \tag{2.5}$$

can be considered as being the open circuit mechanical FRF $\dot{X}/F_p|_{i=0}=1/Z_m$ (see Figure 2.3) where the output $\dot{X}$ is fed back with a feedback FRF Ψ^2/Z_e. In order to realize unconditionally stable velocity feedback [18], Ψ^2/Z_e should be positive real where the inverse of the resistance determines the feedback gain. However, in a real system in analogy to the motional impedance in an electrical circuit a term related to the electrical system $\Psi^2/Z_e = \Psi^2/(R+Lj\omega)$ is added in the numerator of equation (2.5). As a result the mechanical impedance of the short-circuited actuator has an additional term $\Delta D = \Psi^2/R$ if the inductance L is negligible. Since this term is proportional to the velocity $\dot{x}$ damping is added to the mechanical impedance. However, if the coil resistance R is negligible the mechanical impedance is increased by a term $\Delta K/(j\omega) = \Psi^2/(Lj\omega)$. Hence, additional stiffness results as this term is proportional to the coil displacement $x=\dot{x}/j\omega$. As in general both electrical parameters are not negligible stiffness and damping are added. Nevertheless the damping effect is particularly effective at frequencies lower than the characteristic electrical frequency while the stiffness effect tends to be particularly effective at higher frequencies greater than the characteristic electrical frequency. From this simple analysis it is easy to see that for active vibration damping it is not necessary to feed back the coil velocity using an external sensor since it is possible to add damping to the actuator by enhancing the term Ψ^2/R. This can be achieved either by increasing the coupling coefficient Ψ or by reducing the electrical resistance R and compensating for the inductance L. As Ψ is given by the shaker design Sections 5 and 6 deal with implementing a negative impedance amplifier in order to reduce R. For instance the amplitude of the FRF $\dot{X}/F_p$ is reduced by more than 6 dB relative to the open circuit mechanical FRF $\dot{X}/F_p|_{u=0}$ if the open loop FRF

$$\left|\Psi^2/(Z_e Z_m)\right| >> 1 \Leftrightarrow \Psi^2 >> |Z_e Z_m| \tag{2.6}$$

indicating that the coupling effect is large at the mechanical resonance frequency where $|Z_m|$ is small and for frequencies smaller than the electrical frequency $\omega_e=R/L$ where $|Z_e|<<1$.

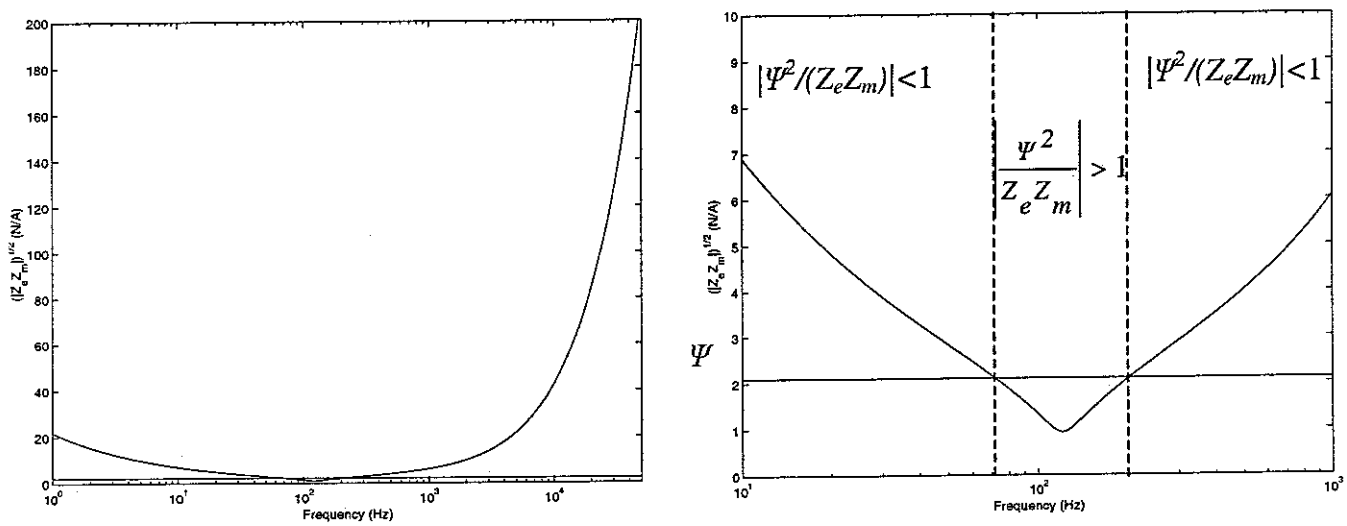

Figure 2.7: *Uncoupled FRFs Z_mZ_e compared to the transducer coefficient $\Psi=2.1$ and zoom at the mechanical resonance*

Equation (2.6) implies that the value of the transducer coefficient is essential for sufficient coupling. For the chosen shaker parameters Figure 2.7 shows the curve of the square root of the modulus of the two terms Ψ^2 and $Z_m Z_e$ as a function of frequency. The left plot indicates that the coupling effect is important close to the mechanical frequency between about 70Hz and 200Hz. Also, the shape of the FRF $Z_m Z_e$ suggests that by increasing the transducer gain the coupling at lower frequencies is increased more than at frequencies greater than the mechanical resonance frequency.

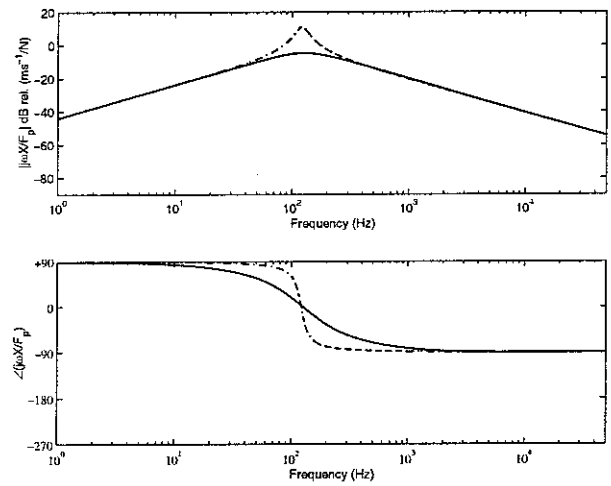

Figure 2.8: *Simulated Bode plot of the FRF between the primary force and the velocity $\dot{X}$ of the complete coupled electromechanical model in figure 2.2 compared with the FRF of the mechanical part (dash dotted line)*

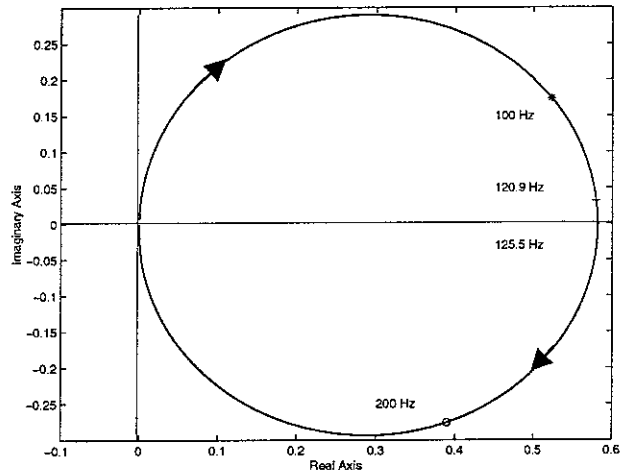

Figure 2.9: *Simulated Nyquist plot of the FRF from the primary force input to the velocity for the coupled electromechanical model in figure 2.2, zoom at the origin*

In the same way the bode plots of the closed ($\dot{X}/F_p|_{u=0}$, solid line) and open circuit mechanical FRF ($\dot{X}/F_p|_{i=0}$, dashed dotted line) depicted in Figure 2.8 show noticeable differences only at the mechanical resonance frequency. The damping effect due to adding an electrodynamic device with a resistor is visible around the resonance frequency where the amplitude is reduced and the phase transition is flattened. In general significant damping is only added to natural frequencies that lie below the characteristic electrical frequency and thus below the roll-off depicted in Figure 2.5.

The Nyquist plot of the closed circuit mechanical FRF ($\dot{X}/F_p|_{u=0}$) depicted in Figure 2.9 indicates that the resonance frequency of the mechanical system has shifted upwards to about 125.5 Hz relative to the case depicted in Figure 2.4. This is due to the increase of the dynamic stiffness by the additional self-inductance L. Adding an additional capacitance that would introduce an additional inertia effect could compensate for this phenomenon. The increase of damping is highlighted by the reduction of the real part at the intersection point of the locus with the real axis. Moreover as the superposition of the electrical FRF and the mechanical FRF is greatest at the mechanical resonance frequency where the electrical FRF does not have a phase shift the phase of the mechanical FRF is deformed towards a zero phase shift. Hence the locus in the Nyquist plot in Figure 2.9 stays in the positive real plane even by adding the self-sensing actuator. But following Equation (2.5) there would be an additional phase shift at higher frequencies due to the electrical FRF if the transducer coefficient was great enough.

The FRF between the input voltage and the coil current when there is no primary force

$$\left.\frac{I(\omega)}{U(\omega)}\right|_{F_p=0} = \frac{1/Z_e}{1+\Psi^2/(Z_e Z_m)} \tag{2.7}$$

consists of the blocked electrical FRF $I/U|_{\dot{x}=0} = 1/Z_e$ (see Figure 2.5) whose output I is fed back with a feedback FRF Ψ^2/Z_m. By inverting equation (2.7) $U = \left(Z_e + \Psi^2/Z_m\right)I$ the impedance between the voltage and the current in the electric circuit consists of the electrical impedance Z_e and a term containing the coupling coefficient and the mechanical impedance Ψ^2/Z_m. The latter one is the motional impedance as explained in more detail for instance by [25]. It indicates the influence of the mechanical system on the electrical one due to the electrodynamic coupling with the motion of a mechanical system.

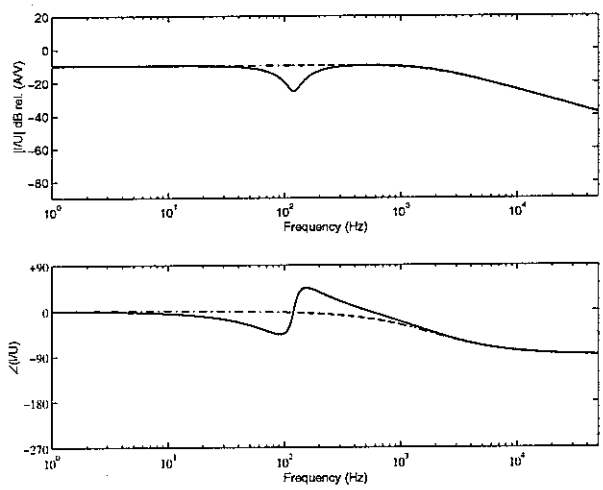

Figure 2.10 : *Simulated Bode plot of the FRF from the source voltage to the current for the coupled electro-dynamic model in figure 2.2 (solid line) compared to the FRF of the electrical model(dash dotted line)*

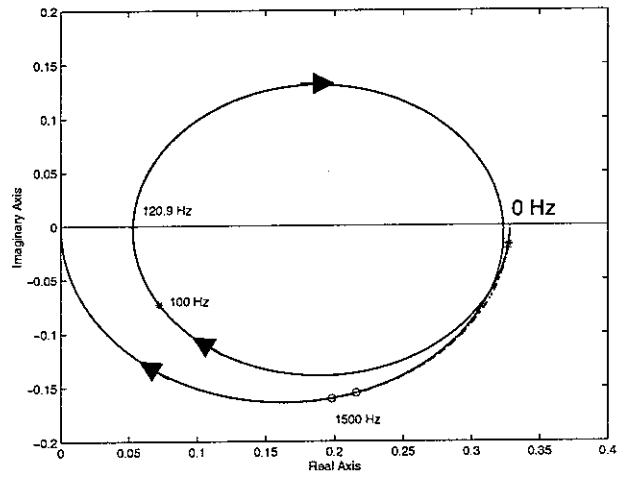

Figure 2.11: *Simulated Nyquist plot of the FRF from the source voltage to the current for the coupled electro-dynamic model in figure 2.2 compared with the FRF of the electrical model(dash dotted line)*

Figure 2.10 shows the Bode plot of the coupled ($I/U|_{F_p=0}$) and blocked ($I/U|_{\dot{x}=0} = 1/Z_e$) FRF between the source voltage and the current. Similarly to the analysis presented above the influence of the mechanical part on the electrical part is found to be greatest at the mechanical resonance frequency. As indicated by equation (2.7) the amplitude of the coupled FRF is reduced in the top plot of Figure 2.10. The phase tends to be deformed in direction of the mechanical phase i.e. towards a minus 90 degrees phase shift for frequencies smaller than the mechanical resonance frequency and towards a plus 90 degrees phase shift for frequencies greater than the mechanical resonance frequency. The coupling can be neglected for frequencies far away from the mechanical resonance frequency as the curve of the coupled FRF then tends towards the curve of the uncoupled FRF in Figure 2.10.

The Nyquist plot of the coupled (solid line) and blocked FRF depicted in Figure 2.11 also shows the effect of the motional impedance effect. Similarly to the case of the coupled

mechanical FRF in equation (2.5) the coupled electrical FRF results from the combination of the uncoupled electrical and the uncoupled mechanical FRF in the frequency range where coupling is important. Here the locus of the uncoupled mechanical FRF depicted in Figure 2.4 is both rotated around the origin by 180° and scaled in such a way as to fit into the locus of the uncoupled electrical FRF (dash dotted line) at frequencies close to the mechanical resonance frequency. When the natural frequency is increased by adding stiffness to the mechanical system the resulting motional impedance loop is shifted in direction of the imaginary axis and its area decreases. Thus when the movement of the mechanical system is restricted by a stiffness tending to infinity no motional impedance loop is observable as it is close to the origin while its size tends to zero. The impedance curve then only shows the characteristics of the electrical system whose locus is depicted in Figure 2.6. A similar effect is found by increasing the damping factor of the mechanical system when the motional impedance circle also becomes very small relative to the electrical impedance. Increasing the mass moves the motional impedance circle to lower frequencies and also reduces its surface.

3. COMPARISON OF MEASURED AND SIMULATED OPEN LOOP ELECTRICAL AND MECHANICAL FREQUENCY RESPONSE FUNCTIONS

Figure 3.1 shows the circuit and the equipment used for identification measurements. Its characteristic values are compiled in Tables 3.1 and 3.2.

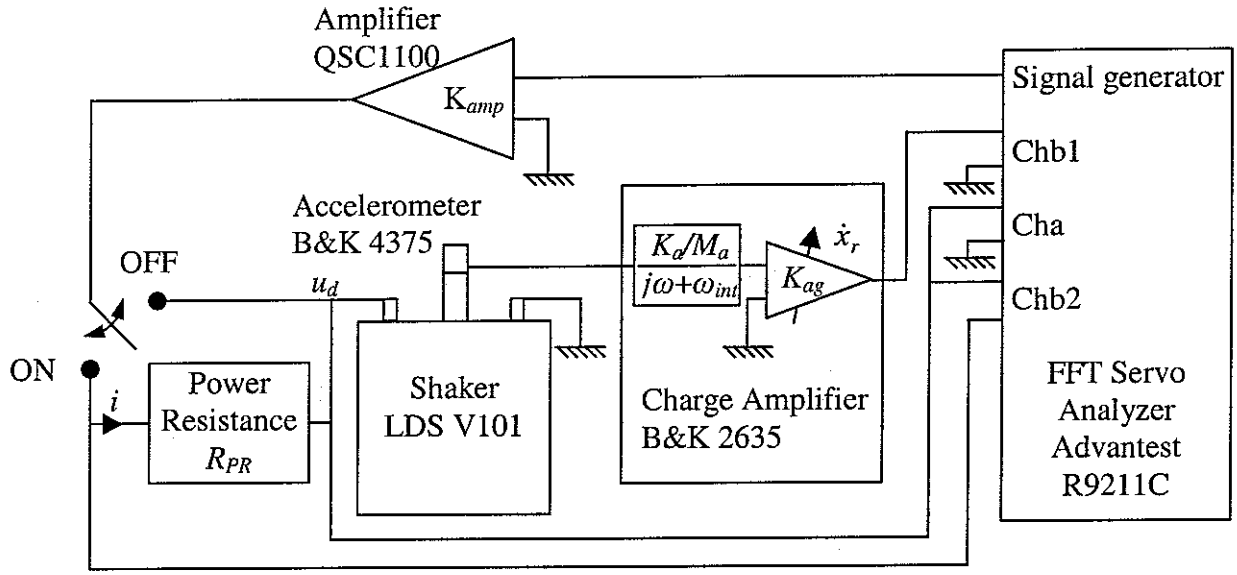

Figure 3.1: *Measurement circuit for identification of shaker parameters*

The accelerometer outputs a signal proportional to the relative displacement x_{rel}=Re($X_{rel}(\omega)$exp($j\omega t$)) between its seismic mass M_a and the moving coil and the charge amplifier integrates the accelerometer output signal. The resulting integrated relative displacement $\dot{x}_r(t) = \mathrm{Re}\left(\dot{X}_r(\omega)\exp(j\omega t)\right)$ measured on channel Chb1 (switch OFF) is a good estimation of the coil velocity $\dot{x}$ for frequencies much smaller than the accelerometer resonance frequency as is explained in Appendix A. For convenience the mechanical FRF is taken with reference to the voltage input of the shaker u_d(t)=Re($U_d(\omega)$exp($j\omega t$)) measured on channel Cha. This disturbance voltage then generates a disturbance force f_p on the shaker as illustrated in the schematic overview in Figure 3.2.

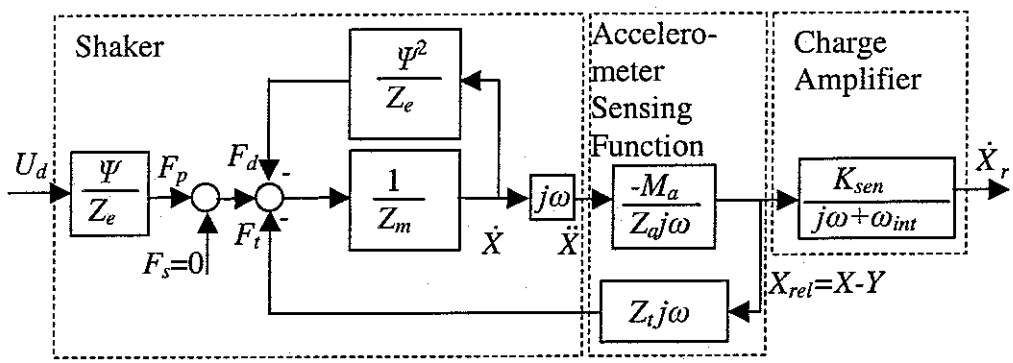

Figure 3.2: *Open loop FRFs*

For identification measurements there is no secondary, feedback force $f_s(t)$=Re($F_s(\omega)$exp($j\omega t$)) applied to the shaker mass but there are an internal electrical damping force $f_d(t)$=Re($F_d(\omega)$exp($j\omega t$)) due to the electrodynamic coupling and an internal transmission force

$f_t(t)=\mathrm{Re}(F_t(\omega)\exp(j\omega t))$ between the accelerometer inertial mass and the shaker mass. Then instead of identifying parameters in the FRF $\dot{X}_r/F_p$, parameters in the FRF

$$\frac{\dot{X}_r}{U_d}=\frac{\Psi M_a K_{sen}}{\left(Z_t Z_e jM_a\omega+Z_e Z_m Z_a+\Psi^2 Z_a\right)\left(j\omega+\omega_{int}\right)} \tag{3.1}$$

are identified, where $Z_t=K_a/(j\omega)+D_a$ is an impedance defined by the relative velocity $\dot{x}_{rel}$ between the coil assembly and the seismic mass of the accelerometer and the force transferred from the coil assembly onto the seismic mass f_t. $Z_a=j\omega M_a + D_a + K_a/(j\omega)$ is the accelerometer mechanical impedance, K_a is the stiffness of the piezoelectric material and D_a its linearized damping coefficient, K_{sen} a measurement equipment constant and ω_{int} the non-ideal integrator cut-off frequency. Hence, the electrical frequency and the damped, mechanical natural frequency can be identified simultaneously in only one FRF, but parameters of the electrical FRF I/U_d are also identified in order to distinguish between mechanical and electric damping effects. For this purpose the shaker voltage u_d is again measured on channel Cha and the voltage drop is measured at an additional power resistance R_{PR}, proportional to the current i through it, on channel Chb2 (switch ON).

The measurement gain of the charge amplifier K_{ag} is adapted manually for both sets of measurements such as to observe a sufficient and linear signal output and the amplifier gain K_{amp} such as to limit the shaker current to 1A. Additionally the equipment introduces measurement gains compiled in Table 3.1 that are included in the model rather than used to modify measurement data so that all measured signals have unit Volts. They are fixed by the power resistance R_{PR} which converts the current through it to voltage with a gain $K_{PR} = R_{PR}$ and by the accelerometer and its internal circuit with the amplification K_{sen} that converts a charge proportional to the relative displacement to voltage. As the supplier makes the low frequency approximation described in Appendix A for the accelerometer the additional factor $\omega_{na}^2=K_a/M_a=10^{10}$ rad/s^2 is included into K_{sen} in order to convert the sensitivity given by the supplier in terms of voltage/acceleration K_s into voltage/displacement.

Table 3.1: *Chosen gains*

Gain type		Value
Amplifier gain	K_{amp}	16 dB
Measurement gain	K_{ag}	1 V/V, 10V/V, 100V/V
Fixed Accelerometer gain	$K_{sen}=K_{ag}K_a/M_aK_s$	458 10^7 V/m
Power resistance gain	K_{PR}	1, 2, 3 Ω

The internal signal generator of the frequency analyser is used to generate a white noise signal with a 1V amplitude successively in the range from 0-10Hz, 0-100Hz, 0-1kHz, 0-10kHz and 0-100kHz at linearly stepped frequencies, so that the 1-10Hz, 10-100Hz, 100-1kHz, 1k-10kHz and 10k to 100kHz frequency ranges respectively are well excited. 32 successive measurements are carried out in each range and the estimated FRF with a resolution of 800 lines in each frequency range, is automatically averaged by the servo analyser. For the

estimation the frequency analyser internally digitises the data, calculates the power spectral density of the input signal in channel Cha $S_{aa}(\omega)$ and the cross spectral density between channel Cha and channel Chb $S_{ab}(\omega)$ so that an estimate of the FRF between channel Cha and Chb is given by [85] as

$$H_{ab}(\omega) = \frac{S_{ab}(\omega)}{S_{aa}(\omega)}. \tag{3.2}$$

The calculated frequency data is visualized and compared to simulations I/U_d and $\dot{X}_r/U_d$. Parameters are adapted to give a good visual correspondence between simulations and measurements of both FRFs. Due to the coupling between the FRFs this process is iterative as having a good fit for one FRF does not necessarily also mean a good fit for the other one.

3.1 Measured and simulated mechanical frequency response function with short-circuited electrical part

Comparing the bode plots of the FRF $\dot{X}_r/U_d$ estimated from measurements (solid line) to the simulations with parameters in Table 3.2 (dashed line) in Figure 3.3 shows an excellent correspondence for frequencies between the low-pass filter approximation of the integrator in the charge amplifier and the natural frequency of the accelerometer. The damped resonance peak of the coil assembly can be found with the 180 degrees phase shift as well as the influence of the electrical system with another phase shift of 90 degrees. Although the same mechanical resonance frequency as implied by supplier's data has been identified mass and stiffness values are found to be different in order to adequately model the relative damping influence.

Table 3.2: *Identified parameters*

Parameter		Value
Coil assembly mass	M	0.0017 kg
Duct cover stiffness	K	989 N/m
Damping coefficient	D	0.28 Ns/m
Inductance	L	0.262 mH
Resistance	R	3.05 Ohms
Actuator constant	Ψ	2.1 N/A or V/m/s
Stiffness of inertial mass support	K_a	6.7×10^6 N/m
Accelerometer Damping	D_a	4 Ns/m
Inertial mass of accelerometer	M_a	0.00067 kg

Furthermore the assumption of a non-ideal integrator does not seem to hold at least not its modelling as a single low-pass filter. Characteristic curves given by the supplier also indicate that a higher order filter is implemented in the charge amplifier.

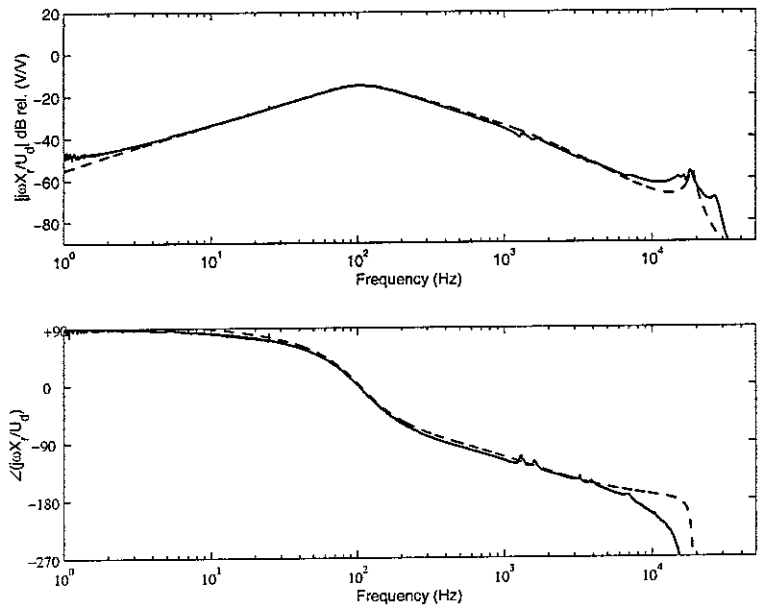

Figure 3.3: *Bode plot of the measured (solid line) and simulated (dotted line) FRF from the source voltage U_d to the integrated relative displacement $\dot{X}_r$*

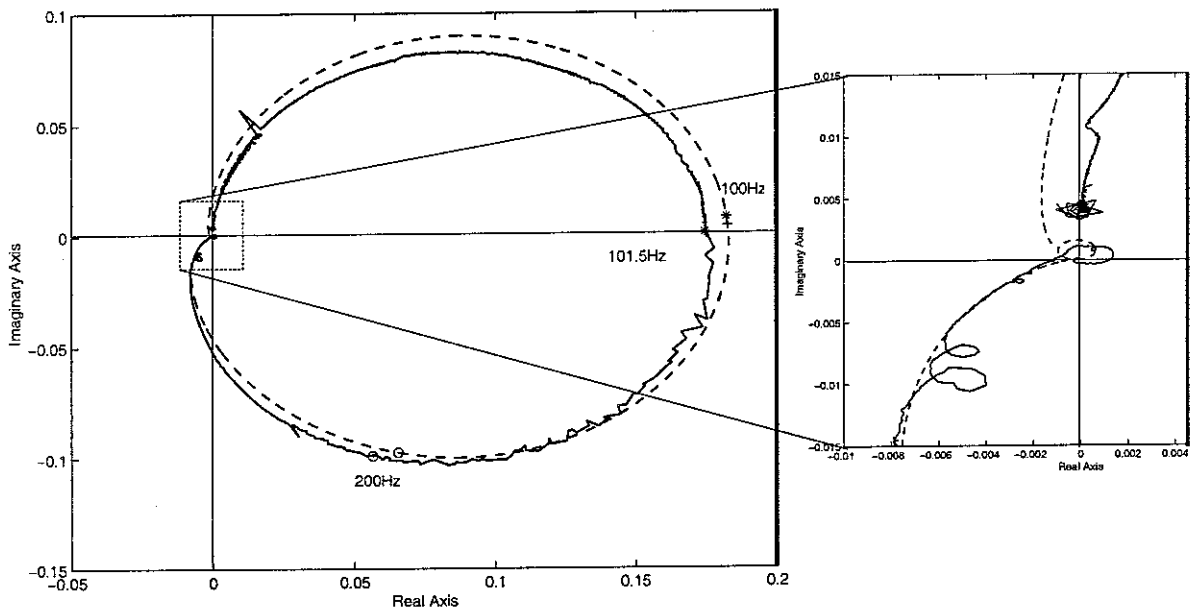

Figure 3.4: *Nyquist plot of the measured (solid line) and simulated (dotted line) FRF from the source voltage U_d to the integrated relative displacement $\dot{X}_r$ and zoom at the origin*

The Nyquist plot also exhibits reasonable correspondence between measurements and simulations around the natural frequency of the coil assembly. In particular the resonance frequency itself turns out to be about 101.5 Hz, which is close to the simulated 102.5 Hz. Additionally not modelled resonance loops appear at about 1500Hz. Moreover the additional loop due to the accelerometer dynamics is observable close to the origin though measurements show a different loop form that indicates that the model overestimates the

importance of the accelerometer. The plot also shows the spill-over due to the electrical system as the FRF from the disturbance voltage including the electrical model is considered.

3.2 Measured and simulated electrical frequency response function without primary force excitation

As is the case for the FRF from the source voltage U_d to the integrated relative displacement $\dot{X}_r$ the correspondence between measurements and simulations of the FRF from U_d to the coil current I is excellent for frequencies around the mechanical natural frequency as shown in Figure 3.5. The influence of the mechanical system on the electrical system is visible in the amplitude plot, where the back-EMF effect produces a trough at the mechanical resonance frequency, and in the phase plot, where a phase shift of 180 degrees seems to be forced by the mechanical system. But the coupling is not strong enough so that not a complete 180° phase shift is visible. Note that the additional measurement gain K_{PR} is included so that the steady static value does not give the exact inverse of the resistance R and the unit of the plot is Volts per Volts.

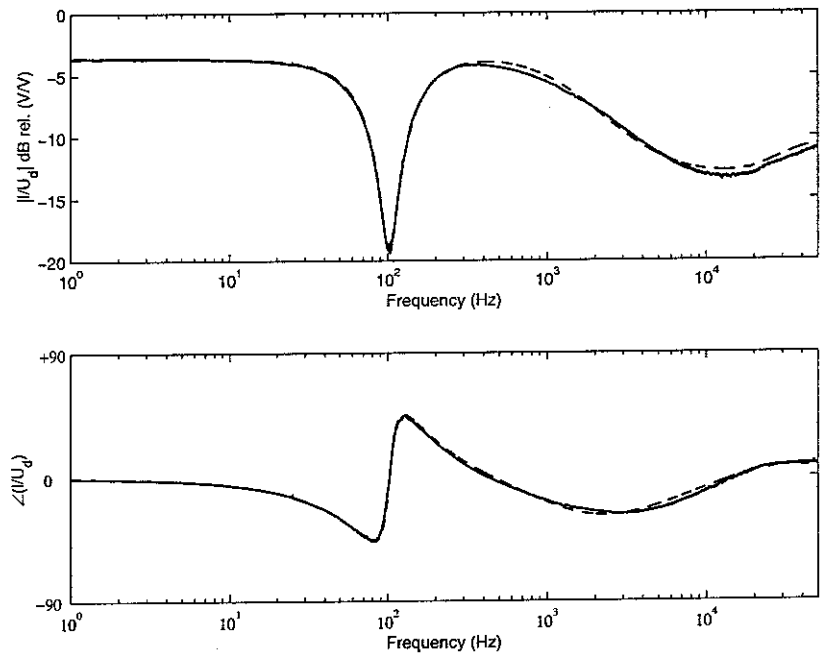

Figure 3.5: *Bode plot of the measured (solid line) and simulated (dashed line) FRF from the source voltage to the measured coil current when considering eddy current losses of the core and an additional capacitance as in figure B.1, zoom between 0 and -20 dB*

At frequencies greater than the electrical frequency the simulation shown in Figure 2.10 with the model in Figure 2.2 may not pick up important physical characteristics of the actuator. However, in Section 2 it has been noted that the natural frequencies of the mechanical system to be damped lies below the electrical, characteristic frequency. Therefore a detailed model as explained in Annex B is not necessary in order to evaluate damping, but still it is used for simulations in Figure 3.5 and Figure 3.6. This model describes an additional capacitance effect parallel to the shaker and eddy current effects modelled by a resistance R_e parallel to the shaker inductance as proposed for instance in reference [80].

Considering additional eddy currents and capacitance C as well as the accelerometer function the FRF I/U_d becomes

$$\frac{I(\omega)}{U_d(\omega)} = \frac{(Cj\omega)^2\left[\tilde{Z}_m\left(\tilde{Z}_e Z_{e2} - (Lj\omega)^2\right) + \Psi^2 jZ_{e2}\omega\right] K_{PR}}{Z_{e1}(Cj\omega)^2\left[\tilde{Z}_m\left(\tilde{Z}_e Z_{e2} - (Lj\omega)^2\right) + \Psi^2 jZ_{e2}\omega\right] - Z_{e2}\tilde{Z}_m} \tag{3.3}$$

where $\tilde{Z}_e = Lj\omega + 1/(Cj\omega)$, $Z_{e1} = j\omega L_1 + R + 1/(Cj\omega)$ and $Z_{e2} = (L_2 + L)\, j\omega + R_e$ are additional electrical impedances with line inductances L_2 and L_1 and $\tilde{Z}_m = -Z_m Z_a \omega^2 - Z_t M_a^2 j\omega$ is an enlarged motional impedance.

The Nyquist plot of this FRF depicted in Figure 3.6 shows a good fit between simulations with additional parameters in Tables B.1 and B.2 and measurements. The mechanical resonance frequency can also be very well found to lie at about 101.5 Hz. Also in Figure 3.6 it is noted that the locus starts at a real value of twice the inverse shaker resistance R due to the measurement gain K_{PR}=2. Furthermore the typical characteristic of a lead part is added to the plot at higher frequencies well above 1500 Hz. The fact that this loop is smaller than the loop for lower frequencies indicates that additional damping is introduced so that the assumption of an additional resistance due to for instance eddy currents is reasonable. Changing parameters indicates that correspondence between measurements and simulations is either satisfactory in the range from about 300 Hz to about 2000 Hz or in the range from 10 kHz to 40 kHz. Hence, there seems to be a trade-off between getting a good correspondence in either of those frequency bands. Moreover the Nyquist plot shows that at the simulated mechanical natural frequency the FRF does not change significantly in comparison to Figure 2.11 when changing the electrical higher frequency characteristics due to the capacitance and also the damping of the mechanical system due to Eddy currents modelled by the resistance R_e can be neglected.

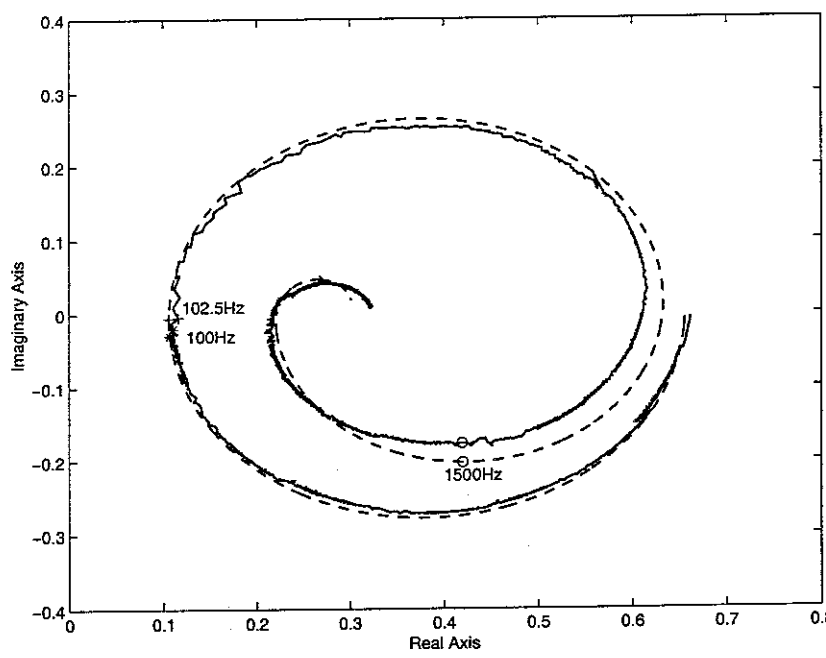

Figure 3.6: *Nyquist plot of the measured (solid line) and simulated (dotted line) FRF from the source voltage to the coil current when considering eddy current losses of the ferromagnetic core and an additional capacitance*

4. MEASURED VELOCITY FEEDBACK CONTROL

After theoretical analysis and experimental identification of the open loop frequency responses of the shaker in the previous two sections in this section an adequate control algorithm is investigated for the implementation of measured velocity feedback. As shown by [23] direct velocity feedback with collocated actuators and sensors is unconditionally stable. Additionally direct feedback of the absolute velocity leads to active damping at resonance frequencies as shown by [3]. Therefore fixed gain feedback of the shaker coil absolute velocity also called rate or direct feedback is investigated. Practical stability limits due to non-ideal actuator and sensor behaviour are found using the Nyquist criterion and the root locus plot. First simulations show the closed loop behaviour and second results of implementing gain feedback at a real shaker are presented.

4.1 Stability and simulation of the feedback control system

Considering the system depicted in Figure 3.2 when the feedback loop is closed by a fixed gain $-G$ as shown in Figure 4.1 a secondary force f_s is generated by the shaker that cancels the disturbance by the primary force f_p. In this system the primary force f_p is generated by a disturbance voltage u_d and the secondary force f_s results from a feedback voltage u_{fb}.

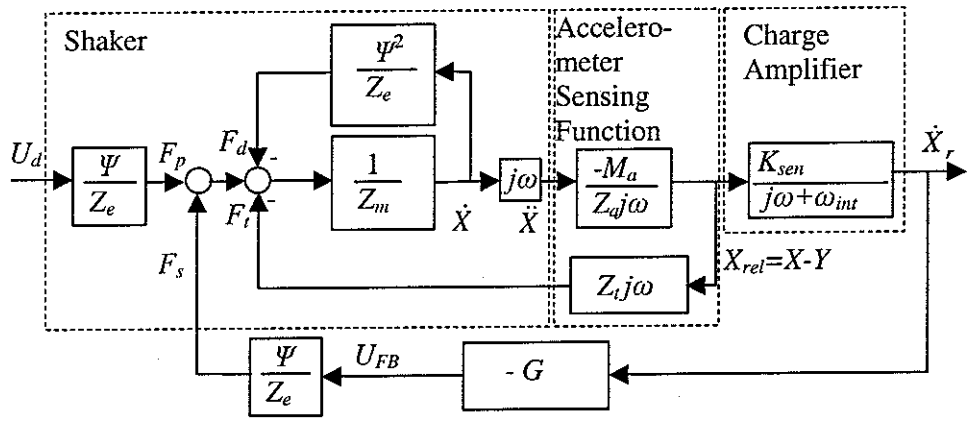

Figure 4.1: *Closed loop FRFs*

Moreover, the open loop FRF from U_d to F_p and from U_{FB} to F_s is identical. Therefore instead of considering FRFs from F_p or F_s to $\dot{X}_r$, FRFs from U_d and U_{FB} to $\dot{X}_r$ are investigated. Closing the loop thus means modifying the disturbance voltage u_d by an additional feedback voltage u_{fb} so that the resulting voltage input to the shaker is $u = u_d + u_{fb}$. Then the closed loop FRF from U_d to $\dot{X}_r$ becomes

$$\left.\frac{\dot{X}_r}{U_d}\right|_{cl} = \frac{\dot{X}_r/U_d}{1+G\frac{\dot{X}_r}{U_d}} = \frac{\Psi M_a K_{sen}}{\left[j\omega M_a Z_t Z_e + \left(Z_e Z_m + \Psi^2\right)Z_a\right]\left(j\omega+\omega_{int}\right)+M_a G\Psi K_{sen}} \tag{4.1}$$

By comparing the open loop equation (3.1) to the closed loop equation (4.1) the additional $M_a K_{sen} G\Psi$ term of zero order in $j\omega$ proportional to velocity indicates that damping is added to the open loop FRF by negative feedback. Inversely positive feedback leads to negative

damping. If the sensor and actuator transducers are not collocated velocity feedback may destabilize the FRF for a certain gain determined for instance by the Nyquist criterion. Considering a stable continuous open loop FRF $G\dot{X}_r/U_d$ the closed loop is conditionally stable if the locus of the open loop in the Nyquist diagram does neither encircle nor pass through the critical point (-1,0) as stated e.g. in [86]. If instead the sensor and actuator transducers are collocated so that the real part of the open loop FRF is constrained to be positive definite the closed loop is even unconditionally stable.

Applying this Nyquist criterion to the locus of the open loop FRF $\dot{X}_r/U_d$ in Figure 3.4 shows that the closed loop is conditionally stable. Multiplying with a feedback gain G might lead to instability of the closed loop as the small loop at the accelerometer natural frequency or at the non-modelled loop at about 1500Hz might increase and finally encircle the critical point. This is illustrated in Figure 4.2 with a set of simulations using the identified model equation (3.1) by varying the negative feedback gain G. Figure 4.2 illustrates the open loop FRF $G\ \dot{X}_r/U_d$ for different values of the gain G where for G>2220 the locus encircles the critical point and instability for the closed loop FRF is predicted.

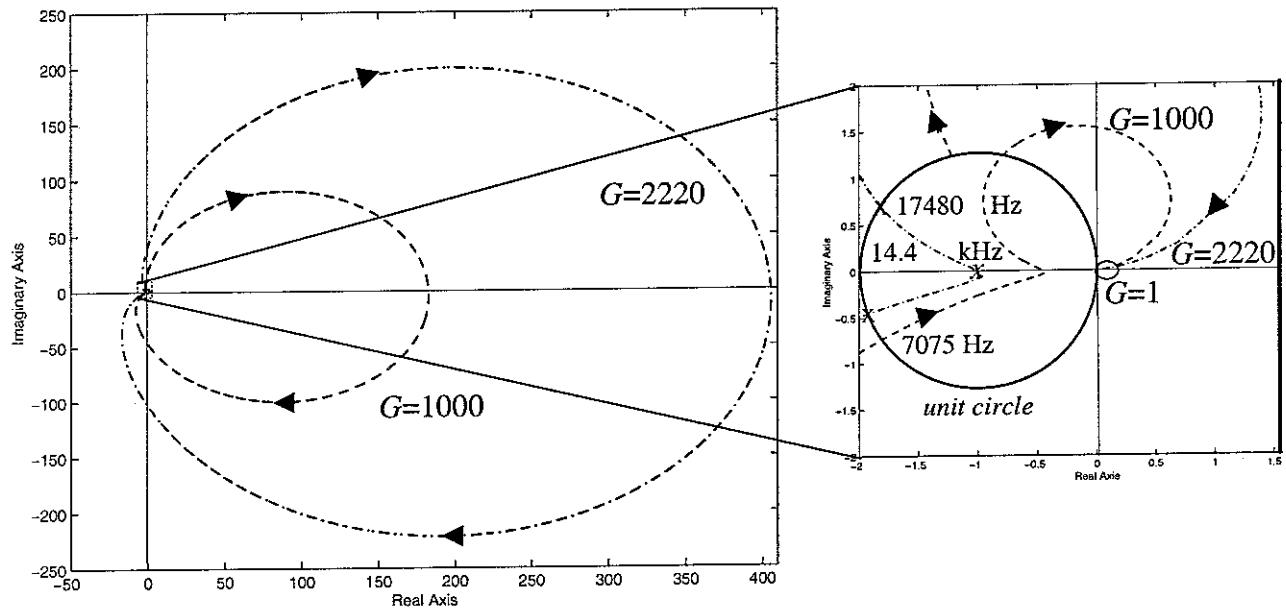

Figure 4.2: *Open loop Nyquist plot of the FRF $G\ \dot{X}_r/U_d$ of the model in Figure 2.2 for different values of the feedback gain G and zoom at the origin*

Additionally the closed loop amplitude is predicted to decrease only at frequencies where the open loop locus lays outside a unit circle around the critical point. For instance, when G=2220 for frequencies inside the unit circle from about 7075 Hz to ca. 17480 Hz the closed loop amplitude is increased by $1/|1+G\dot{X}_r/U_d|$. The oscillation frequency of the unstable closed loop is found at the critical point to be 14400 Hz. Hence spillover in the negative real half plane is critical for vibration reduction as the disturbance might increase.

In contrast to the ideal open loop locus in Figure 2.9 that does not show spillover into the negative real plane the open loop locus with non-ideal accelerometer, actuator and measurement equipment in Figure 4.2 has spillover. Adding only the actuator leads to spill-

over into the third quadrant that itself does not lead to instability, but as the locus crosses into the unit circle around the critical point vibrations are amplified in this frequency range. Additionally small random changes in the locus together with a sufficient feedback gain may destabilize the closed loop as the locus is close to the critical point. Adding an accelerometer adds an additional resonance loop and a phase shift of 180 degrees to the open loop. For higher feedback gains the accelerometer thus destabilizes the closed loop. Although measurements in Figure 3.4 do not show non-ideal behaviour of the integrator implemented in the charge amplifier in the considered frequency range, non-ideal integration is a potential source of instability as the locus might move into the second quadrant close to the critical point at a sufficient gain. Then, when entering the unit circle around the critical point, vibrations are amplified and small random changes in the locus may lead to instability of the closed loop. Note that this would only be a risk at extremely high gains, G=2220 in Figure 4.2, so that for most practical applications stability is predicted.

Some of the effects discussed above are also found by closed loop simulations. Figure 4.3 shows the Bode plot of the closed loop FRF $\dot{X}_r/U_d$ in equation (4.1) for different negative values of the feedback gain G. At the first mechanical natural frequency at 101.5 Hz damping is introduced that is visible in the amplitude plot by decreasing amplitude and in the phase plot by a flattening phase transition when comparing for instance the open loop FRF at G=0 to a closed loop FRF with G=10. But at higher frequencies where the open loop locus depicted in Figure 4.3 enters the unit circle an increase in amplitude and a steeper phase transition appears. Although effective for a closed loop FRF with G=10 this spillover effect is more obvious for a closed loop FRF with G=1000. The closed loop FRF with the stability limit feedback gain G=2220 intersects with the open loop FRF at 7075Hz that is the same

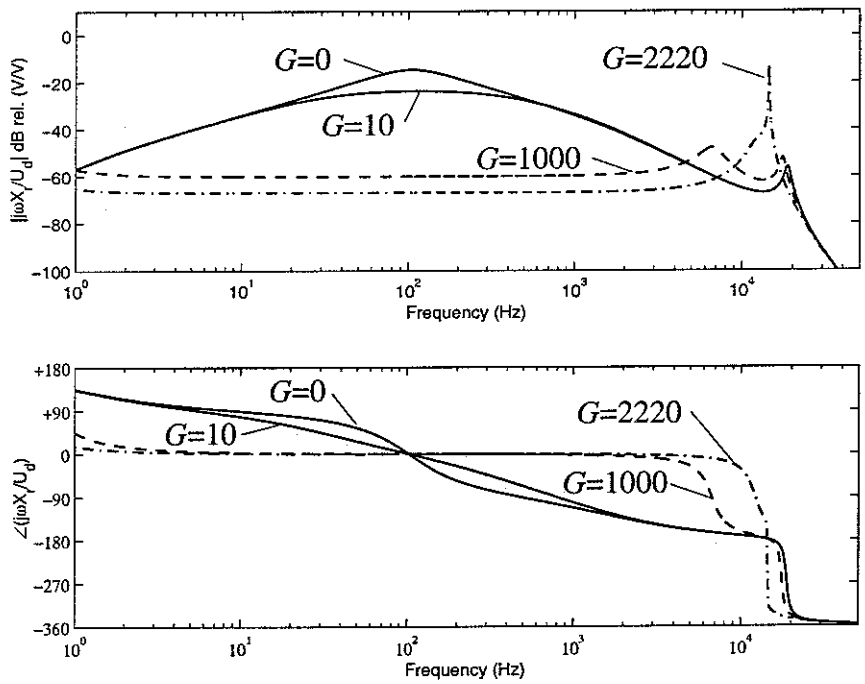

Figure 4.3: *Simulated Bode plot of the closed loop FRF from U_d to $\dot{X}_r$ with the model in figure 2.2 with feedback of $\dot{X}_r$ and different negative feedback gains G*

frequency at which the closed loop locus intersects the unit circle around the critical point in the Nyquist plot in Figure 4.3. At the frequency of 14400Hz where the closed loop FRF goes trough the critical point the Bode plot shows a sharp increase in gain and a steep phase transition. When using a larger feedback gain the closed loop FRF becomes unstable.

The stability limits for negative feedback of $\dot{X}_r$ are also found in the rootlocus plot. The rootlocus plot shows the pole position of the closed loop with increasing feedback gain G in the real-imaginary plane. The locus starts at the open loop poles for G=0 and goes to the open loop zeros for $G \rightarrow \infty$ or diverges. The closed loop poles are found by calculating the roots of $1+GH$, where H is the open loop FRF.

Figure 4.4 shows the rootlocus plot for negative feedback of the FRF $\dot{X}_r/U_d$ and a zoom at the origin. The open loop pole indicated by × at $-\omega_e=-2\pi f=-10991$ rad/s is the electrical, characteristic frequency. The open loop poles due to the accelerometer natural frequency are located at -4178.5+/-117910j and the poles of the natural frequency of the coil assembly are situated at -383+/-541j. An additional pole due to the integration model of the preamplifier is found close to the origin at $-\omega_{int}=-2\pi$. By increasing the gain G the accelerometer poles move towards the positive real half plane and at G=2220 they enter into the real half-plane. Poles in the positive real half plane are unstable as the transformation of the FRF into the time domain results into diverging positive exponential functions. Hence for gains G>2220 the closed loop is unstable. The pole of the electrical frequency and one pole of the coil assembly approach each other and diverge then in the negative real half plane; the second pole of the coil assembly moves to one of the two zeros at the origin for infinite feedback gain G. Hence, as also the Bode plot indicates, only the additional poles at the natural frequency of the accelerometer generate instability. Although the accelerometer could be considered as an additional DOF of a mechanical system added to the coil assembly no additional zero between the two natural frequencies is visible since the relative displacement $x_{rel}=x-y$ is the accelerometer output as indicated in Appendix A. Therefore no zero-pole flipping as for instance mentioned by [4] is observable and the influence on a typical structure with several poles and zeros close to the imaginary axis where this flipping is observable could only be

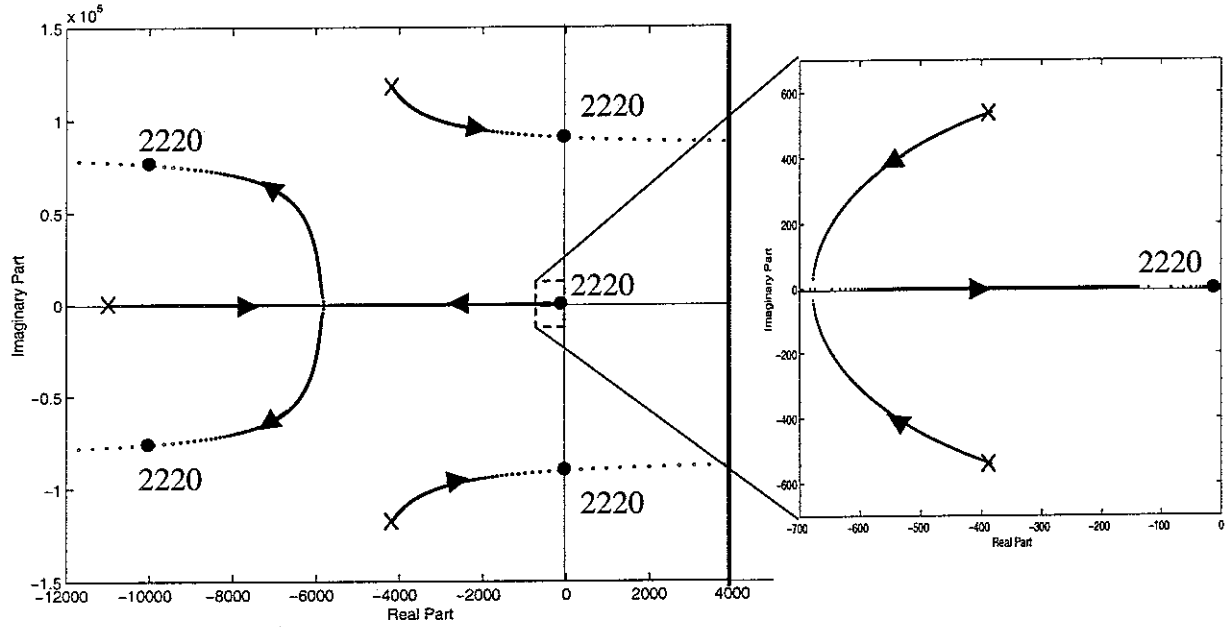

Figure 4.4: *Rootlocus plot of* $1+G\ \dot{X}_r/U_d$ *for negative feedback of* $\dot{X}_r$*; crosses: open loop pole position; points: pole position at the indicated gain; arrows: pole movement with increasing gain G*

investigated by adding another mechanical DOF. In order to generate unconditional stability for the closed loop, a compensator in the region between the accelerometer poles and the imaginary axis can add zeros. For instance a notch filter with two zeros located near the accelerometer poles could be used. Possible lack in robustness of the notch filter is not important as the accelerometer poles are not close to the imaginary axis.

4.2 Implementation of velocity feedback control

The velocity feedback is obtained in practice by closing the loop between the preamplifier output that is proportional to the coil assembly velocity measured by the accelerometer and the voltage input of the shaker as shown in Figure 4.5. Hence, in contrast to Figure 4.1 there is no separate primary and secondary force applied on the shaker mass, but the shaker FRF Ψ/Z_e is used to generate a force from the sum $u=u_d+u_{fb}$ of the disturbance voltage u_d and the feedback voltage u_{fb}. The second power amplifier DC300 implements negative feedback. The disturbance signal is generated by the signal generator of a FFT analyser that is also used to measure the shaker velocity.

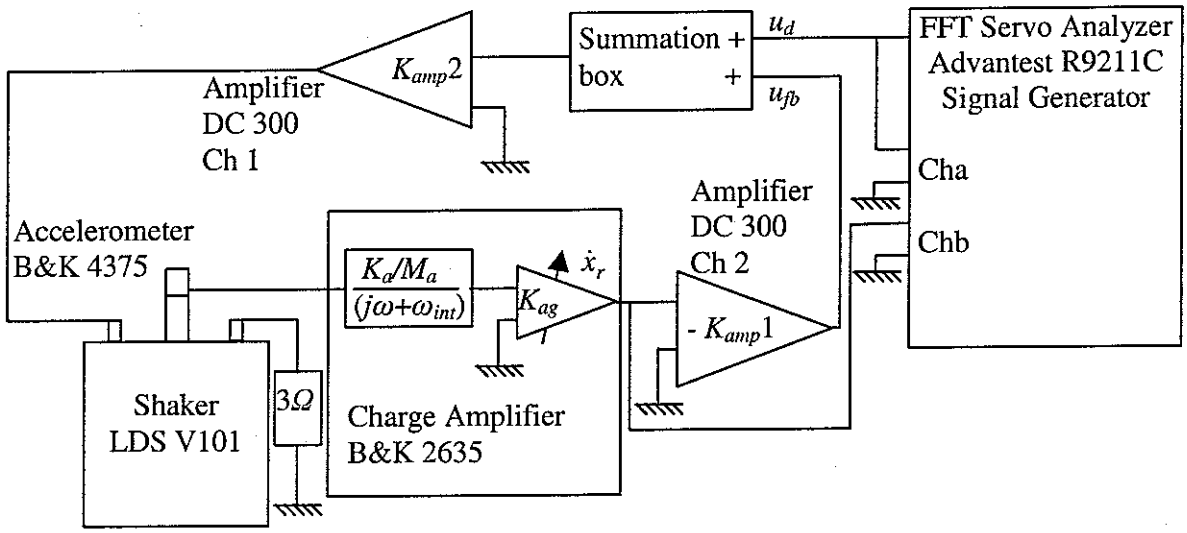

Figure 4.5: *Circuit for closed loop measurements*

Figure 4.6 depicts the frequency response function (FRF) source voltage measured in channel a to measured velocity measured in channel b for negative feedback and several values of the feedback gain $K_{amp}1$ compared to the open loop case. The DC amplifier gain $K_{amp}2$ adds an additional constant open loop gain so that the reduction in dB differs from the one depicted in Figure 4.3. The graph shows for three values of the feedback gain $K_{amp}1$ that by increasing the gain, damping can be increased in comparison to the open loop case that is also depicted. Dashed lines indicate simulations. Measurements and simulations fit well for frequencies between about 5 Hz and 1000 Hz. For higher feedback gains a peak appears at about 2500Hz. This is not surprising as differences between measurements and simulations have also been observed during the open loop identification in the zoom in Figure 3.4 between 1000 and 3000 Hz. Additionally a very low frequency displacement of the shaker is observed, but not measured at G=20. A limit for active damping by measured velocity feedback is hence not given by the accelerometer natural frequency but by shaker dynamics well below this frequency and by the integrator electronics at high gains and very low frequencies.

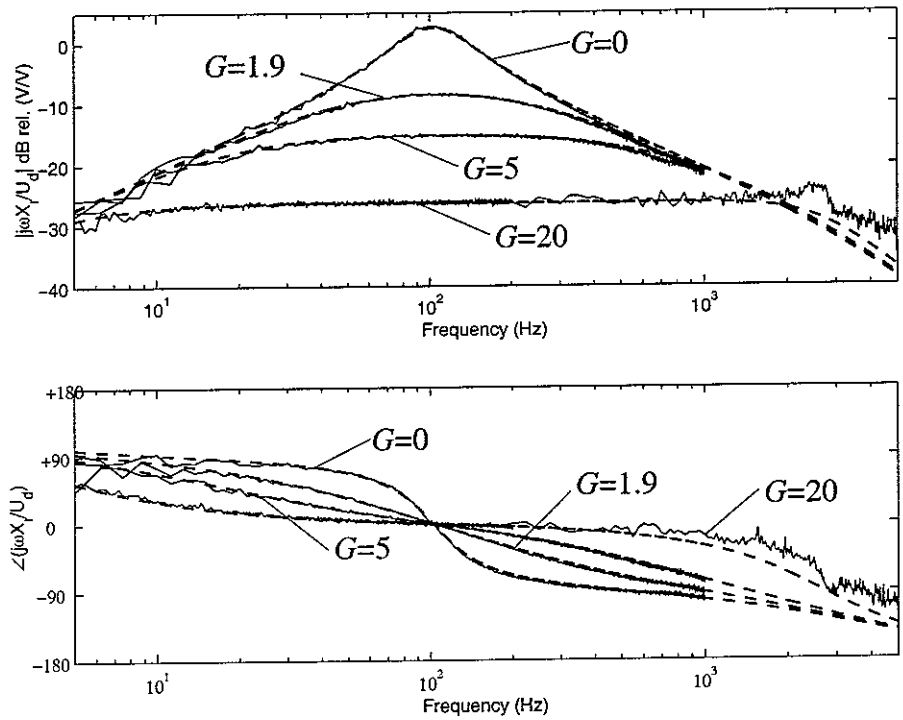

Figure 4.6: *Bode plot of the measured (solid) and simulated (dashed) FRF from U_d to $\dot{X}_r$ for the open loop case G=0 and negative feedback gains* 1.9, 5 *and* 20

The Nyquist plot in Figure 4.7 of the source voltage – velocity FRF with negative feedback compared with the open loop case also shows that damping is increased as the size of the resonance loop is decreased. Since very low frequency behaviour below 1Hz is not measured because of low coherence, it also indicates that the critical point at –1,0 is not encircled implying that higher gains could be implemented. As visual inspection clearly shows a low frequency vibration higher gains have not been implemented. Moreover correspondence between measurements and simulations is good around the first resonance frequency.

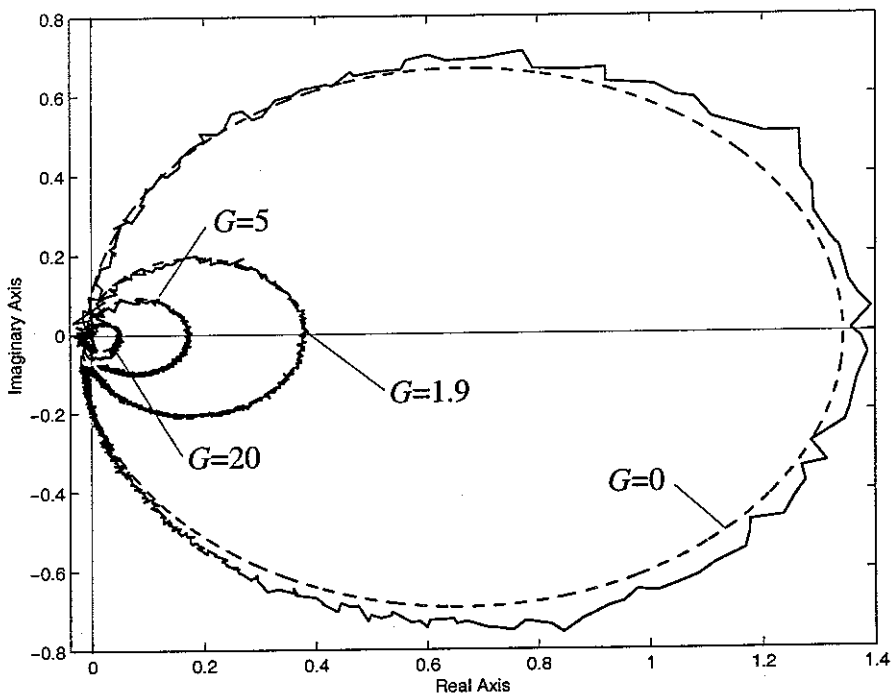

Figure 4.7: *Nyquist plot of the measured (solid) and simulated (dashed) FRF from U_d to $\dot{X}_r$ in the open loop case and for negative feedback gains 1.9, 5 and 20*

5. CURRENT FEEDBACK CONTROL

In contrast to Section 4 where the shaker has been purely used as an actuator and limits due to the measurement electronics have been found, in this section the shaker is considered as a self-sensing actuator. As the open loop FRFs of the self-sensing actuator have already been presented in Sections 2 and 3, the effects of current feedback on the closed loop are now investigated. Proportional current feedback should be similar to absolute velocity feedback since the back-EMF is proportional to the absolute velocity in this case where the base of the shaker can be considered as rigid and not vibrating. Hence, current feedback should show the damping effect of velocity feedback without needing an additional sensor. Also, collocation and thus stable control for large feedback gains should be guaranteed. However, the theoretical study presented in Subsection 5.1 shows practical limitations in this sense. In this subsection first the equivalent velocity feedback path and stability of the closed loop with current feedback are investigated using the Nyquist criterion. Second closed-loop simulations show the effect of proportional current feedback on the mechanical system. These effects are also explained by using the root locus plot. Finally in Subsection 5.2 proportional current feedback is implemented at the shaker and measurements are compared to simulations.

5.1 Proportional current feedback theory

When proportional current feedback is implemented the open loop FRF depicted in Figure 3.2 is modified by a proportional current feedback gain G inside the open loop $\dot{X}_r/U_d$ as depicted in Figure 5.1. The feedback gain G then also incorporates the current measurement gain K_{PR} due to an additional power resistance.

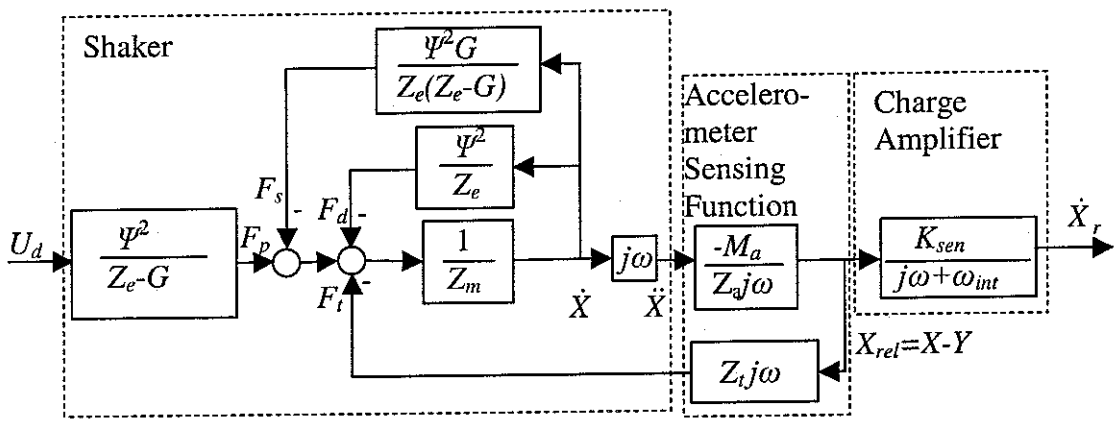

Figure 5.1: *Closed loop FRFs for current feedback*

In the previous sections a disturbance voltage u_d has been used to generate a primary force f_p. Thus instead of using a force sensor to measure f_p the disturbance voltage u_d is measured. This is reasonable as long as the FRF between U_d and F_p stays constant for different feedback gains. But Figure 5.1 shows that F_p depends on the current feedback gain G. Thus by implementing current feedback not only the total feedback force F_d+F_s is modified by an additional secondary force F_s but also the primary force F_p generated from a disturbance voltage U_d changes. Hence, in order to validate all FRFs of the direct current feedback theory in an experiment a primary force has to be exerted on the mechanical structure by a mechanism that is different from the force generation by this shaker. Since it is not practical

to link two shakers directly without an intermediate structure the mechanical FRF from the primary force F_p to the measured velocity $\dot{X}_r$ is only investigated by simulations for the system in Figure 2.1 without additional force sensor. Nevertheless other measurable, coupled FRFs are also verified by measurements

5.1.1 Limitations to proportional current feedback

Figure 5.1 indicates that the sum of the passive F_d and active F_s feedback force

$$F_d + F_s = \frac{-\Psi^2}{Z_e - G}\dot{X} = \frac{-\Psi^2/L}{(R-G)/L + j\omega}\dot{X} \tag{5.1}$$

is proportional to a low pass filtered velocity signal for proportional current feedback. Therefore it cannot be assumed that proportional current feedback is direct velocity feedback for the mechanical FRF $\dot{X}/F_p$. The first order low pass filter has a gain dependent cut-off frequency at $\omega_{co}=(R-G)/L$. As G does only influence the denominator a trade-off between velocity feedback amplitude and cut-off frequency of the feedback low-pass filter appears as illustrated in Figure 5.2. For negative feedback gains the amplitude of the velocity feedback FRF decreases. For positive feedback gains the impedance is reduced by subtracting the feedback gain from the resistance value so that a negative output impedance amplifier is implemented. Then the amplitude of the velocity feedback FRF increases, but the cut-off frequency is also reduced.

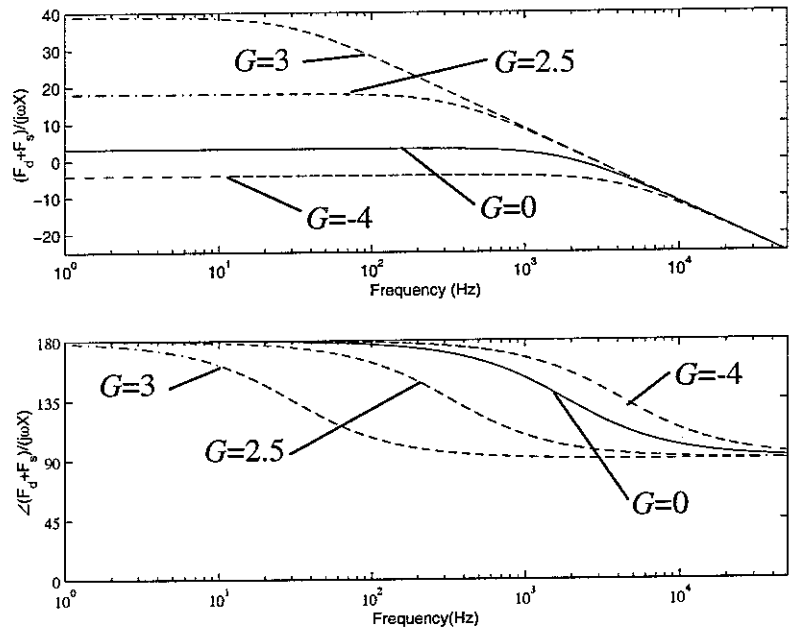

Figure 5.2 : *Force velocity feedback FRF for different direct current feedback gains G=-4, 2.5, 3 compared to the open loop case G=0*

When the current feedback gain G is greater than the resistance R the feedback FRF becomes unstable as its pole is positive. Therefore current feedback for a shaker can only be used for gains smaller than the electrical resistance R. As described in section 2 there is already a

passive damping force $F_d = \frac{\Psi^2}{Z_e}\dot{X}$ for G=0 due to electromagnetic coupling. Feedback gains smaller than 0 reduce this electrical damping and negative damping is introduced by using negative current feedback gains. Therefore current feedback gains that lead to additional positive damping lie in the range between 0 and $+R$.

In the limiting case $G \rightarrow +R$ equation (5.1) tends to negative displacement feedback as then the feedback velocity $\dot{X}$ is integrated. This is equivalent to adding stiffness to the mechanical system. In the same way a first order low-pass filter can be considered as an integrator above its cut-off frequency. Figure 5.2 indicates that below the cut-off frequency ω_{co} damping is added whereas for greater frequencies displacement feedback leads to additional stiffness.

Proportional current feedback has the same effect on the open loop electrical FRF $I/U|_{ol}$ in equation (3.3) as a resistance since an additional voltage $U_{FB}=GI$ proportional to current is added. In contrast to the passive choice of the resistance the resistance easily tuned with the gain G can become negative and hence cancel the coil resistance so that the effective resistance seen by the mechanical system becomes very small. The closed loop FRF

$$\frac{I}{U_d} = \frac{I/U_d\big|_{ol}}{1 - G\,I/U_d\big|_{ol}} = \frac{(Cj\omega)^2\left[\tilde{Z}_m\left(\tilde{Z}_e Z_{e2} - (Lj\omega)^2\right) + \Psi^2 jZ_{e2}\omega\right]K_{PR}}{(Z_{e1} - G)(Cj\omega)^2\left[\tilde{Z}_m\left(\tilde{Z}_e Z_{e2} - (Lj\omega)^2\right) + \Psi^2 jZ_{e2}\omega\right] - Z_{e2}\tilde{Z}_m} \qquad (5.2)$$

has a minus sign in front of the feedback gain due to the assumed positive feedback in Figure 5.1. Therefore negative feedback gains indicate an increased resistance whereas positive feedback gains mean a reduced resistance. Additionally if R=G the denominator in equation (5.2) becomes very small and the closed loop gain very high so that stability problems might arise.

In Figure 5.3 the Nyquist plot of the open loop FRF of equation (3.3) is depicted multiplied by different open loop gains G. The open loop is multiplied by negative gains for positive current feedback that is assumed in Figure 5.1, equation (5.1) and equation (5.2).

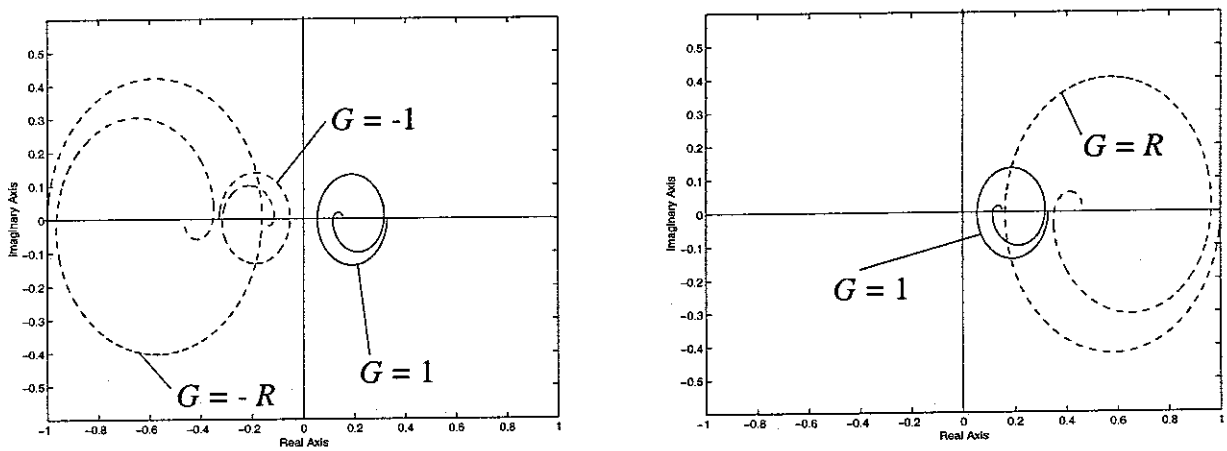

Figure 5.3: *Nyquist plot of the open loop FRF I/U multiplied by different gains G = -R, G = -1, G = 1 and G = R*

For G>=0 (negative current feedback) the open loop is unconditionally stable as is highlighted for instance for G=1 and G=R on the right side of Figure 5.3, but if G<0 (positive current feedback) the locus flips into the negative real half plane as is shown for instance for G=-1 and G=-R on the left side of Figure 5.3. In the latter case the closed loop amplitude I/U_d is predicted to increase over the whole frequency range. For gains greater than R the locus starts left of the critical point (-1,0) and the closed loop is predicted to become unstable. Additional stability limits are not found by this method. In the next section closed loop simulations verify the stability limit and show the influence of stabilizing gains on all closed loop FRFs.

5.1.2 Closed loop simulations

Figure 5.4 shows the Bode plot of the closed loop FRF in equation (5.2) for different negative feedback gains G. As predicted in section 5.1.1 the equivalent resistance is increased by increasing $|G|$ so that at higher gains the FRF tends to a pure real behaviour dominated by the equivalent electrical resistance. Moreover the influence of the mechanical system on the electrical FRF due to coupling is reduced for increasing $|G|$. Both the phase plot and the gain plot show that for high frequencies the response tends towards a purely resistive behaviour so that neither eddy currents nor capacitance effects are important for high negative feedback gains. Negative current feedback is not advantageous for sensing the behaviour of the mechanical part because the coupling effect becomes negligible. Additionally it is also not advantageous for the actuation because the amplitude of the closed loop FRF decreases i.e. a higher voltage has to be applied in order to obtain a set current.

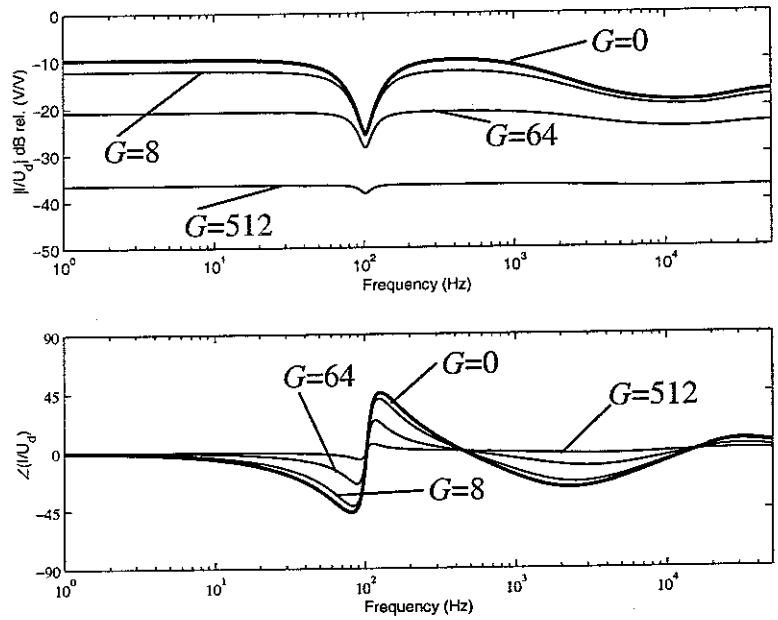

Figure 5.4: *Predicted Bode plot of the FRF disturbance voltage U_d to shaker current I with negative feedback gains G= 8, 64, 512 compared to the open loop case G=0*

Figure 5.5 depicts the Bode plot of the same FRF for different positive feedback gains G. As the FRF becomes unstable for G>R only values of G < 3.05 are considered. The Bode plot shows an additional resonance peak appearing at about 437 Hz that becomes steeper for increasing gains. The resonance is also visible in the phase plot where a -180° phase shift

appears whose phase transition becomes steeper by increasing gains indicating that damping is reduced. This resonance is due to the interaction between the electrical characteristic frequency and the mechanical natural frequency as will be described in section 5.1.3. The trough at the mechanical resonance frequency then behaves as a zero with a positive 180° phase shift. The integrative behaviour at lower frequencies only appears at gains very close to the stability limit. High frequency behaviour is not changed significantly except for the increased gain due to the bigger resistance also predicted in section 5.1.1. A node appears at higher frequencies in the phase plot where no change in phase shift is possible.

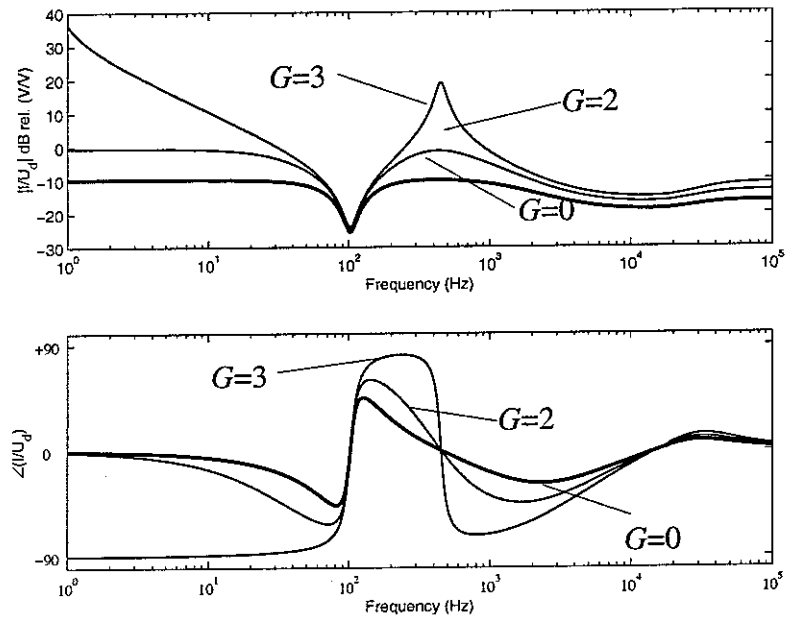

Figure 5.5: *Predicted Bode plot of the FRF disturbance voltage U_d to shaker current I for positive feedback gains G=2,3 compared to the open loop FRF with G=0*

Once a stability limit has been found it is interesting to see how much additional vibration reduction is possible. Figure 5.6 shows the Bode plot of the FRF from the primary force F_p to the measured vibration velocity $\dot{X}_r$ for different positive gains G in the stable region. As in the FRF I/U_d it also shows an additional resonance appearing at 437 Hz. However, the mechanical resonance at about 100 Hz is reduced by positive current feedback. This is due to additional damping as indicated by the decreasing steepness of the first −180° phase shift in the phase plot. Thus an optimum value for the controller gain appears where the increased amplitude at the additional resonance is equal to the reduced amplitude at the mechanical resonance frequency. Vibration reduction up to 8 dB at G=2 is simulated. Moreover positive current feedback has negligible influence on the high frequency behaviour beyond the characteristic electrical frequency. An influence on frequencies below the mechanical, natural frequency is only visible for gains close to the stability limit as has also been found at the FRF I/U_d.

Negative current feedback leads to reduced damping at the FRF $\dot{X}_r/F_p$. Moreover there is no significant influence at low and high frequencies and the FRF tends to the open loop mechanical FRF $\dot{X}_r/F_p|_{i=0}$ without influence of the shaker i.e. without back-EMF effect. This

is explained by the very high gains that lead to a very high equivalent electrical resistance so that it dominates over the back-EMF effect in the electrical circuit as illustrated in Figure 5.4.

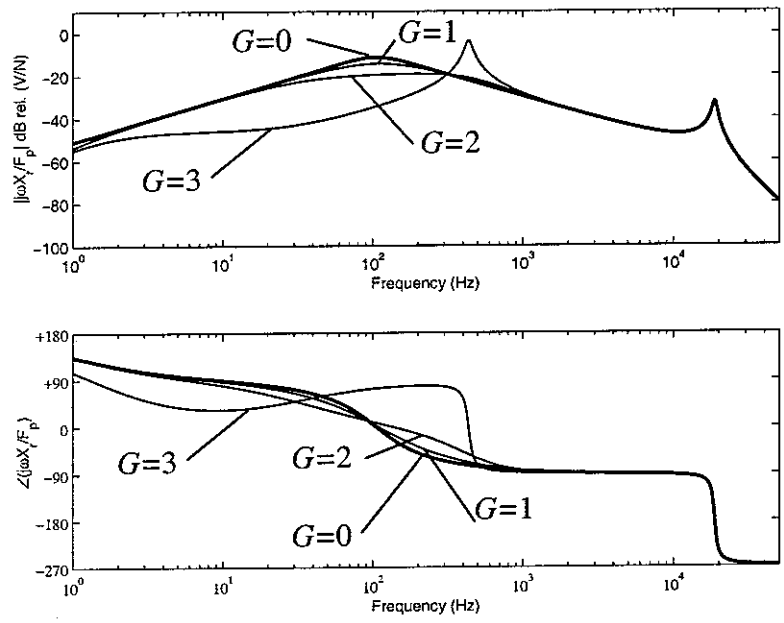

Figure 5.6: *Bode plot of the FRF from the primary force to the measured velocity for positive current feedback gains G=1,2,3 compared to the open loop FRF with G=0*

The presented FRF cannot be measured at the chosen shaker as no additional force sensor for the primary excitation f_p is available. Additionally as discussed in Section 4 the primary force is obtained by using an additional voltage input to the shaker. Thus the primary force is not independent of the positive current feedback gain. The FRF that can be measured is from the disturbance voltage U_d to the measured velocity $\dot{X}_r$ depicted in Figure 5.7 for different values of the positive current feedback gain G. Like in the two FRFs before an additional

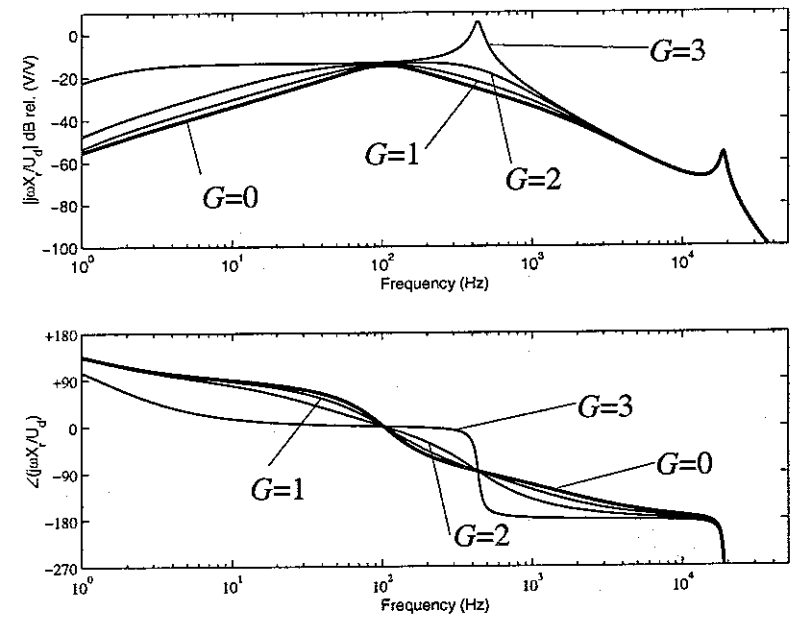

Figure 5.7: *Bode plot of FRF disturbance voltage to measured velocity with positive current feedback and feedback gains G=1,2,3 compared to the open loop FRF with G=0*

resonance appears at 437 Hz with increasing positive current feedback gain. But in contrast to the FRF $\dot{X}_r/F_p$ there is no reduction visible at the mechanical, natural frequency. On the contrary the amplitude is slightly increased. There is no influence visible at higher frequencies beyond the characteristic, electrical frequency. But there is a remarkable influence at lower frequencies, especially at gains close to the stability limit. The phase change is similar to the phase change of the FRF $\dot{X}_r/F_p$ with the exception of an additional –90° phase shift due to the low pass filter behaviour of the electrical part.

As also indicated by the FRF I/U_d at negative current feedback gains no additional damping can be added. Instead damping is reduced and the FRF tends to the open loop case $I/U|_{\dot{x}=0}$ without back-EMF effect for increasing gains. Due to the increased equivalent resistance the amplitude decreases in the whole frequency range.

In the next section an explanation for vibration reduction is given with reference to the root locus plot.

5.1.3 Explanation by the root locus

Figure 5.8 shows the roots of the denominator of the closed loop FRF $\dot{X}_r/U_d$ near the origin for increasing values of the positive current feedback gain G. As at least one pole stays in the positive real half plane for higher gains, i.e. the system does not become stable again for even higher feedback gains, gains only until G=2000 are plotted. Open loop poles are indicated by 'x'. As the output variable $\dot{X}_r$ of the considered FRF is not the feedback variable I it is not possible to determine closed loop pole positions from open loop zeros of the FRF $\dot{X}_r/U_d$. This indicates that implementing current feedback changes plant parameters rather than just controlling the output. The complex conjugate pole pair associated to the natural frequency of

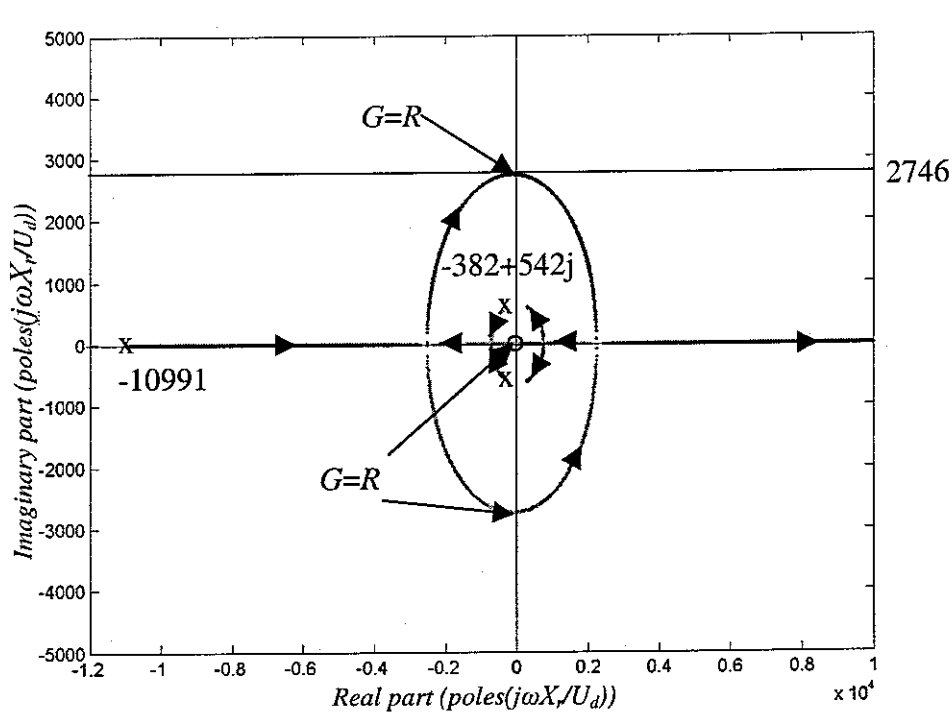

Figure 5.8: *Root locus plot of the FRF disturbance voltage U_d to measured velocity $\dot{X}_r$ for positive current feedback gains G = 1 to 2000; x open loop poles; zoom at origin*

the accelerometer and not shown in the figure does not change very much from the open loop pole position. It moves on an elliptic locus in direction of the imaginary axis. As the angle of a line from the origin to the pole position to the real axis is not decreased between the beginning and the final position no additional damping is added to this pole by implementing positive current feedback. Nevertheless the pole does not become unstable since it does not move into the positive real half plane.

Figure 5.8 also shows that with increasing positive feedback gain the open loop pole associated to the electrical part at about (–10991,0) moves towards the imaginary axis. The two mechanical shaker poles are also moved from their open loop position at (-382, +/-542j) in such a way that the angle between a line from the mechanical poles to the origin and the real axis is decreased. Thus damping of the mechanical resonance is increased. When the poles have reached the real axis the system is critically damped and the two mechanical poles move further on the real axis in opposite direction. At further increasing feedback gain the mechanical pole further away from the imaginary axis interacts with the electrical pole in such a way that the mechanical and the electrical pole move away from the real axis on a circular trajectory in direction of the imaginary axis. This new pole pair crosses the imaginary axis when G becomes equal to the electrical resistance R. Thus the same stability limit $G=R$ is found as before. The distance of the two poles when they cross the imaginary axis is equal to the additional resonance frequency that appears in the Bode plots simulated in Section 5.1.2. Because of the interaction and coupling between the poles it is not possible to say whether the new resonance is a mechanical or an electrical one. The region of stability is limited by the value of the resistance and the region of additional damping is even smaller and for the measured resistance relatively close to the stability limit. For robustness reasons it is advantageous to choose a higher passive resistance so that a small absolute change in resistance does not mean a large change in pole location. But Figure 5.4 implies that a high passive resistance leads to a relative low sensing effect. Hence, control robustness and sensing have to be traded off in an actuator design.

When comparing the pole positions of Figure 5.8 to the pole configuration of the controller

$$H(j\omega)=\frac{g}{\alpha}\frac{j\omega+1/T}{j\omega+1/(\alpha T)} \tag{5.3}$$

on page 79 in [4] both controller configurations become identical when assuming that the zero in [4] has moved to the origin i.e. $\alpha T=L/R$, $T>>1$ and $g/\alpha=-\Psi^2$. Thus the shaker can be considered as an analog lead compensator whose parameters can be adapted by adequately choosing its magnetic, geometric and electrical properties and thus the electrical parameters R and L. The zero cannot be moved as it is due to the derivation because of velocity feedback. Moreover the investigated shaker does not have a zero distribution of a typical mechanical structure with several mechanical natural frequencies so that the system configuration is different to the one given in [4]. For a study of the influence on the mechanical system these zeros should be considered. This can be carried out for instance by adding a plate or beam. Additionally as an electrical system is used for feedback a large variety of different controllers can be easily implemented electronically in order to change mechanical pole positions.

For negative current feedback the electrical pole stays stable as it moves far away from the mechanical poles for increasing gains. Thus it is easier to influence mechanical pole positions by positive current feedback than by negative current feedback. Additionally there is very small damping added to the accelerometer resonance frequency so that the influence of negative current feedback on the accelerometer pole position can be neglected. Moreover the damping of the shaker mechanical resonance frequency is reduced with increasing negative current feedback gains so that negative current feedback cannot be used for vibration reduction. In the next section some important, simulated results are verified by measurements at the identified shaker.

5.2 Implementation of direct current feedback control

For practical implementation of current feedback in contrast to identification measurements DC amplifiers are used in order to avoid the high pass filter characteristics of audio amplifiers. Additionally in order to prevent damage to the shaker a fuse and an ammeter are used that introduce an additional, minor resistance in the electrical circuit. Therefore the motional impedance influence of the open loop FRF is reduced and the FRFs are shifted by a gain relative to the identified FRFs in section 3. A self-made, passive resistance bridge in Figure 5.9 replaces the summation box in Figure 4.5. Figure 5.9 shows that the voltage drop at the power resistance of 3 Ω proportional to the current is amplified and is directly fed back and summed up to the disturbance voltage. In addition either the velocity of the coil assembly is measured via the accelerometer and its amplifier in order to estimate the possible vibration reduction or the voltage drop at the power resistance is measured in order to measure the FRF I/U_d. Measurements and signal generation are once again carried out with the FFT Servo Analyzer.

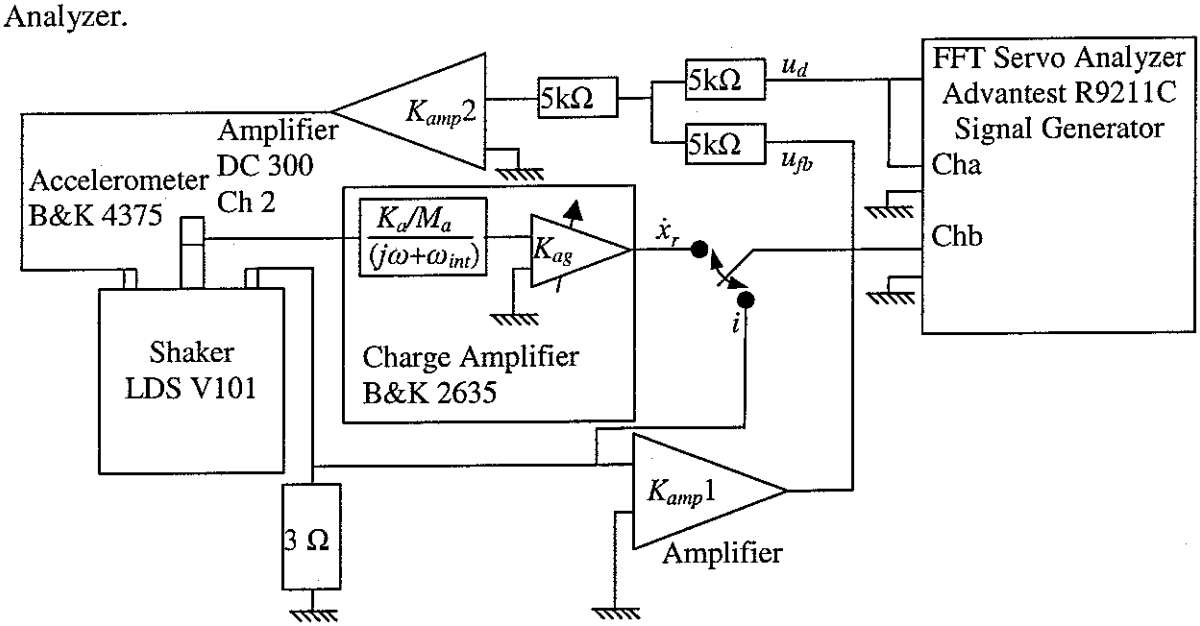

Figure 5.9: *Circuit for closed loop current feedback measurements*

Figure 5.10 shows the bode plot of the FRF from the disturbance voltage to the measured velocity for different positive current feedback gains compared to the open loop case for simulations and measurements in the frequency range from 1 to 1000 Hz. Both measurements and simulations show the characteristic additional resonance both in the amplitude plot and in the phase plot. The peak can be simulated well if the inductance is changed to L=0.4847mH

and the coil resistance to $R=6\Omega$ due to the additional measurement power resistance. Moreover at very low frequencies measurements and simulations are very different due to a lack in coherence as it has also been observed in identification measurements. For higher gains the coherence between the excitation voltage and measured velocity is reduced, which is visible by the noisy curve for $G=5.7$.

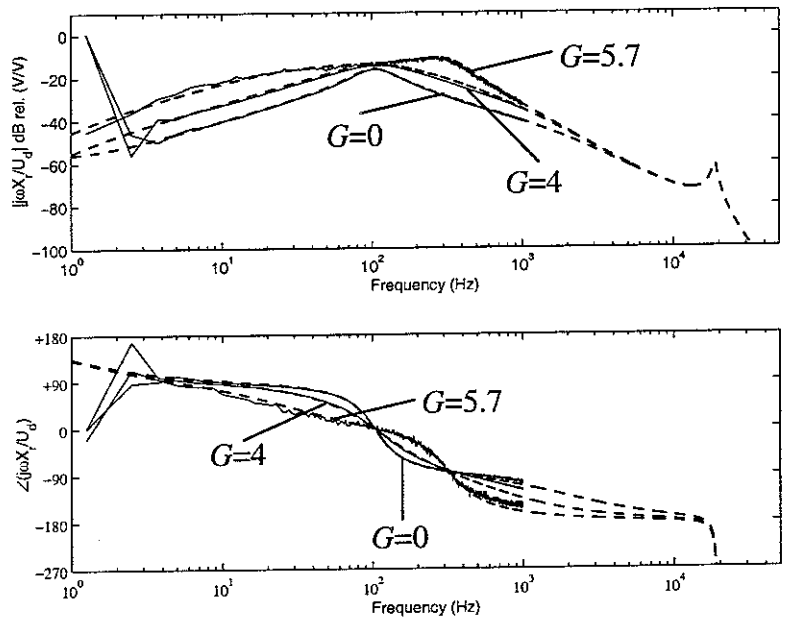

Figure 5.10: *Simulated and Measured FRF from the voltage disturbance U_d to the measured velocity $\dot{X}_r$ for different positive current feedback gains G= 4 and G= 5.7 compared to the open loop FRF with G=0*

Similar observations are true for the bode plot of the FRF from the disturbance voltage to the current depicted in Figure 5.11 where measurements and simulations agree reasonably well

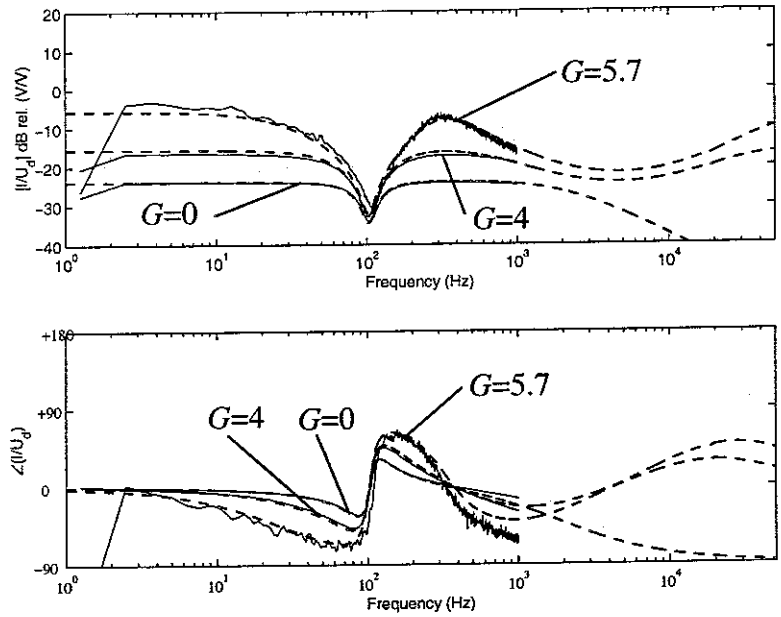

Figure 5.11: *Simulated and Measured FRF from the voltage disturbance U_d to the current I for different positive current feedback gains G = 4 and G = 5.7 compared to the open loop FRF with G = 0*

for frequencies below the mechanical natural frequency but are slightly different for higher gains and frequencies. At the mechanical resonance frequency the coherence of the input and output signal is reduced due to the steep peaks in the curve and thus measurements are not reliable at the mechanical resonance frequency. High frequency behaviour has not been checked because, as simulations have shown, the high frequency area is not interesting for vibration reduction by proportional, positive current feedback.

6. INDUCED VOLTAGE FEEDBACK CONTROL

Instead of feeding back a voltage proportional to the whole current that also contains components not related to the coil velocity, in this section a way to feed back only the voltage proportional to the coil velocity (induced voltage) is investigated using an electrical bridge circuit depicted in Figure 6.1. Section 6.1 reviews the characteristics of such a bridge circuit and compares proportional current feedback to induced voltage feedback. In section 6.1.1 simulated changes of bridge parameters indicate that both control schemes implement the same feedback force if no compensator for the coil inductance is implemented in a so-called Wheatstone bridge. A bridge with an ideally balanced resistance and inductance, a so-called Owens bridge, does only differ from ideal velocity feedback by the shaker actuation characteristic. Section 6.1.2 describes the only benefit of using a Wheatstone bridge to generate the feedback signal in comparison to proportional current feedback i.e. that the first one is unconditionally stable. Using an Owens bridge induced voltage feedback becomes conditionally stable again, but section 6.1.3, presenting closed loop simulations, shows that far higher vibration reduction, comparable to the velocity feedback case, becomes possible. Section 6.1.4 gives an explanation by means of the root locus plot and stresses the importance and practical difficulties of compensating for the coil inductance. Moreover it indicates that proportional current and induced voltage feedback with inductance compensation become identical when also in the proportional current feedback scheme the inductance is removed by using a negative inductance amplifier. Section 6.2 compares measurements and simulations for the non-compensated and compensated induced voltage feedback control. It indicates the importance of a well-tuned bridge circuit.

6.1 Induced voltage feedback theory

Before being able to feed it back, the voltage proportional to velocity has to be estimated from the measured voltage. For this purpose a complex bridge including a compensation for the coil inductance by a complex impedance is added to the circuit in Figure 5.1. As depicted in Figure 6.1 a general bridge circuit consists of four electrical impedances Z_1, Z_2, Z_3 and Z_4.

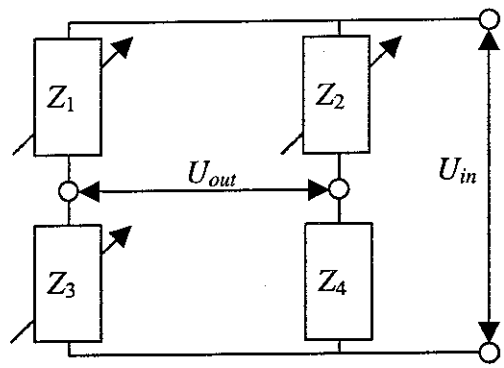

Figure 6.1: *General bridge circuit for the measurement of an impedance Z_4 by using known impedances Z_1, Z_2 and Z_3 to bring the output voltage U_{out} to zero at a given input voltage U_{in}*

Two pairs of impedances, the left pair Z_1, Z_3 and the right pair Z_2, Z_4, are connected in parallel relative to an input voltage U_{in}. The output voltage U_{out} is in parallel to the upper pair Z_1, Z_2 and the lower pair Z_3, Z_4. Such a circuit is usually used to determine the value of the unknown impedance Z_4. When there is an input voltage to the bridge, the output voltage

$U_{out}=[Z_2/(Z_2+Z_4)-Z_1/(Z_1+Z_3)]\ U_{in}$ is zero if the term in brackets is zero. This is achieved if the bridge is balanced by varying Z_1, Z_2 and Z_3. In this case the value of Z_4 is given by $Z_4=Z_3Z_2/Z_1$ when the value of the other bridge impedances is known. In the used circuit Z_4 is replaced by the shaker so that $Z_4=Z_e$ and a term due to the induced voltage $U_i = \Psi \dot{X}$ appears in the FRF between the input voltage and the output voltage $U_{out}=[Z_2/(Z_2+Z_e)-Z_1/(Z_1+Z_3)]\ U_{in}$ + $Z_2/(Z_2+Z_e)\ U_i$. If now the term in brackets is zero, i.e. the bridge is balanced, the output voltage will be related to the induced voltage and thus to the coil velocity that is to be used for feedback. Figure 6.2 shows the closed loop FRFs when feeding back the output voltage of the bridge with shaker to its input with a feedback gain G. The additional bridge serves as an observer in such a way that the output signal of the bridge gives the induced voltage if the bridge is perfectly balanced.

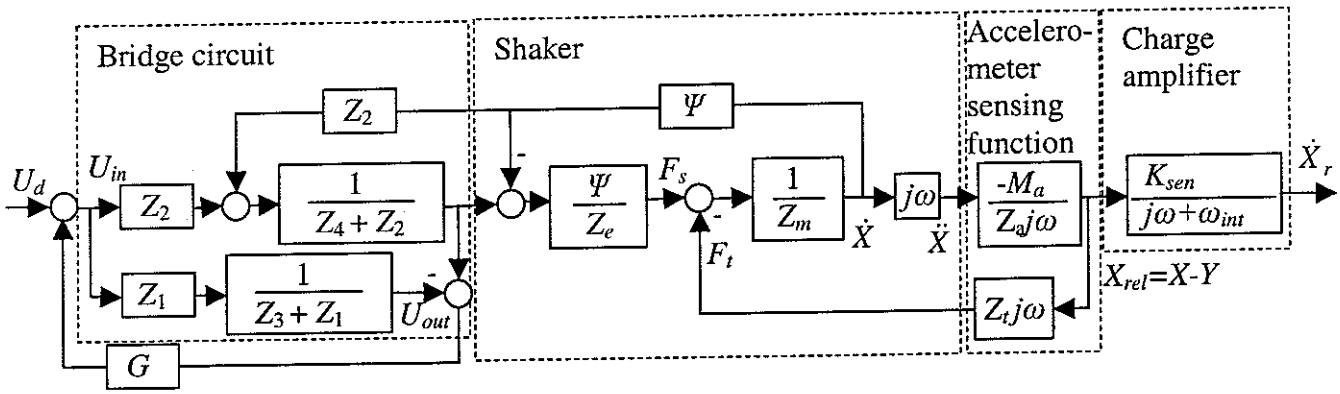

Figure 6.2: *Closed loop FRF's for induced voltage feedback*

In theory the bridge is ideally balanced if $Z_1=Z_2=Z_3=Z_e$. For this case Figure 6.3 shows the secondary force F_s including passive velocity feedback as function of the shaker velocity $\dot{X}$.

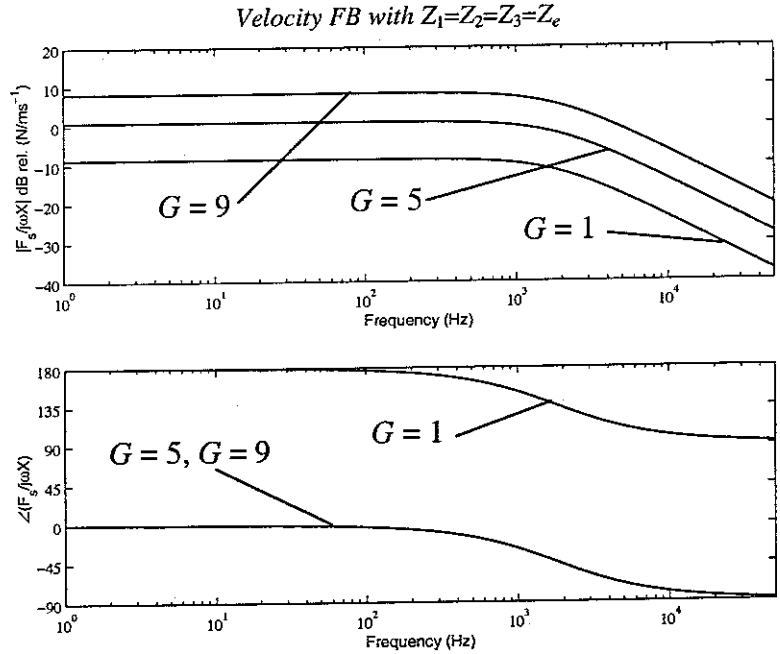

Figure 6.3: *FRF between the secondary force and the coil velocity for different feedback gains G and a perfectly balanced complex bridge circuit*

In this case an increased bridge voltage feedback gain G leads to increased velocity feedback amplitude. Moreover the cut-off frequency due to the shaker inductance does not move to lower frequencies as has been the case for pure current feedback. Thus there is no amplitude-bandwidth trade-off for the ideal case and induced voltage feedback is identical to velocity feedback until the characteristic electrical shaker frequency for a perfectly balanced bridge circuit.

6.1.1 Limitations to induced voltage feedback

In practice, however, there are at least two ways to balance the bridge. The first one uses an Owens bridge with $Z_1=1/j\omega C_2$, $Z_2=R_1$, $Z_3=R_3+1/j\omega C_3$. If the bridge is balanced a shaker impedance $Z_4=R_1C_3/C_2+j\omega C_2R_3R_1$ that is of the form of the coil impedance Z_e can be compensated. By varying R_1, when $C_2=C_3$, the resistive part of the shaker impedance is determined whereas by varying R_3 the inductive part of the shaker impedance is compensated. Considering an ideal resistance and inductance behaviour of the shaker coil the output voltage of the balanced Owens bridge is proportional to the induced voltage and hence the coil velocity. The second scheme uses a Wheatstone bridge where resistors R_1 and R_{eb} replace all outside complex impedances i.e. $Z_1=Z_2=R_1$; $Z_3=R_{eb}$. Then only the resistive part of the shaker impedance can be determined by varying Z_3 in such a way that the bridge is balanced for DC inputs. However, at AC inputs and higher frequencies a proportion of the input voltage is still fed through to the output so that no ideal induced voltage feedback can be realized.

In the first case, although $Z_3=R_3+1/j\omega C_3$ and $Z_1=1/j\omega C_2$ are tuned in such a way that $C_2R_3R_1=L$ and $R_1C_3/C_2=R$, $Z_2=R_1$ might be more or less well tuned to the static electrical impedance of the shaker. Figure 6.4 depicts the FRF from the coil velocity to the secondary force in this case for different feedback gains when R_1 changes by +/- 33 %.

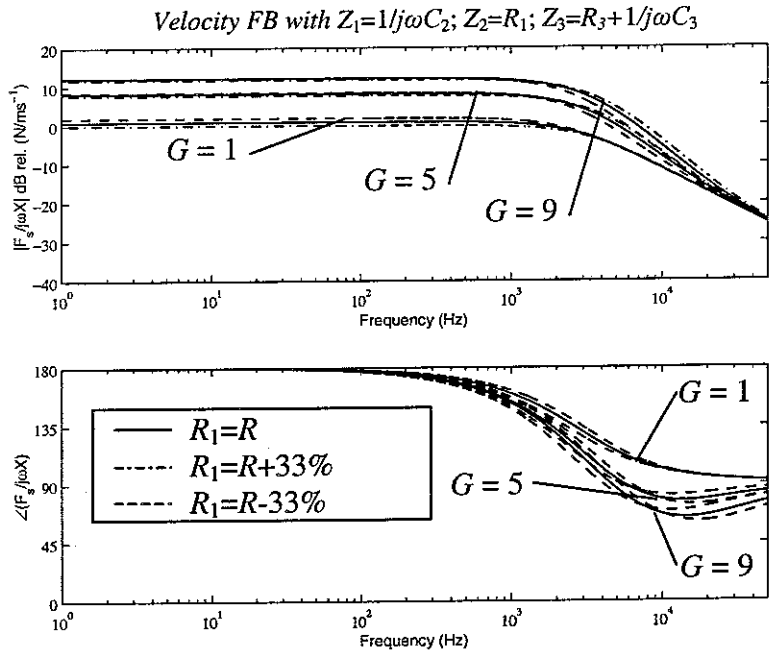

Figure 6.4: *FRF between the secondary force and the coil velocity for feedback gains G=1, 5 and 9 where R_1 varies by +/- 33%*

As the roll-off becomes steeper, using just a resistance instead of a complex impedance for R_1 seems to be advantageous. But the cut-off frequency changes slightly to lower frequencies for increasing gains so that an amplitude-bandwidth trade-off appears that nevertheless is smaller than in the pure current feedback case. Moreover variations in R_1 have only a small influence on the feedback force. Variation of R_1 is relatively less important for higher gains for frequencies lower than the cut-off frequency.

In the second case also Z_1 and Z_3 might just be more or less well-tuned resistances R_1 and R_{eb} instead of complex impedances so that a pure resistive Wheatstone bridge is realized. Figures 6.5 and 6.6 show the influence of a mistuned $Z_3=R_{eb}$, $Z_1=R_1$ and $Z_2=R_1$ at the example of feedback gains $G=1$ and $G=5$.

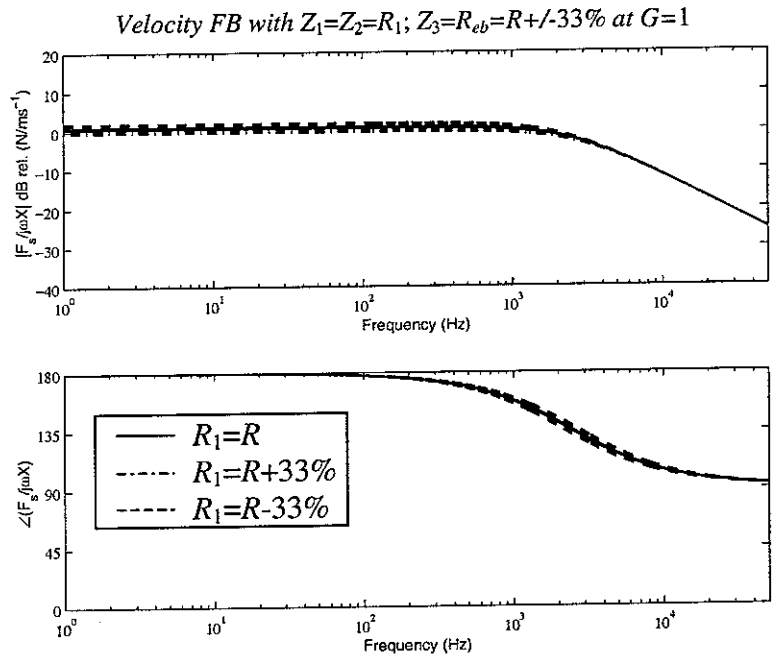

Figure 6.5: *FRF between the secondary force and the coil velocity for a feedback gain G=1 and variations in Z_1, Z_2 and Z_3 by +/- 33%*

For the small feedback gain $G=1$ parameter changes of either R_1 or R_{eb} only play a minor role. Moreover only a negligible bandwidth reduction is visible in Figure 6.5. At higher gains, e.g. $G=5$, however, changes in R_1 still have a negligible influence on the force feedback, but a reduction of the resistor R_{eb} leads to a clearly visible increase in bandwidth and reduction in feedback amplitude. The inverse is true for an increasing resistance value as depicted in Figure 6.6. It hence plays a similar role as the feedback gain for proportional current feedback.

Figure 6.3 and 6.4 are clearly different from the force velocity feedback FRFs simulated for direct current feedback depicted in Figure 5.2. They indicate that induced voltage feedback is advantageous compared to proportional current feedback, both for an ideally balanced complex bridge and for an Owens bridge with balanced inductance, as no bandwidth-amplitude trade-off appears.

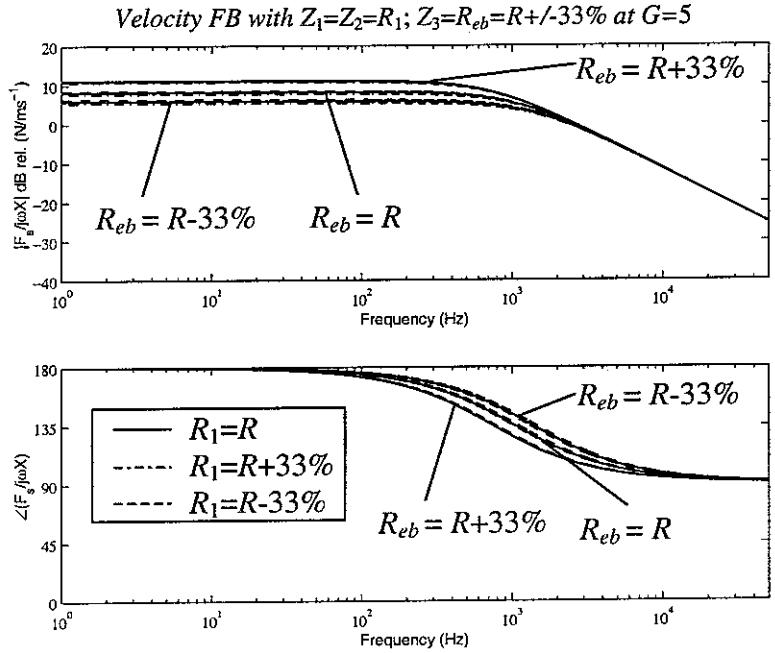

Figure 6.6: *FRF between the secondary force and the coil velocity for a feedback gain G=5 and R_1 and R_{eb} varying by +/- 33%*

Figures 6.7 and 6.8 compare the FRF from the coil velocity to the secondary force without passive damping effect of the induced voltage feedback to the case with proportional current feedback. Two different feedback gains are chosen and both R_1 and R_{eb} of an unbalanced Wheatstone bridge are varied. Figure 6.7 indicates that for a feedback gain G=4 a varying R_1 may lead to changes in the cut-off frequency of the induced voltage feedback, but that these changes are small in comparison to changes due to variations in R_{eb}. Moreover the curve for

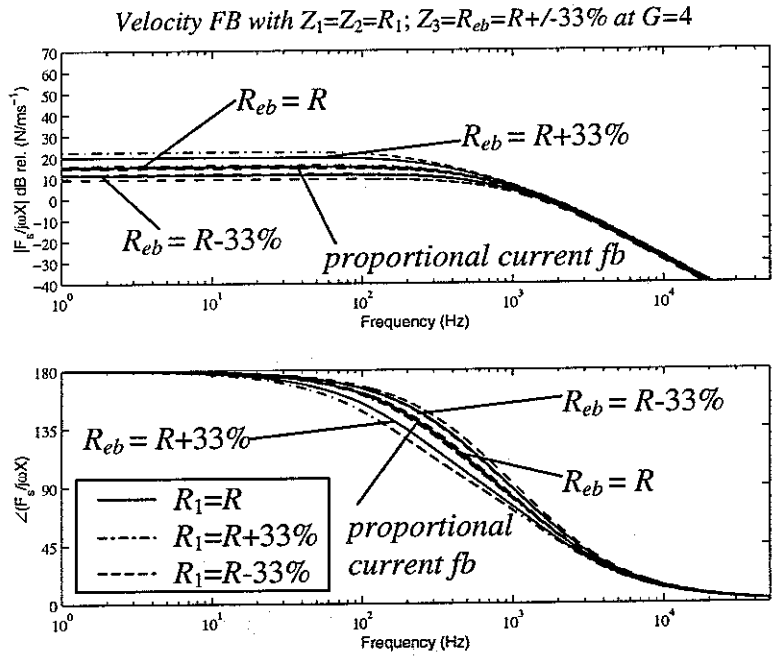

Figure 6.7: *FRF between the secondary force without passive damping and the coil velocity for a feedback gain G=4 and variations in R_1 and R_{eb} by +/- 33% compared to the proportional current feedback case*

proportional current feedback corresponds to the curve for a balanced Wheatstone bridge without balanced inductance i.e. R_{eb}=R. The FRF of an unbalanced bridge with variations in R_{eb} and R_1 is shown in Figure 6.8 for a higher feedback gain G=5. Since the proportional current feedback curve corresponds exactly to an induced voltage feedback curve when the bridge does not compensate for the shaker inductance and is not balanced i.e. R_1=R+33% and R_{eb}=R proportional current feedback is a special case of induced voltage feedback when feedback gains stabilize the feedback loop. By comparing Figures 6.7 and 6.8 it can be seen that changing R_{eb} has the same effect as changing the feedback gain G since changes in R_{eb} lead to similar curve shapes as changes in G.

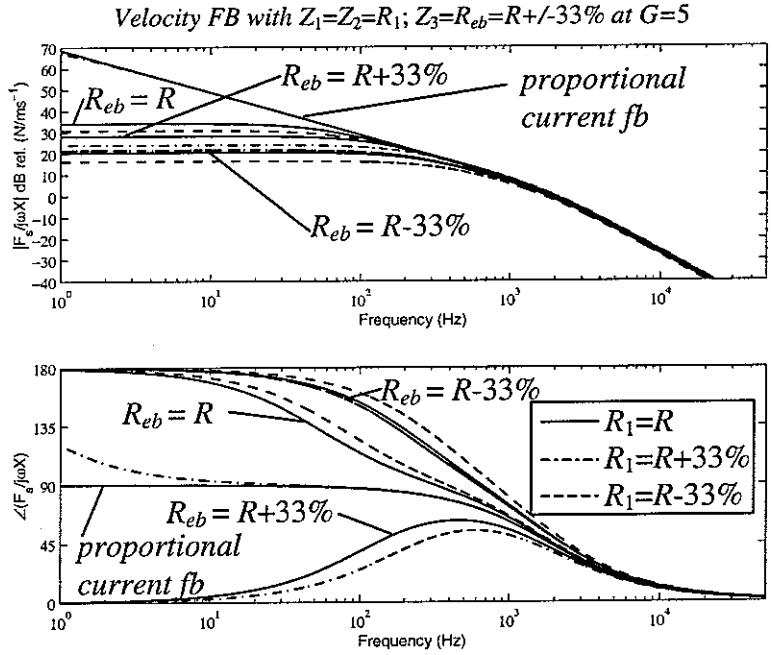

Figure 6.8: *FRF between the secondary force without passive damping and the coil velocity for a feedback gain G=5 and variations in R_1 and R_{eb} by +/-33% compared to the proportional current feedback case*

When varying R_1 on the estimation side of the bridge i.e. in the term $1/(Z_3+Z_1)$ once more a gain bandwidth trade-off appears that is similar to changing the resistance R_{eb} in the same term. But in contrast to direct current feedback at higher gains even rather large variations of R_1 do not lead to instability. In the following section stability is investigated for the case of the Owens bridge and the Wheatstone bridge.

6.1.2 Stability

For the ideally balanced Owens bridge the solid line in Figure 6.9 depicts the FRF between the bridge input U_{in} and the bridge output voltage U_{out} as Bode plot and in the Nyquist diagram. The bode plot looks comparable to the one of the measured velocity in Figure 3.3 except for the different behaviour at the accelerometer resonance frequency. In the case of the accelerometer the relative displacement between structure and accelerometer seismic mass is used do approximate the coil acceleration. Here the output voltage directly gives the FRF to the coil velocity so that no additional 180 degree phase shift appears in Figure 6.9. The Nyquist plot cannot be distinguished from the simulated plot in Figure 3.4 around the shaker

mechanical natural frequency. For an ideally balanced Owens bridge the output voltage thus is proportional to the coil velocity. In consequence the closed loop is only conditionally stable. Additionally for simplicity simulations in this section have been carried out neglecting eddy current effects that might add damping at the second natural frequency. This phenomenon due to a special actuator design will be discussed in Section 6.2 when comparing simulations to measurements. Figure 6.9 also indicates what happens if the value of the resistance of R_1 changes assuming that R_3 is varied so that the compensating inductance $L_e=C_2R_3R_1$ stays at the ideal value of the coil inductance where $C_2=C_3$ and hence R_1 determines the compensating resistance. The FRF (dashed dotted line in Figure 6.9) for small values of R_1 resembles a first order low pass filter due to the electrical resistance-inductance behaviour and the influence of the mechanical on the electrical system becomes negligible. For higher resistance values the locus (dashed line in Figure 6.9) flips into the negative real half plane leading to conditional stability.

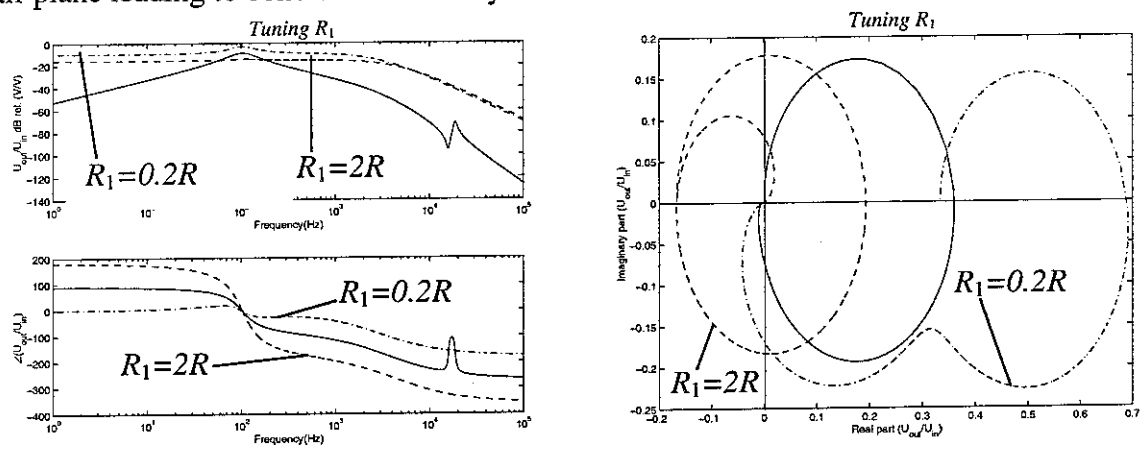

Figure 6.9: *Bode(left) and Nyquist (right) right plots of the FRF between the output voltage and the input voltage of the Owens bridge for R_1=0.2R (dashed dotted line), R_1=R (solid line), R_1=2R (dashed line)*

The inverse is observable when $Z_2=R_1$ and $Z_1=1/j\omega C_2$ vary even though $C_2R_3R_1=L$ and $R_1C_3/C_2=R$. Figure 6.10 depicting the same FRF as before for varying R_1 indicates that for low values of R_1 the locus approaches the instability point whereas high values (dashed line in Figure 6.10) do not destabilize the closed loop. Moreover a motional feedback trough instead of a peak may appear at the mechanical natural frequency for small resistance values in the Bode plot (dashed dotted line in Figure 6.10). The Nyquist plot shows that in the case of a balanced Owens bridge only very high gains similar to the velocity feedback case might destabilize the closed loop.

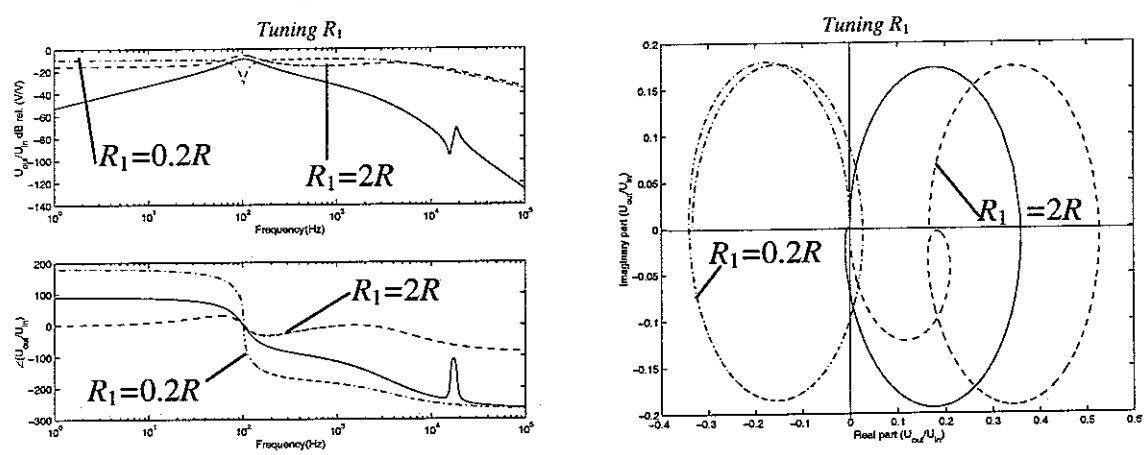

Figure 6.10: *Bode (left) and Nyquist (right) plot of the FRF between the output voltage and the input voltage of the Owens bridge for R_1=0.2R (dashed dotted line), R_1=R (solid line), R_1=2R (dashed line)*

If instead of an Owens bridge a pure resistive Wheatstone bridge is used unconditional stability results if only the bridge resistance is balanced with the internal coil resistance. Figure 6.11, showing the Bode plot and the Nyquist diagram of the FRF between the bridge input voltage and the bridge output voltage, highlights that the locus stays in the right half plane far away from the critical point –1,0 (solid line). Even for high feedback gains no stability problem is anticipated. But the Bode plot also shows that the accelerometer resonance may no longer be influenced, as no motional peak is visible in the Bode plot. Self-sensing damping hence is limited in bandwidth to the anti-resonance frequency also found as a resonance frequency in the proportional current feedback case. Figure 6.11 also shows the influence of a varying resistance R_{eb}. High resistance values (dashed line) still lead to conditional stability whereas small resistance (dashed dotted line) values do not influence stability. As in the case with balanced inductance L_e small resistance values for R_1 may lead to instability and a high R_1 just shifts the Nyquist plot further into the right real half plane.

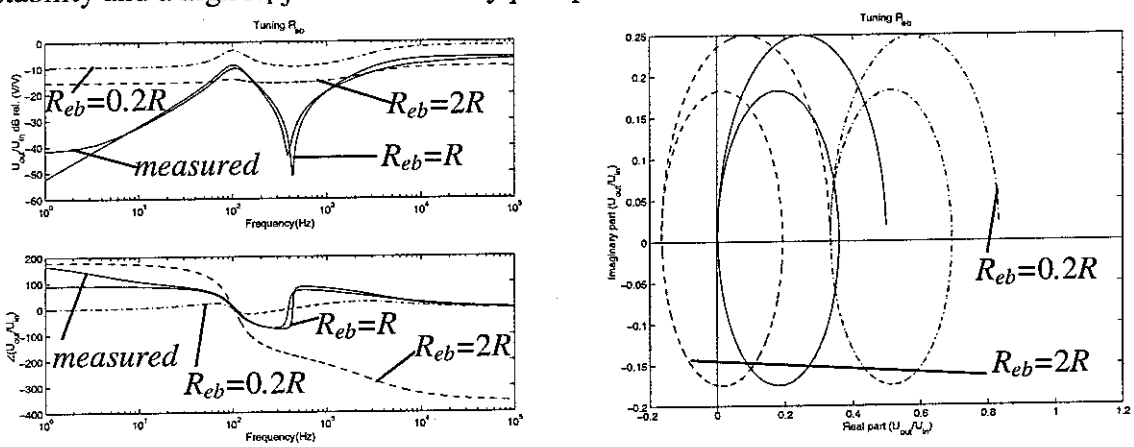

Figure 6.11: *Bode(left) and Nyquist (right) plot of the FRF between the output voltage and the input voltage of the Wheatstone Bridge; R_{eb}=0.2R (dashed dotted line); R_{eb}=R (solid line)* and *R_{eb}=2R (dashed line) compared to the measured FRF (solid line)*

In conclusion in contrast to proportional direct current feedback induced voltage feedback for a balanced purely resistive Wheatstone bridge is unconditionally stable, but the equivalent force feedback FRF shows the same amplitude bandwidth trade-off for both feedback schemes. Compensating for the coil inductance using a balanced Owens bridge then introduces conditional stability. Section 6.1.3 then compares the closed loop performance of the feedback schemes.

6.1.3 Closed loop simulations

Figure 6.12 shows the Bode plot of the FRF between the primary force input and the measured coil velocity for the open loop case and for different output voltage feedback gains when the Owens bridge is ideally balanced. This FRF is relevant for the assessment of vibration reduction when the structure is excited by a primary force. The plot also indicates that very high gains and very high damping is possible. Additionally the low frequency behaviour is only influenced at very high gains. Before this lower limit is important the high frequency amplification has to be considered as will be explained in section 6.1.4.

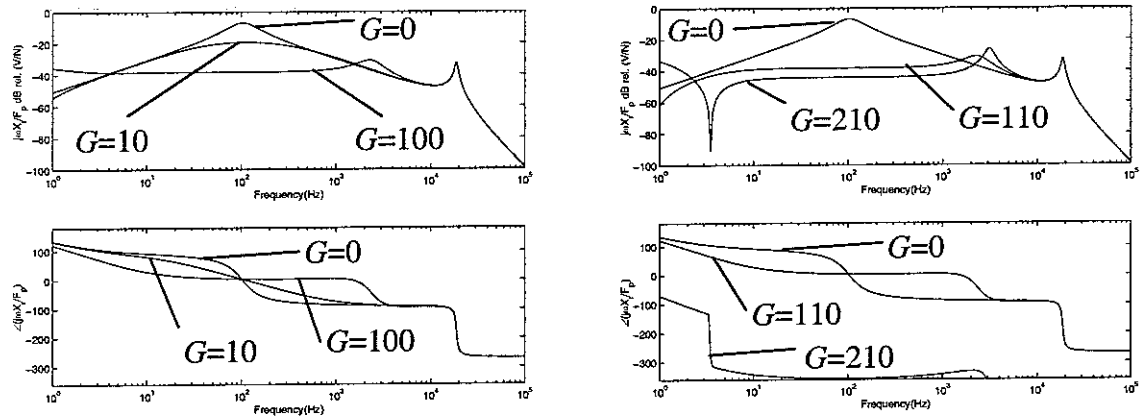

Figure 6.12: *FRF from the primary force to the coil velocity for output voltage feedback gains G=10, 100 (left) and 110, 210 (right) compared to the open loop G=0 when the coil inductance and resistance are compensated using an Owens bridge*

Figure 6.13 depicts the Bode plot of the FRF between the input voltage U_{in} and the measured coil velocity $\dot{X}_r$ in the open loop case and for different output voltage feedback gains when an ideally balanced Owens bridge is used compensating for the coil inductance. The plot indicates that very high gains leading to a high amount of damping can be realized without causing instability. Vibration reduction by 30 dB similar to the velocity feedback case seem to be possible. Nevertheless at very high gains vibration amplification appears at high frequencies and the accelerometer resonance is not damped. Section 6.1.4 gives an explanation for these findings using the root locus plot.

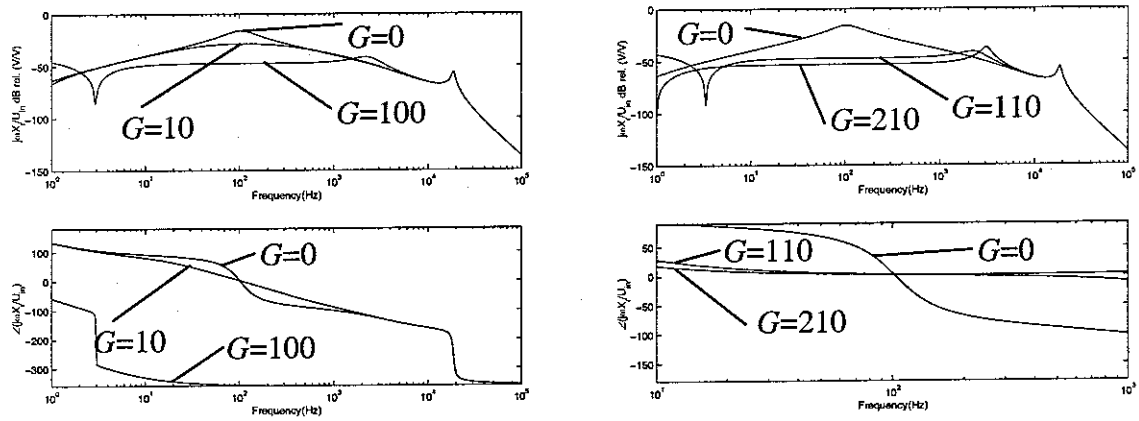

Figure 6.13: *FRF from the input voltage to the coil velocity for current feedback gains G=10, 100 (left) and 110, 210 (right) compared to the open loop G=0 when the coil inductance and resistance are compensated using an Owens bridge*

These very good results for an ideally balanced Owens bridge are to be modified if considering a pure resistive Wheatstone bridge that ideally compensates for only the coil resistance. In this case Figure 6.14 depicts the Bode plot of the FRF between the primary force and the measured velocity for different output voltage feedback gains compared to the open loop case when the resistive Wheatstone bridge is ideally balanced. As in Figure 6.13 an additional resonance peak appears that in contrast to the proportional current feedback case depicted in Figure 5.6 does not destabilize the closed loop, but it allows only rather small feedback gains and active damping values for vibration reduction up to about 15dB.

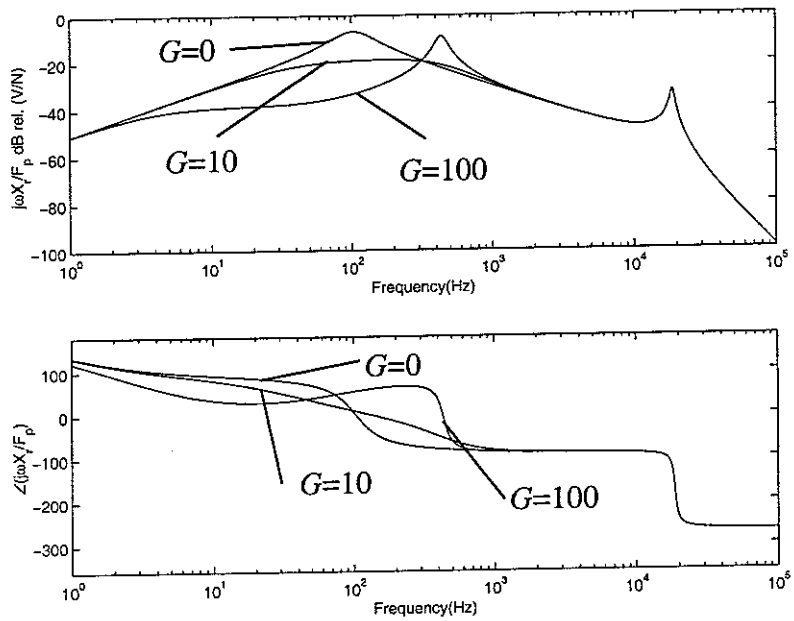

Figure 6.14: *FRF from the primary force to the coil velocity for output voltage feedback gains G=10 and G=100 compared to the open loop G=0 if the coil resistance is compensated using a Wheatstone bridge*

Figure 6.15 depicts the Bode plot of the FRF from the input voltage to the measured coil velocity for different induced voltage feedback gains compared to the open loop case. As in the proportional current feedback case an additional resonance peak at a characteristic frequency between the characteristic electrical and the mechanical resonance frequency appears. A phase transition of 180 degrees is observable at this characteristic frequency that corresponds to the frequency of the anti-resonance in Figure 6.11. Despite its resonant appearance it does not destabilize the closed loop as has been indicated by Figure 6.11.

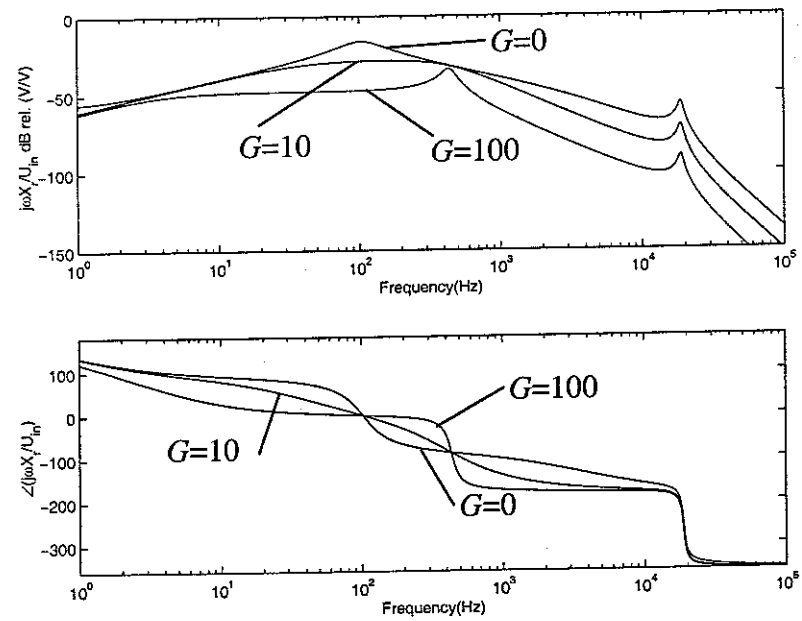

Figure 6.15: *FRF from the input voltage to the coil velocity for output voltage feedback gains G=10 and G=100 compared to the open loop G=0 when the coil resistance is compensated using a Wheatstone bridge*

After having presented the extreme cases ideal coil inductance compensation and no coil inductance compensation the investigation of the closed loop root locus plot in Section 6.1.4 gives an explanation for these and the intermediate cases with partially compensated coil inductance.

6.1.4 Explanation by the root locus

Figure 6.16 depicts the roots of the closed loop FRF between the Owens bridge input voltage and its output voltage for different induced voltage feedback gains when the Owens bridge is ideally balanced. Open loop poles are indicated by a 'x', open loop zeros are marked with an 'o'. Arrows indicate closed loop pole movement with increasing feedback gain. In comparison to the proportional current feedback root locus plot depicted in Figure 5.8 there is an additional electrical pole due to the compensating inductance of the Owens bridge and an additional zero between the poles of the natural frequency of the coil assembly and the poles of the natural frequency of the accelerometer due to the Owens bridge circuitry. The additional electrical pole moves to $-\infty$ on the real axis for increasing feedback gains and is of no further interest. But instead of returning to the real axis, as in the case of proportional current feedback, the two coil assembly poles tend towards the open loop zero for increasing gain after having interacted with the electrical pole and after having crossed into the positive real half plane. Hence stability considerations change significantly relative to the proportional current feedback case as higher feedback gains can be realized before instability occurs and the additional resonance lies at higher frequencies. The accelerometer pole still diverges into the real half plane for increasing feedback gains after having shortly interacted with the coil assembly poles so that the closed loop FRF does not become stable again for higher gains.

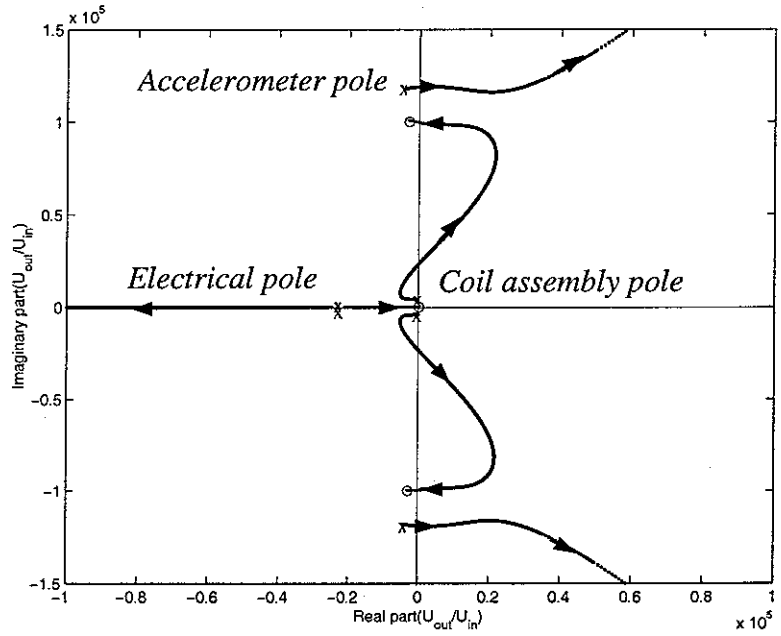

Figure 6.16: *Locus of the denominator roots of the closed loop FRF U_{out}/U_{in}, o open loop zeros, x open loop poles for L_e identical to the coil inductance*

Figure 6.17 shows the same plot if a purely resistive Wheatstone bridge is used not compensating for the coil inductance. In comparison to Figure 5.8 it is only the negative real half plane to which two zeros due to the Wheatstone bridge circuit are added close to the

imaginary axis and these zeros are responsible for the anti-resonance in Figure 6.11. As all poles are in the negative real half plane no stability limit is predicted. Moreover only one electrical pole due to the coil inductance is visible. The coil assembly poles move towards the additional zeros for increasing gains. As these zeros are very close to the imaginary axis the poles moving towards their position are lightly damped and a steep peak appears in the Bode plot in Figure 6.15 close to the frequency of the anti-resonance in Figure 6.11. For increasing gains this peak tends to become very low damped, but it is not predicted to become unstable. In comparison to Figure 6.16 the additional resonance frequency is also at much lower values.

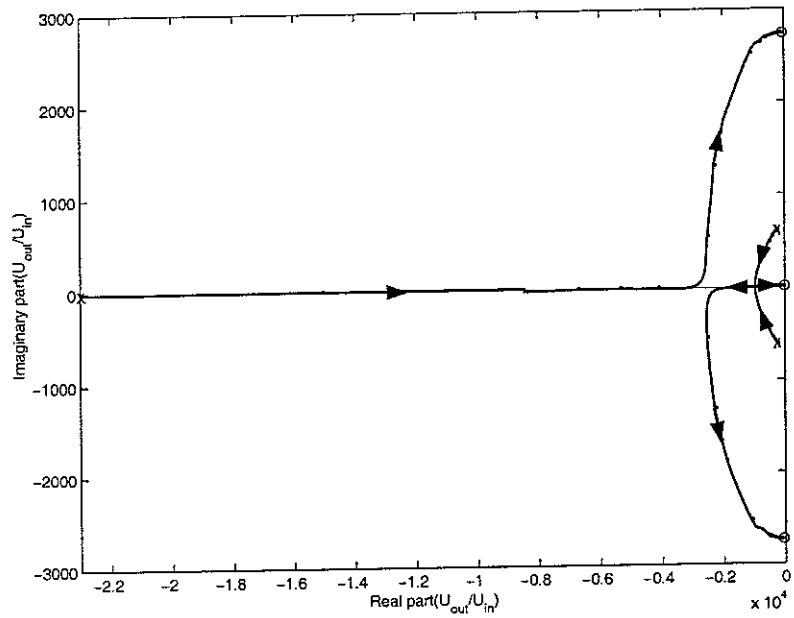

Figure 6.17: *Locus of the denominator roots of the closed loop FRF U_{out}/U_{in}, o open loop zeros, x open loop poles for a Wheatstone bridge*

For increasing values of $L_e=C_2R_3R_1$, i.e. R_3 if C_2 is constant and the coil resistance is balanced by R_1, the position of the open loop zeros changes in a characteristic way between the position for $L_e=0$ and L_e identical to the coil inductance or even larger and there is a value of L_e for which the closed loop changes from being unconditionally stable to becoming merely conditionally stable. This change of the zero position is not linear to the compensating inductance and Figure 6.18 shows the imaginary part of the zero i.e. its frequency position as function of the balancing inductance. The figure shows a large change in the zero frequency if the compensating inductance is very close to the coil inductance. Therefore balancing the inductance part of the Owens bridge is predicted to be difficult.

These simulations are only approximations to the real behaviour as the identification step in Section 3 has already shown that the model is very approximate at frequencies greater than 1kHz. They indicate that there is a practical limit to a perfect balance of the Owens bridge and realising induced voltage feedback that is comparable to velocity feedback. Similar root locus plots could be obtained by pole placement using an appropriate current feedback transfer function.

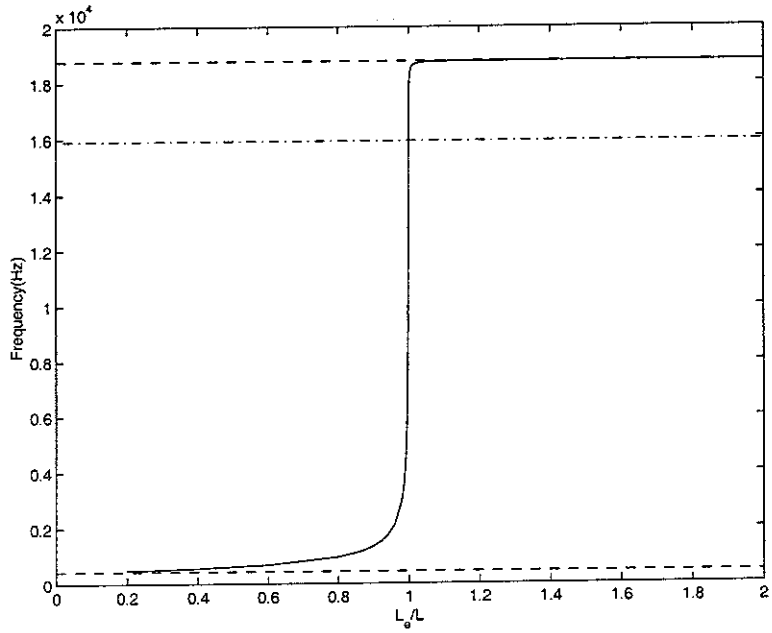

Figure 6.18: *Simulated position of the frequency of the additional zero due to the Owens bridge and relative inductance magnitude errors L/L_e. The balanced zero frequency is indicated by the dashed dotted line (-.-), the zero frequency position without compensation (--) and at the second natural frequency (---) by dotted lines.*

6.2 Implementation of induced voltage feedback control

Induced voltage feedback is implemented at the shaker using a Wheatstone and an Owens bridge respectively.

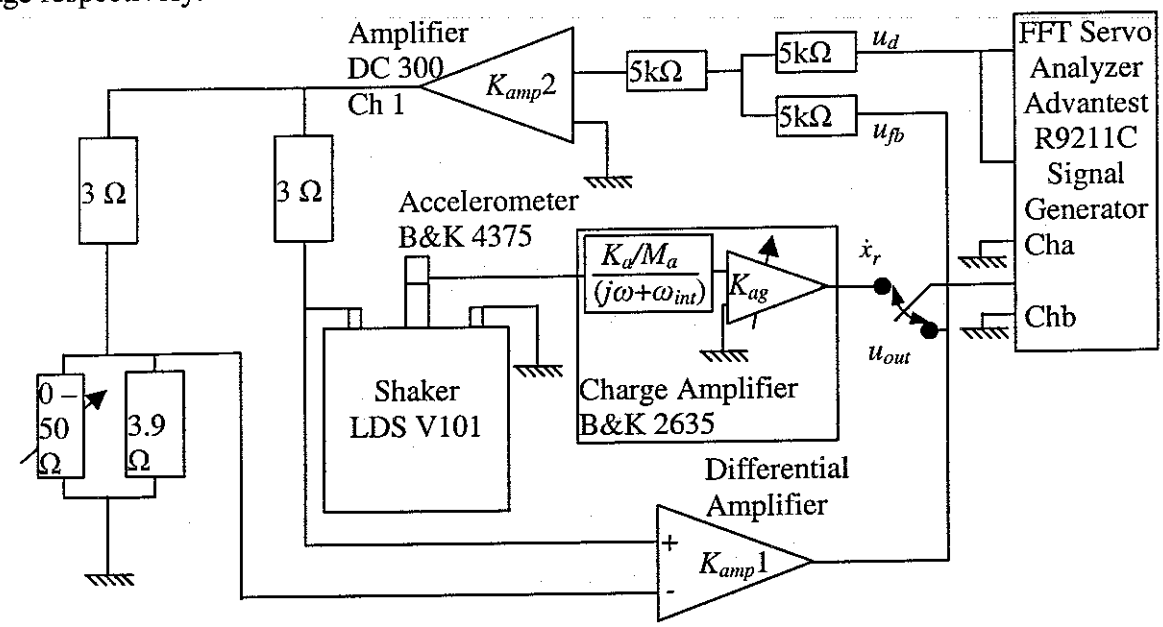

Figure 6.19: *Circuit for closed loop induced voltage feedback measurements using a Wheatstone bridge*

Figure 6.19 shows the used Wheatstone bridge implementation including the amplifiers, the shaker and the signal generator and analyser from Sections 4 and 5. An additional differential

amplifier with gain $K_{amp}1$ is used to implement the feedback gain G. 3 Ω power resistors with a tolerance of 10% are used for the resistance R_1. The balancing resistance R_{eb} is chosen to be a 3.9 Ω power resistor in parallel to a variable 50 Ω potentiometer so that the resistance value can be changed between 0 and 3.62 Ω. Since the 10% tolerance is large trials with different resistors have been carried out in order to obtain a well-balanced combination. Using potentiometers in parallel to R_1 has not given satisfactory results. For balancing purposes the potentiometer is varied in order to adjust R_{eb} to the internal coil resistance. The faint and solid line in Figure 6.11 is the result of an open loop measurement of the 10 times averaged FRF between the disturbance voltage U_d and the output voltage U_{out} with a balanced resistor that is found by visually maximizing the steepness of the anti-resonance of the FRF given by the servo analyser. After having determined this balanced state the feedback loop is closed by connecting the differential amplifier output to the feedback resistor of 5kΩ and the FRF between the disturbance voltage U_d and the measured velocity $\dot{X}_r$ is measured. Figure 6.20 depicts this FRF measured and simulated for a balanced Wheatstone bridge and different induced voltage feedback gains compared to the open loop. Measurements and simulations agree well in the interesting frequency range if model parameters are adjusted in order to account for non-ideal resistors (coil resistance: 3.66Ω, left side R_1=2.71Ω). In order to find the same frequency of the additional resonance the modelled coil inductance is adjusted to L=0.4847mH. Although measurement coherence is reduced due to the non-ideal differential amplifier, it is still sufficient to show the main characteristics in the considered frequency range. As in the proportional current feedback case an additional resonance peak at the open loop anti-resonance frequency between the characteristic electrical and the mechanical resonance frequency appears.

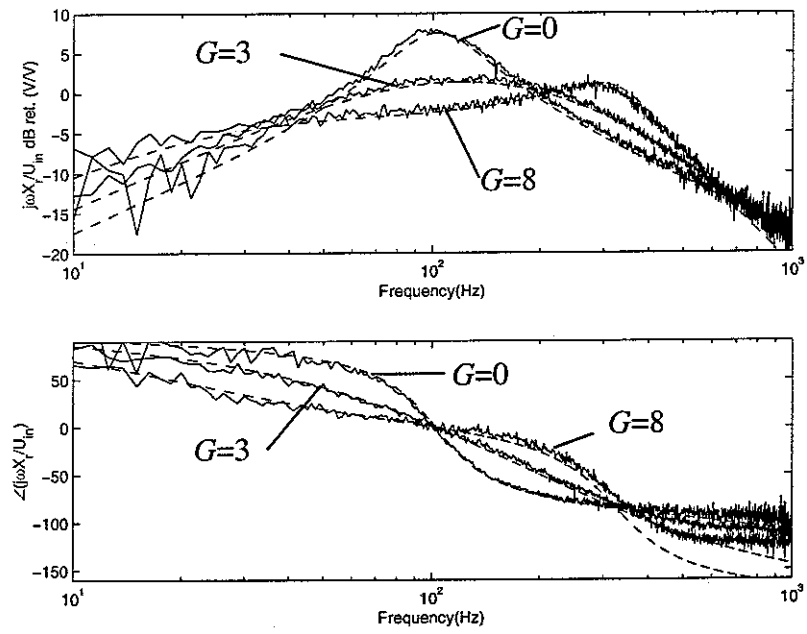

Figure 6.20: *Simulated (-- dashed line) and measured (- solid line) FRF between the disturbance voltage U_d and the measured coil velocity $\dot{X}_r$ for different output voltage feedback gains compared to the open loop, tuned resistance, L_e=0*

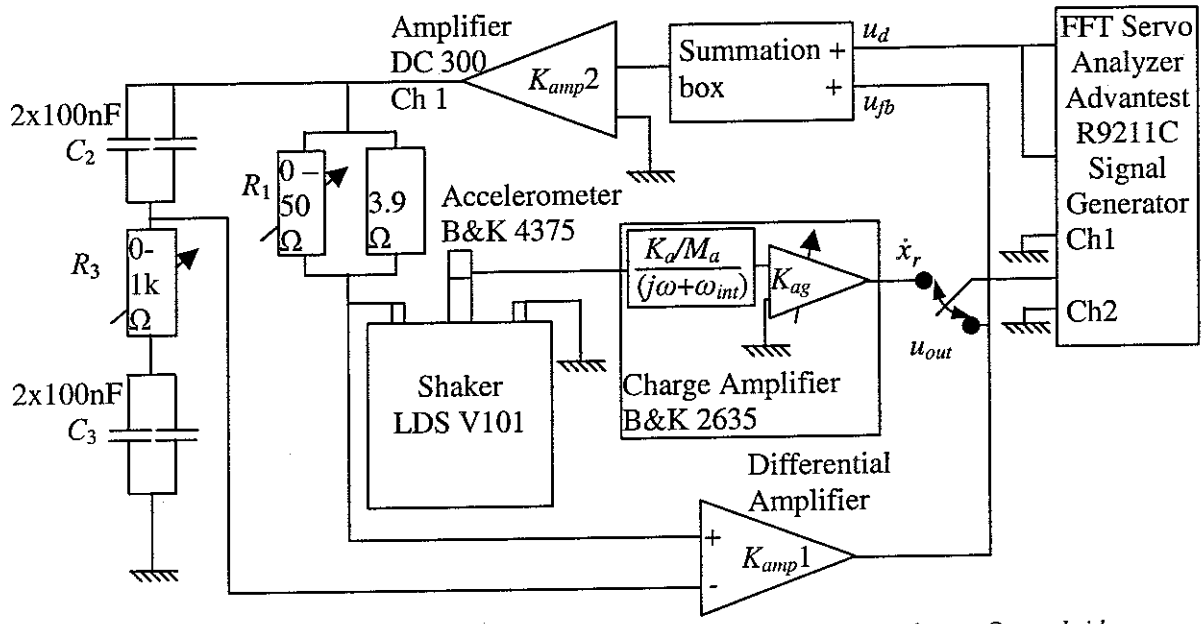

Figure 6.21: *Circuit for closed loop induced voltage feedback measurements using an Owens bridge*

The implementation scheme of the Owens bridge is shown in Figure 6.21 using twice two $100nF$ capacitors in parallel and a variable $1k\Omega$ resistor. First the resistor R_1 is tuned in the open loop in order to balance the coil resistance by $R=R_1C_2/C_3$ using the same method as for the Wheatstone bridge. Then the resistor R_3 is adjusted in order to change the apparent inductance $L_e=R_1R_3C_3$ at one side of the bridge and to compensate for the coil inductance. Figure 6.22 shows the FRF from the disturbance voltage U_d to the output voltage U_{out} when R_1 is tuned to maximize the steepness of the anti-resonance. Remark that the frequency of the notch is slightly different from the one determined in Figure 6.11. due to parameter variability. Then R_3 is changed from its minimum value of 37Ω to 370Ω and 475Ω so that the notch is tuned to 400Hz, 600Hz and 800 Hz respectively. As the notch gets blurred and the coherence reduced for increasing notch frequency 800 Hz is about the highest frequency to which the notch can be clearly tuned manually. For higher values of R_3 the FRF approaches a

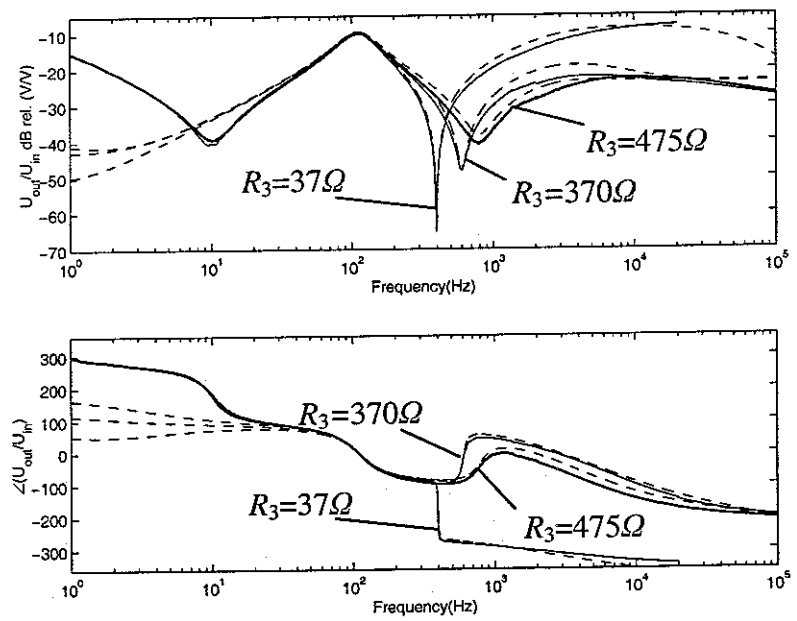

Figure 6.22: *Bode plot of the measured (solid line -) and simulated (dashed line --) FRF between the bridge input voltage U_{in} and the bridge output voltage U_{out} for three different values of R_3 and C_3 capacitance changes within tolerance (+/-10%) when R_1 is tuned to give a maximally steep anti-resonance at 400 Hz*

misbalanced state similar to the one depicted as a dashed line in Figure 6.11. By assuming capacitor tolerance given by the manufacturer to 10% simulations can be fitted to measurements as shown in Figure 6.22. As a shaker with a different coil assembly has been used corresponding parameter values are compiled in Table 6.1. Especially the eddy current behaviour has changed drastically probably because a different sheet metal has been used within the magnetic circuit. It is remarkable that even small parameter differences within manufacturing tolerances between C_2 and C_3 as compiled in Table 6.2 prevent a perfect bridge balance. Simulations show that these differences are responsible for the additional amplitude and phase changes at the zero frequency indicating increased damping of the notch when changed to higher frequencies.

Table 6.1: *Identified parameters of the shaker with different coil assembly*

Parameter		Value
Coil assembly mass	M	0.0014 kg
Duct cover stiffness	K	980 N/m
Damping coefficient	D	0.31 Ns/m
Inductance	L	0.375 mH
Resistance	R	3.48 Ohms
Actuator constant	Ψ	2.1 N/A or V/m/s
Resistance due to eddy currents	R_e	40 Ohms
Line inductance	L_2	$2.62\ 10^{-10}$ H
Capacitance	C	$2.5\ 10^{-8}$Fa
Line inductance	L_1	$1.179\ 10^{-5}$ H

The difference between measurements and simulations at even higher frequencies is likely due to the not in detail modelled influence of the magnetic core as explained for instance in [89]. Hence eddy currents, self-capacitance and residual looses of the core are to be compensated if the bandwidth is to be increased to even higher frequencies. For instance due to the current in the coil a high frequency magnetic field is generated that induces eddy currents opposing the primary current in other coil windings. The additional, apparent coil resistance for higher frequencies is modelled by a simple resistance R_e as explained in Appendix B although more sophisticated models as for instance presented in [90] might be necessary to improve the already satisfactory fit. The low frequency fit between measurements and simulations could be improved by considering power amplifier dynamics and especially an additional capacitance in parallel.

Table 6.2: *Identified capacitor values*

Parameter		Value
Capacitor	C_2	$1.85\ 10^{-7}$ Fa
Capacitor (notch tuned to 400 Hz)	C_3	$1.8\ 10^{-7}$ Fa
Capacitor (notch tuned to 600 Hz)	C_3	$1.84\ 10^{-7}$ Fa
Capacitor (notch tuned to 800 Hz)	C_3	$1.89\ 10^{-7}$ Fa

Figure 6.23 depicts the Nyquist plot of the open loop FRF between the disturbance voltage U_d and the bridge output voltage U_{out} for the notch tuned to 400 Hz and 800 Hz. As predicted in Section 6.1 the closed loop FRF turns from unconditionally stable to conditionally stable when the zero is moved to higher frequencies. This is obvious in Figure 6.23 where the locus of the open loop FRF moves into the left half plane also for higher frequencies when the compensating inductance value is changed to a higher value. Measurements already cross slightly into the left half plane for lower frequencies (first, left notch in Figure 6.22) at both inductance values because of power amplifier dynamics.

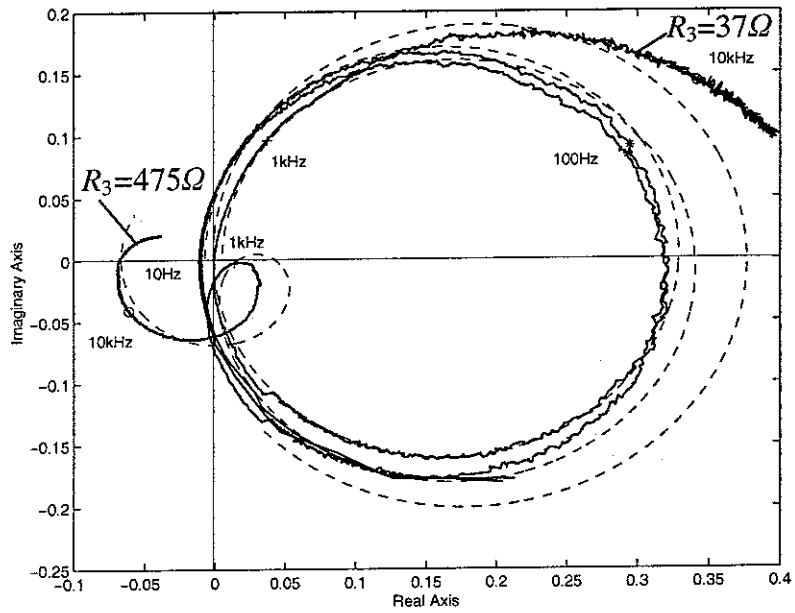

Figure 6.23: *Nyquist plot of the measured (solid line -) and simulated (dashed line --) FRF between the bridge input voltage U_{in} and the bridge output voltage U_{out} for two different values of R_3 and C_3 capacitance changes within tolerance (+/-10%) when R_1 is tuned to give a maximally steep anti-resonance at 400 Hz*

Figures 6.24 – 6.26 depict closed loop measurements and simulations of the FRF between the disturbance voltage U_d and the measured coil velocity $\dot{X}_r$ for different values of the frequency of the open loop notch. Measurements and simulations agree well between about 20Hz and the notch frequency between 400Hz and 800 Hz. Vibration reductions between 12dB (400Hz notch frequency), 14dB (600Hz) and 16dB (800Hz) can be achieved over the frequency range until the notch frequency. At this anti-resonance frequency of the open loop a resonance peak appears in the closed loop that is only visible greatly damped as only gains close to the optimal one are depicted in Figures 6.24 to 6.26.

However, lower frequencies are dominated by influence of the power amplifier that is not modelled and that leads to an additional phase shift at low frequencies. Luckily the amplitude is small enough at the first, left-hand notch so that no instability occurs. Higher frequency measurements show a different dynamic relative to simulations due to unmodelled electromagnetic interaction, a different accelerometer behaviour and unmodelled shaker dynamics as for instance an additional, though in measurements not visible, resonance frequency is given by the supplier [84] at 12 kHz. In simulations in Section 6.1 an additional source of instability of the closed loop lies at the accelerometer natural frequency whereas in measurements a high amplitude peak potentially leading to instability appears at a frequency

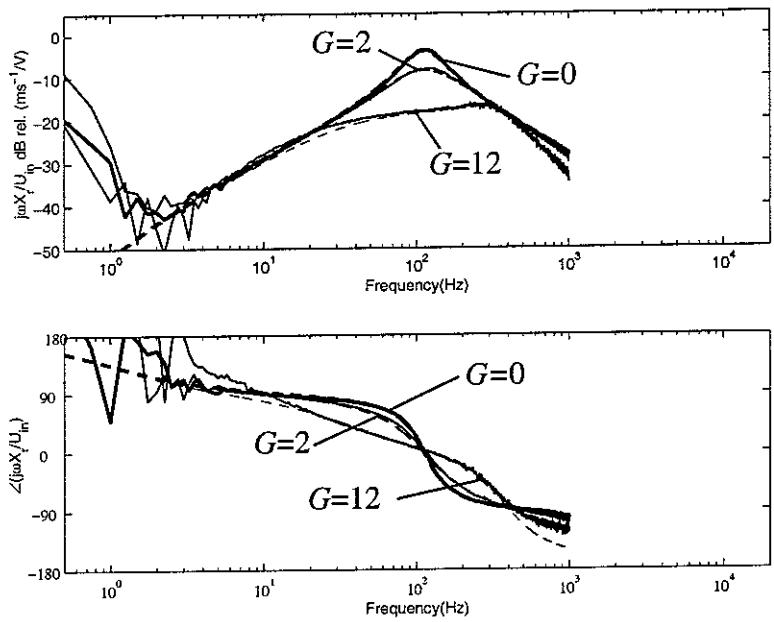

Figure 6.24: *Bode plot of the closed loop measured (solid line -) and simulated (dashed line --) FRF between the disturbance voltage U_d and the measured coil velocity $\dot{X}_r$ with different feedback gains G=2, 12 compared to the open loop case for R_3=37 and the open loop anti-resonance at 400 Hz when R_1 is tuned to give a maximally steep anti-resonance at 400 Hz*

between the frequency of the open loop anti-resonance that depends on the inductance tuning and higher electromagnetic or mechanical dynamics. In order to increase the bandwidth of self-sensing control hence these high order dynamics are to be compensated for. Alternatively a low-pass filter with a cut-off frequency beyond the open loop notch frequency could be tried in order to achieve a minor increase in bandwidth. Finally further investigations could be based on a system where electromagnetic interaction and higher mechanical dynamics are minimized.

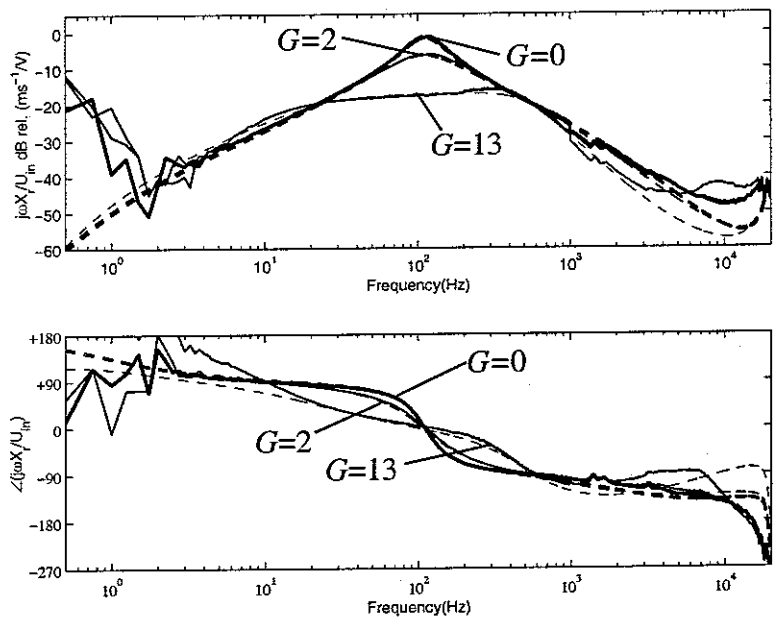

Figure 6.25: *Bode plot of the closed loop measured (solid line -) and simulated (dashed line --) FRF between the disturbance voltage U_d and the measured coil velocity $\dot{X}_r$ with different feedback gains G=2, 13 compared to the open loop case for R_3=37 and the open loop anti-resonance at 600 Hz when R_1 is tuned to give a maximally steep anti-resonance at 400 Hz*

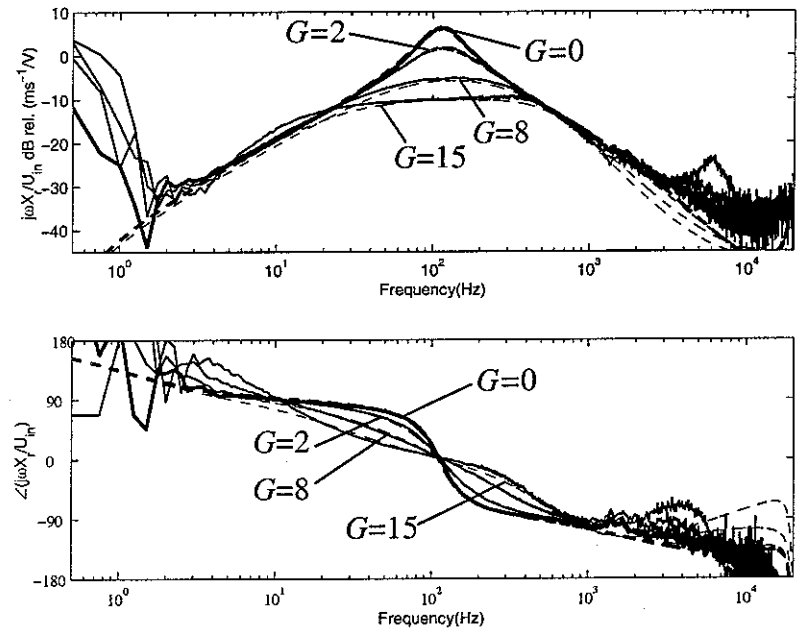

Figure 6.26: *Bode plot of the closed loop measured (solid line -) and simulated (dashed line --) FRF between the disturbance voltage U_d and the measured coil velocity $\dot{X}_r$ with different feedback gains G= 2, 8, 15 compared to the open loop case for R_3=37 and the open loop anti-resonance at 800 Hz when R_1 is tuned to give a maximally steep anti-resonance at 400 Hz*

7. CONCLUDING REMARKS

In order to investigate the limits of use of an electrodynamic actuator as a self-sensing vibration reduction device a conventional shaker has been modelled, identified and direct velocity, proportional current feedback and induced voltage feedback have been simulated and implemented experimentally.

Modelling of the mechanical, electrical, coupling and accelerometer system by LTI models has shown that the electromagnetic transducer coefficient has to be as big as possible for a self-sensing actuator. Additional passive damping is added to the mechanical system by the back-EMF and Lorentz force coupling with the electrical system already leading to "vibration reduction" of about 22dB for force excitation. Vibration reduction increases with decreasing electrical impedance. The effect of the mechanical system on the electrical system is also clearly visible by an additional motional impedance.

Identification by comparing the model to a FRF estimated from the power spectrum densities of input and output signals at the shaker and adjusting parameters leads to a good correspondence between measurements and simulations below and at the first mechanical frequency of the shaker. The electrical FRF shows good correspondence also at higher frequencies if an Eddy current and a capacitance model are added which however have little effects on the measurement of the mechanical FRF.

Using the rootlocus method and the Nyquist criterion, measured velocity feedback is found to become unstable only for very high gains in theory due to additional accelerometer dynamics. Simulations predict additional damping at the shaker mechanical natural frequency and a vibration reduction of up to 35 dB for negative velocity feedback. Positive velocity feedback reduces damping and becomes unstable already for small gains. Implementation of negative velocity feedback at the shaker shows a maximum reduction of only about 27 dB as for high gains unmodelled shaker dynamics lead to a peak at about 2500 Hz and a very low-frequency vibration probably due to integrator electronics is perceived.

Theoretical investigations show that current feedback is proportional to velocity feedback below an internal actuator cut-off frequency. Additionally the feedback gain has to be traded off for the control bandwidth. Applying the Nyquist criterion reveals that proportional current feedback is stable for positive gains smaller than the electrical resistance. Closed loop simulations indicate that additional vibration reduction of up to 8 dB is possible by adding damping at the first mechanical natural frequency for positive current feedback, but that negative proportional current feedback does not lead to vibration reduction. The root locus plot of the closed loop FRF explains the additional damping by an interaction of the mechanical poles with the electrical pole of the shaker. It highlights that the shaker acts as an analogue lead compensator. Moreover, for the choice of the value of the electrical shaker resistance, closed loop simulations and the root locus plot indicate that control robustness and self-sensing effectiveness have to be traded off. For a preliminary experimental investigation, an external primary force is not applied so that the vibration reduction cannot be found. But comparing other simulated FRFs to measurements shows good correspondence for frequencies smaller than 1000Hz.

Simulations of induced voltage feedback show that vibration reduction up to 30 dB at force excitation is possible if the coil resistance and inductance are completely compensated by an external Owens bridge. However, if ideal compensation is not possible, a stability limit appears at a frequency depending on the amount of compensation. If only the coil resistance is compensated simulations show that induced voltage feedback is unconditionally stable, but vibration reduction only up to 8 dB comparable to the proportional current feedback case is possible. This reduction is also found in experiments for feedback at a Wheatstone bridge when measuring the FRF from the disturbance voltage to the coil velocity. At the practical implementation of the Owens bridge a tuning problem is observed as the coil inductance could not be compensated completely. When partly compensating for the inductance vibration reduction up to 16 dB is observed and control bandwidth is increased up to about 800Hz. At greater frequencies the simulations match the measurements only qualitatively.

Further work could first focus on optimising the actuator for self-sensing. Especially the found trade-offs amplitude-bandwidth and robustness-sensing have to be chosen adequately for the application. A second requirement is to reduce eddy currents at higher frequencies and to respect weight constraints despite a large transducer coefficient.

Second in order to balance the bridge parameters an adaptive mechanism, similar to the one used by [37] for piezoelectric sensoriactuators, could be used that also has to prevent that these parameters surpass a certain value that leads to instability. The compensation side of the bridge could also be realized with electronics in a similar way, but less complicated than carried out by [81] (analogue circuit) and [48] (digital-analogue).

Third in order to investigate the influence of a self-sensing actuator on a flexible mechanical system a beam or plate should be added to the shaker and several mechanical FRFs should be measured and compared to simulations. Especially the question of how far collocation of a self-sensing actuator holds for a flexible system should be investigated. Finally the use of a self-sensing actuator as an inertial actuator could be examined at the same system.

8. REFERENCES

[1] Matsumura, F. Okada, Y. Fujita, M. and Namerikawa, T. State of the Art of Magnetic Bearings. JSME International Journal Series C. Vol. 40. No.4. 1997. pp.553-560

[2] von Flotow, A.H. An Expository Overview of Active Control of Machinery Mounts. Proceedings of the 27th Conference on Decision and Control. Austin. Tx. December 1988. pp. 2029-2033

[3] Karnopp, D. Active and Semi-Active Vibration Isolation. Transactions of the ASME. Special 50th Anniversary Design Issue. June 1995. Vol.117. pp. 177-185

[4] Preumont, Andre. Vibration Control of Active Structures. Kluver Academic Publishers. 2nd Edition. 2002

[5] Gardonio, P. Lee. Y.-S. Elliott, S.J. and Debost, S. Analysis and measurement of a matched volume velocity sensor and uniform force actuator for active structural acoustic control. Journal of the Acoustical Society of America. Vol. 100. No. 6. December 2001. pp. 3025-3031

[6] Baumann, W.T. Saunders, W.R. and Robertshaw, H.H. Active suppression of acoustic radiation from impulsively excited structures. Journal of the Acoustical Society of America. Vol. 90. No.6. December 1991. pp. 3202-3208

[7] Heckl, M. and Müller, H.A. Taschenbuch der Technischen Akustik. Springer. Berlin. 2nd Edition. 1995

[8] Harris, C.M. Shock and Vibration Handbook. McGraw-Hill. New York. 4th Edition. 1995

[9] Brennan, M.J. and Dayou, J. Global Control of Vibration Using a Tunable Vibration Neutralizer. Journal of Sound and Vibration. Vol. 232. No. 3. 2000. pp. 585-600

[10] Elliott, S.J. Serrand, M. and Gardonio, P. Feedback Stability Limits for Active Isolation Systems with Reactive and Inertial Actuators. Transactions of the ASME. Journal of Vibration and Acoustics. Vol. 123. April 2001. pp. 250-261

[11] Beard, A.M. von Flotow, A.H and Schubert, D.W. A practical product implementation of an active/passive vibration isolation system. Proceedings of Stable Control of Active Isolation Systems. 2000. pp. 101-108
[12] Gardonio, P. Bianchi, E. and Elliott, S.J. Smart Panel with Multiple Decentralised Units for the Control of Sound Transmission. Journal of Sound and Vibration. in press. 2003
[13] Fuller, C.R. Elliott, S.J. and Nelson P.A. Active Control of Vibration. Academic Press. London. 1996
[14] Nelson, P.A. Elliott, S.J. Active Control of Sound. Academic Press. London. Fourth printing. 1999
[15] Roure, A. Self-adaptive Broadband Active Sound Control System. Journal of Sound and Vibration. 1985. Vol.101. No.3. pp. 429-441
[16] Rafaely, B. and Jones, M. Combined feedback-feedforward active noise-reducing headset-The effect of the acoustics on broadband performance. Vol. 112. No.3. Pt.1. September 2002. pp. 981-989
[17] Elliott, S.J. Nelson, P.A. Stothers, I.M. and Boucher, C. C. In-flight Experiments on the Active Control of Propeller-induced Cabin Noise. Journal of Sound and Vibration. Vol. 140. No.2. 1990. pp. 219-238.
[18] Elliott, S. J. Signal Processing for Active Control. Academic Press. 2001
[19] Petitjean, B. and Legrain, I. Feedback Controllers for Active Vibration Suppression. Journal of Structural Control. Vol.3. No. 1-2. June 1996. pp. 111-127.
[20] Johnson, M.E. and Elliott, S.J. Active control of sound radiation using volume velocity cancellation. Journal of the Acoustical Society of America. Vol. 98. No.4. October 1995. pp. 2174-2186.
[21] Henrioulle, K. and Sas, P. Experimental validation of a collocated PVDF volume velocity sensor/actuator pair. Journal of Sound and Vibration. Vol. 265. 2003. pp. 489-506.
[22] Elliott, S.J. Gardonio, P. Sors, T.C. and Brennan, M.J. Active vibroacoustic control with multiple local feedback loops. Journal of the Acoustical Society of America. Vol.111. No.2. February 2002. pp.908-915
[23] Balas, M. J. Direct Velocity Feedback Control of Large Space Structures. AIAA Journal of Guidance and Control. Vol. 2. May-June 1979. pp. 252-253
[24] Sun, J.Q. Some Observations on Physical Duality and Colocation of Structural Control Sensors and Actuators. Journal of Sound and Vibration. Vol. 194. No. 5. 1996. pp. 765-770.
[25] Hunt, F.V. Electroacoustics. Transduction and Its Historical Background. Harvard University Press. 1954
[26] Pratt, J. and Flatau, A.B. Development and Analysis of a Self-sensing Magnetostrictive Actuator Design. SPIE/ASME/SEM North American Conference on Smart Structures 2/93
[27] Clephas, B. and Janocha, H. Extended Performance of Hybrid Actuators. 4th European Conference on Smart Materials and Structures. Internet Publication.
[28] Dosch, J.J. Inman D.J. and Garcia, E. A Self-Sensing Piezoelectric Actuator for Collocated Control. J. of Intell. Mater. Syst. And Struct. Vol.3. January 1992
[29] Montie, D. and Maslen, E. Experimental Self-Sensing Results for a Magnetic Bearing. Proceedings of ASME TURBOEXPO. 4-7 June. 2001
[30] Kettle, P. Murray, A. and Mynihan, F. Sensorless Control of a Brushless DC motor using an Extended Kalman estimator. PCIM'98. Intelligent Motion. May 1998. pp.385-392
[31] Hagood, N.W. and von Flotow, A. Damping of Structural Vibrations with Piezoelectric Materials and Passive Electrical Networks. Journal of Sound and Vibration. Vol.146. No.2. 1991. pp.243-268
[32] Hagood, N.W. and Crawley, E.F. Experimental Investigation of Passive Enhancement of Damping for Space Structures. Journal of Guidance, Control and Dynamics. Vol. 14. No.6. November-December 1991. pp. 1100-1109.
[33] Fleming, A.J. Behrens, S. and Moheimani, S.O.R. Synthetic impedance for implementation of piezoelectric shunt-damping circuits. Electronics Letters. Vol. 36. No. 18. August 2000. pp. 1525-1526
[34] Dosch, J.J. Inman, D.J. and Garcia, E. A Self-Sensing Piezoelectric Actuator for Collocated Control. J. of Intell. Mater. Syst. and Struct. Vol.3. January 1992. pp.166-185
[35] Anderson, E.H. and Hagood, N.W. Simultaneous Piezoelectric Sensing/Actuation: Analysis And Application To Controlled Structures. Journal of Sound and Vibration. Vol.174. No.5. 1994. pp.617-639
[36] Wang, K.W. Structural Vibration Suppression Via Parametric Control Actions – Piezoelectric Materials With Real-time Semi-Active Networks. Series on Stability, Vibration and Control of Structures Volume 1: Wave Motion, Intelligent Structures and Nonlinear Mechanics. World Scientific. Singapore. 1995. pp.112-134
[37] Cole, D.G. and Clark., R.L. Adaptive Compensation of Piezoelectric Sensoriactuators. Journal of Intelligent Material Systems And Structures. Vol.5. September 1994. pp.665-672
[38] Vippermann, J.S. and Clark, R.L. Implementation of an Adaptive Piezoelectric Sensoriactuator. AIAA Journal. Vol. 34. No. 10. October 1996. pp. 2102-2109
[39] Ma, K. Vibration control of smart structures with bonded PZT patches: novel adaptive filtering algorithm and hybrid control scheme. Smart Mater. Struct. Vol. 12. 2003. pp. 473-482
[40] Lee, Y.-S. Elliott, S.J. and Gardonio, P. Matched piezoelectric double sensor/actuator pairs for beam motion control. Smart Materials and Structures. Vol. 12. 2003. pp. 541-548

[41] Oshima, K. Takigami, T. and Hayakawa, Y. Robust Vibration Control of a Cantilever Beam Using Self-Sensing Actuator. JSME International Journal. Series C. Vol. 40. No. 4. 1997. pp. 681-687
[42] Forward, R.L. Electromechanical transducer-coupled mechanical structure with negative capacitance compensation circuit. U.S. Patent 4,158,787. June 19, 1979
[43] Wu, S.-Y. Broadband piezoelectric shunts for structural vibration control. U.S. Patent 6,075,309. June 13, 2000
[44] Behrens, S. Fleming, A.J. and Moheimani, S.O.R. A broadband controller for shunt piezoelectric damping of structural vibration. Smart Mater. Struct. Vol. 12. 2003. pp.18-28
[45] Riordan, R.H.S. Simulated inductors using differential amplifiers. Electronics Letters. Vol. 3. No. 2. February 1967. pp. 50-51
[46] Abramovitch, D. and Franklin, G. A Brief History of Disk Drive Control. IEEE Control Systems Magazine. June 2002
[47] Paulitsch, C. Okamoto, K.-I. and Utsunomiya, K. Self-sensing Active Damping Guide Roller for Elevators. VDI-Berichte 1753. VDI. Düsseldorf 2003. pp.91-110
[48] Behrens, S. Fleming, A.J and Moheimani, S.O.R Electrodynamic Vibration Suppression. SPIE Smart Structures and Materials. Damping and Isolation. San Diego. 2-6 March 2003
[49] Hanson, B.M. Brown, M.D. and Fisher, J. Self Sensing: Closed-Loop Estimation for a Linear Electromagnetic Actuator. Proceedings of the American Control Conference. Arlington. VA. 25-27 June 2001
[50] Voigt, P.G.A.H. Improvements in or Relating to Thermionic Amplifying Circuits for Telephony. British Patent No. 231972 filed January 1924. issued April 1925
[51] de Boer, E. Theory of Motional Feedback. IRE Transactions on Audio. January-February 1961. pp.15-21
[52] Tanner, R.L. Improving Loudspeaker Response with Motional Feedback. Electronics. March 1951. pp.142 and 228-240
[53] Holdaway, H.W. Design of Velocity-Feedback Transducer Systems for Stable Low-Frequency Behavior. IEEE Transactions on Audio. September-October 1963. pp. 155-173
[54] Holdaway, H.W. Controlling the Upper-Frequency Characteristics of Velocity-Feedback Loudspeaker Systems. IEEE Transactions on Audio. September-October 1963. pp. 174-182
[55] de Boer, J. and Schenkel, G. Electromechanical Feedback. The Journal of the Acoustical Society of America. Vol. 20. No. 5. September 1948. pp.641-647
[56] Olson, H.F. Elements of Acoustical Engineering. D van Nostrand. NY. 2nd edition. 4th reprint. 1952
[57] Mills, P.G.L and Hawksford, M.O.J. Distortion Reduction in Moving-Coil Loudspeaker Systems Using Current-Drive Technology. J.Audio Eng. Soc. Vol. 37. No.3. March 1989
[58] Klaassen, J.A. and de Koning, S.H. Motional feedback with loudspeakers. Philips Technical Review Vol. 29. No. 5. 1968. pp. 148-157
[59] De Greef, D. and Vandewege, J. Acceleration feedback loudspeaker. Wireless World. September 1981
[60] Miller, J.M. Combining Positive and Negative Feedback. Electronics. March 1950
[61] Clements, W. A New Approach to Loudspeaker Damping. Audio Engineering. August 1951
[62] Ginzton, E.L. Balanced Feed-Back Amplifiers. Proceedings of the Institute of Radio Engineers. Vol. 26. No. 11. November 1938. pp. 1367-1379
[63] Mayer, H.F. Control of the Effective Internal Impedance of Amplifiers by Means of Feedback. Proceedings of the I.R.E. March 1939. pp.213-217
[64] Terman, F. E. Radio Engineers' Handbook. McGraw Hill. London. 1950
[65] Childs, U.J. Loudspeaker Damping with Dynamic Negative Feedback. Audio Engineering. February 1952
[66] Clements, W. It's Positive Feedback. Audio Engineering. May 1952
[67] Wentworth, J.P. Loudspeaker Damping by the Use of Inverse Feedback. Audio Engineering. December 1951
[68] Stahl, K.E. Synthesis of Loudspeaker Mechanical Parameters by Electrical Means: A New Method for Controlling Low-Frequency Loudspeaker Behavior. J. Audio Eng. Soc. Vol. 29. No. 9. September 1981. pp. 587-596
[69] Normandin, R. Extended Low-Frequency Performance of Existing Loudspeaker Systems. J. Audio Eng. Soc. Vol. 32. No. 1/2. January/February 1984. pp. 18-22
[70] Birt. D. Loudspeaker Power Amplifiers with Load-Adaptive Source Impedance. J. Audio Eng. Soc. Vol. 36. No. 7/8. July.August 1988. pp. 552-561
[71] Greiner R.A. and Travis M. Sims Jr. Loudspeaker Distortion Reduction. J. Audio Eng. Soc. Vol. 32. No. 12. December 1984. pp. 956-963
[72] Catrysse, J.A.M. On the Design of Some Feedback Circuits for Loudspeakers. J. Audio Eng. Soc. Vol. 33. No. 6. June 1985. pp. 430-435

[73] Werner, R.E. and Carrell, R.M. Application of Negative Impedance Amplifier to Loudspeaker Systems. Journal of the Audio Engineering Society. Vol. 6. No. 4. October 1958. pp. 240-243
[74] von Recklinghausen, D.R. Low-Frequency Range Extension of Loudspeakers. J. Audio Eng. Soc. Vol. 33. No. 6. June 1985. pp. 440-446
[75] Adams, G.J. Optimisation and Motional Feedback Techniques in Loudspeaker System Design. Ph.D. thesis. Department of Electrical Engineering. The University of Southampton. Dec. 1979
[76] Thiele, A.N. Loudspeakers in Vented Boxes: Part I. J. Audio Eng. Soc. Vol. 19. No. 5. May 1971. pp. 382-392
[77] Thiele, A.N. Loudspeakers in Vented Boxes: Part 2. J. Audio Eng. Soc. Vol. 19. No. 5. May 1971. pp. 471-483
[78] Benjamin, E. Audio Power Amplifiers for Loudspeaker Loads. J. Audio Eng. Soc. Vol. 42. No. 9. September 1994. pp. 670-683
[79] Self. D. Audio Power Amplifier Design Handbook. Newnes. Oxford. 2nd Edition. 2000
[80] Borwick, J. Loudspeaker and Headphone Handbook. Focal Press. Oxford. 2nd Edition. 1994
[81] Okada, Y. Matsuda, K. Hashitani, H. Self-sensing Active Vibration Control using the Moving-Coil-Type Actuator. Journal of Vibration and Acoustics. Vol. 117. October 1995. pp. 411-415
[82] Bai, M.R. and Wu, H. Robust Control of a sensorless bass-enhanced moving-coil loudspeaker system. J.Acoust.Soc.Am.Vol. 105. No. 6. June 1999. pp. 3283-3289
[83] Brüel&Kjær product data sheet accelerometers type 4375 and charge amplifier type 2635. Nærum. DK. www.bksv.com
[84] LDS product data sheet permanent magnet vibration testing systems V101. Royston. UK. www.lds.com
[85] Hammond, J. K. Signal Processing and Analysis. Lecture notes. Session 2002/03
[86] Unbehauen, H. Regelungstechnik I. Vieweg. Brunswick. 1987
[87] Rao S.S. Mechanical Vibrations. Addison-Wesley. Reading, Mass. Third Edition. 1986
[88] Neubert, H.K.P. Instrument Transducers, an introduction to their performance and design. Oxford University Press. 1963
[89] Snelling, E.C. Soft Ferrites Properties and Applications. Butterworths. London. 2nd Edition. 1988
[90] Miyashita, O. Ohniwa, K. Fujimaki, T. and Morikawa, M. Analysis of the Flux-Lag Effect in an Iron Core. Journal of the Japan Society of Applied Electromagnetics and Mechanics. Vol. 19. No. 5. 1995. pp. 875-878
[91] Horowitz, P. and Hill, W. The Art of Electronics. Cambridge University Press. 3rd Edition. 1980

Appendix A: Accelerometer response

In order to be able to implement collocated velocity feedback and to monitor its vibration an accelerometer is attached to the shaker. An accelerometer consists of a seismic mass on a piezoelectric material that generates an electric charge when strained. First its mechanical behaviour is modelled by a SDOF similar to the model described in Section 2. A resonant and a passive effect of the accelerometer sensor on the self-sensing actuator are described. Second the sensing function of the accelerometer is modelled by introducing a relative displacement between the two DOFs, by neglecting the electromechanical coupling due to the piezoelectric material and by approximating the signal processing of the charge amplifier. Then thirdly it is shown that a separate accelerometer sensor function can be determined. Finally the electrical FRF of the complete model is investigated indicating a minor influence of the accelerometer on the electrical circuit.

A.1 Resonant and passive effect of the accelerometer on the electrodynamic system

The coupled electrodynamic model is expanded by adding a SDOF accelerometer model to the model in Figure 2.2, as shown in Figure A.1.

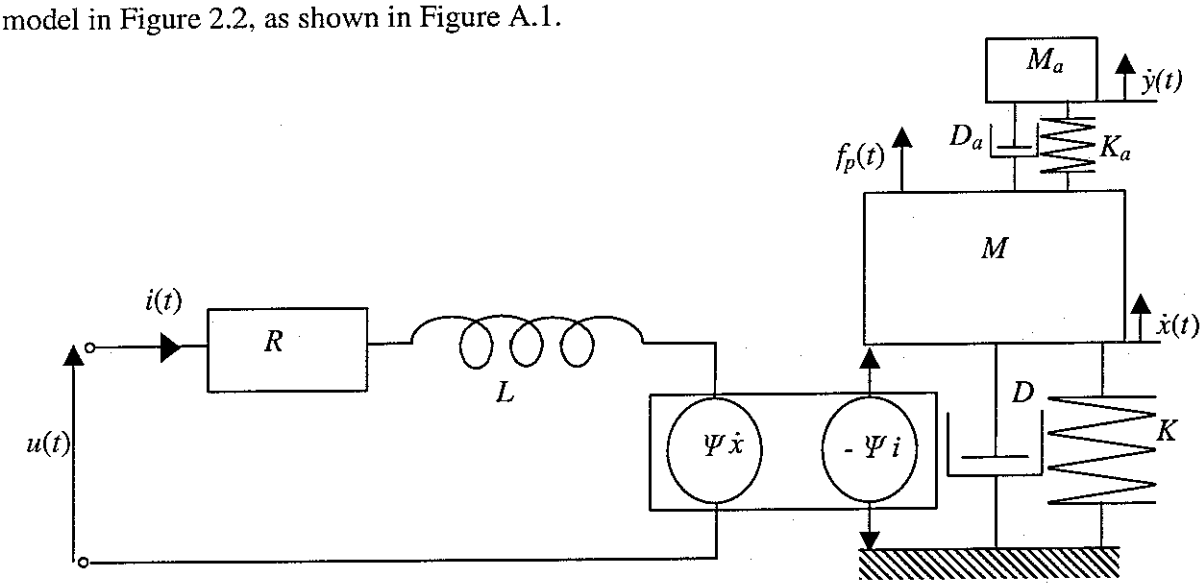

Figure A.1: *Fully coupled electrodynamic model with accelerometer*

The associated model equations become

$$\begin{bmatrix} M_a & -M_a & 0 \\ 0 & M & 0 \\ 0 & 0 & L \end{bmatrix}\begin{Bmatrix} \ddot{z} \\ \ddot{x} \\ \dot{i} \end{Bmatrix}+\begin{bmatrix} D_a & 0 & 0 \\ D_a & D & -\Psi \\ 0 & \Psi & R \end{bmatrix}\begin{Bmatrix} \dot{z} \\ \dot{x} \\ i \end{Bmatrix}+\begin{bmatrix} K_a & 0 & 0 \\ K_a & K & 0 \\ 0 & 0 & 0 \end{bmatrix}\begin{Bmatrix} z \\ x \\ q \end{Bmatrix}=\begin{Bmatrix} 0 \\ f_p \\ u \end{Bmatrix} \tag{A.1}$$

when introducing a relative displacement $z = y - x$ between the displacement of the seismic mass of the accelerometer y and the coil displacement x. The coupled mechanical FRF from the external primary force input to the velocity of the coil assembly then is

$$\frac{\dot{X}(\omega)}{F_p(\omega)} = \frac{1/(Z_m + Z_t)}{1 + \left(\Psi^2/Z_e - Z_t^2/Z_a\right)\frac{1}{(Z_m + Z_t)}} = \frac{Z_a Z_e}{\left(Z_e(Z_m + Z_t) + \Psi^2\right) Z_a - Z_t^2 Z_e} \qquad \text{(A.2)}$$

where the feedback component now consists of a term due to the electrodynamic coupling Ψ^2/Z_e explained in section 2 and a term from the mechanical coupling $(Z_t^2)/Z_a$ with the accelerometer where $Z_a=j\omega M_a+K_a/j\omega+D_a$ is the mechanical impedance of the accelerometer. The mechanical coil impedance Z_m is increased by the impedance $Z_t=K_a/j\omega+D_a$ defined by the transferred force F_t on the accelerometer and the relative velocity between the accelerometer and the coil $\dot{z}$.

The appearance of an additional resonance frequency in the Bode plots of the coupled and uncoupled FRF $\dot{X}/F_p$ depicted in Figures A.2 is the resonant effect of an additional SDOF system added to a mechanical system. This effect could be used for vibration reduction at the anti-resonance frequency by appropriately choosing the natural frequency of the additional DOF.

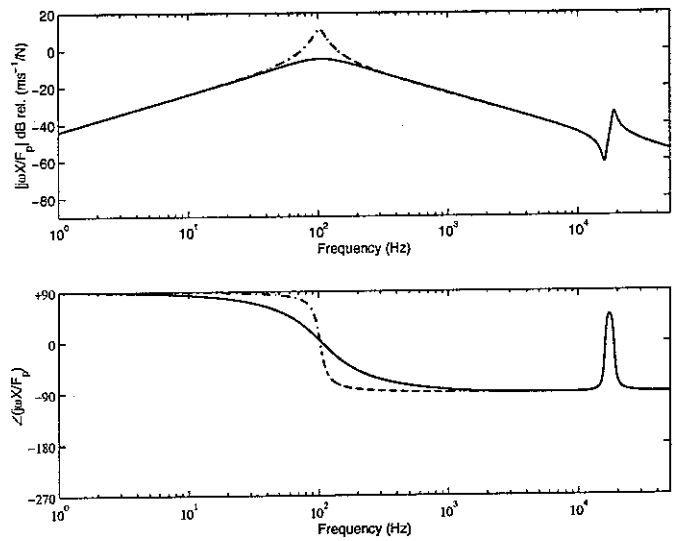

Figure A.2 : *Simulated Bode plot of the FRF from the external force to the velocity for the coupled electromechanical model with accelerometer in figure A.1(solid line) compared to the FRF of the mechanical model with accelerometer (dash dotted line) and w/o coupling*

Moreover the electromagnetic coupling is not able to greatly influence the second mechanical frequency that lies beyond the electrical frequency in simulations of equation (A.2) with additional parameters compiled in Table A.1. Also when changing parameters, so that the first mechanical resonance frequency lies beyond the electrical frequency, using the electrodynamic actuator does not add visible damping to the mechanical system at this mechanical, resonance frequency. Likewise, when reducing the second mechanical resonance frequency to lie below the electrical frequency the electrodynamic coupling is efficient by adding damping at this frequency. Hence, the mechanical frequency of the SDOF system or an attached DOF has to lie below the electrical frequency if the self-sensing actuator is to provide sufficient damping.

Table A.1: *Parameters for accelerometer simulations*

Parameter		Value
Stiffness of inertial mass support	K_a	6.7 10^6 N/m
Damping of accelerometer	D_a	4 Ns/m
Inertial mass of accelerometer	M_a	0.00067 kg
Undamped resonance frequency	ω_{na}	15915.45 Hz
Damped resonance frequency	ω_{da}	15908 Hz

The Nyquist plot in Figure A.3 of the same FRFs gives information about the value of the mechanical frequencies. Compared to the mechanical system without accelerometer the natural mechanical frequency is reduced from ca. 125.5 Hz to about 105.2 Hz with the electrodynamic coupling effect and from ca. 120.9 to about 102.4 Hz without the electrodynamic coupling effect. That is the passive effect of increasing the whole system mass and thus reducing the mechanical resonance frequency when adding an additional spring mass system to the mechanical system. Additionally the locus does not show spill over into the negative real half plane since the natural frequency of the accelerometer leads to a loop into the positive real half plane. This loop is virtually identical for both FRFs also indicating that the electrodynamic coupling effect is negligible for these frequencies.

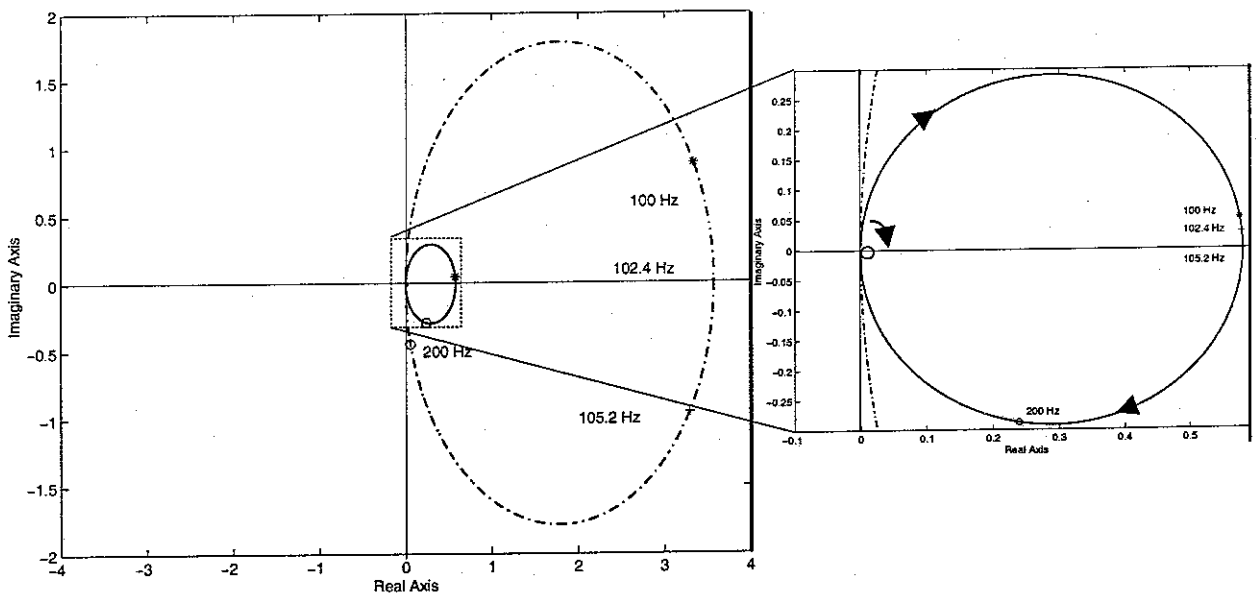

Figure A.3 : *Simulated Nyquist plot of the FRF from the force input to the velocity for the coupled electromechanical model with accelerometer in figure A.1 (solid line) compared to the FRF of the mechanical model with accelerometer (dash dotted line) and w/o coupling and zoom at the origin*

A.2 Relative displacement as measured system output

Although the expression 'accelerometer' indicates that an accelerometer measures the acceleration of the body to which it is attached $\ddot{x}$ in reality the accelerometer output charge is proportional to the relative displacement between both sides of the piezoelectric element $z = x\text{-}y$. In the real system a charge amplifier amplifies the signal coming from the accelerometer that is proportional to the relative displacement z and integrates it by an analogue circuit. The first effect is modelled by multiplying the relative displacement z by a gain K_s given by the accelerometer sensitivity. The second effect is included in the model by adding a non-ideal integrator i.e. a low pass filter with ω_{int} = 1 Hz = 2π rad/s cut-off frequency. Hence, when assuming harmonic behaviour of the form $\dot{x}_r(t) = \mathrm{Re}(\dot{X}_r(\omega)\exp(j\omega t))$ the output becomes the integrated relative displacement

$$\dot{X}_r = \frac{K_s}{j\omega + \omega_{int}} Z = \frac{K_s}{j\omega + \omega_{int}} (X - Y). \tag{A.3}$$

Then the FRF of equation (A.2) from the primary input F_p to the integrated relative displacement $\dot{X}_r$ is

$$\frac{\dot{X}_r(\omega)}{F_p(\omega)} = \frac{M_a K_s/(Z_a Z_m)}{\left(1 + \left(Z_t j\omega + \Psi^2 Z_a/(M_a Z_e)\right) M_a/(Z_a Z_m)\right)(j\omega + \omega_{int})} . \tag{A.4}$$

As before two feedback terms for the electrodynamic coupling $\Psi^2 Z_a/(M_a Z_e)$ and the mechanical coupling $Z_t j\omega$ appear. The Bode plot of this FRF shows a similar behaviour as a FRF from a force input at one DOF to the absolute velocity of a second, non-collocated DOF i.e. no anti-resonance is observed and in contrast to Figure A.2 there is a 180 degree phase shift associated to each mechanical, natural frequency. As in the case of the FRF to the absolute velocity $\dot{x}$ depicted in Figure A.2 the electrodynamic coupling is only sufficiently efficient at frequencies inferior to the electrical frequency as the resonance frequency associated to the accelerometer is not visibly damped. In the Nyquist plot of the same FRF spill over in form of an additional smaller loop associated to the second mechanical frequency appears in the negative real half plane that is not visibly reduced by adding the self-sensing actuator. Additionally spill over appears at low frequencies due to the non-ideal integrator. This observation will become important when considering the control scheme in section 4 as a high gain might destabilize an integrated relative displacement feedback.

By comparing Figures A.2 to 2.8 and A.3 to 2.9 it is evident that for frequencies much lower than the resonance frequency of the accelerometer the integrated relative displacement is a very good approximation for the velocity of the mechanical system $\dot{x}$. That is a common result to be found for example in [87]. But it is also important to note that this approximation neglects a possible source of instability at the resonance frequency of the accelerometer, so that this approximation is not made during this study.

A.3 Accelerometer measurement function

Furthermore using an integrated relative displacement $\dot{x}_r$ is equivalent to considering the velocity of the coil assembly including the accelerometer case $\dot{x}$, if using an appropriate frequency dependent measurement function for the accelerometer. Rewriting the first row of equation (A.1) for the DOF z and considering time harmonic solutions of the form $z(t)=\mathrm{Re}\{Z(\omega)\exp(j\omega t)\}$ it follows

$$Z = -\frac{1}{-\omega^2 + 2j\xi_a\omega_{na}\omega + \omega_{na}^2}\ddot{X} \tag{A.5}$$

where $\omega_{na} = \sqrt{K_a/M_a}$ denotes the natural frequency of the accelerometer without damping and $\xi_a = D_a/(2\sqrt{K_a M_a})$. Equation (A.5) indicates that there is a 2nd order relation between the relative displacement z and the acceleration of the coil assembly that, as mentioned also by [87], can be approximated for frequencies much lower than the natural frequency of the accelerometer $\omega << \omega_{na}$ by

$$\ddot{x} \approx -\omega_{na}^2 z \tag{A.6}$$

When using equation (A.5) with equation (A.3) the exact accelerometer measurement function of the coil assembly velocity is found to be

$$\dot{X}_r = -\frac{K_{sen}}{j\omega + \omega_{int}}\frac{1}{-\omega^2 + 2j\xi_a\omega_{na}\omega + \omega_{na}^2}\ddot{X}, \tag{A.7}$$

where $K_{sen}=K_s\omega^2_{na}$. Thus the coil assembly acceleration $\ddot{x}$ as solution to the electromechanical system in equation (A.1) is the output of the electromechanical plant to be controlled and equation (A.7) describes the additional transducer FRF associated to the accelerometer and charge amplifier used in the following sections for the description of the accelerometer. $\dot{X}_r$ is then referred to as the measured velocity.

A.4 Electrical FRF with accelerometer

The FRF from the source voltage to the coil current when adding an accelerometer to the coupled electromechanical system as depicted in Figure A.1 is

$$\frac{I(\omega)}{U(\omega)} = \frac{Z_m Z_a - Z_t jM_a\omega}{Z_e(Z_m Z_a + Z_t jM_a\omega) + \Psi^2 Z_a}. \tag{A.8}$$

Comparing the bode plots in Figure A.4 of this FRF and the case without accelerometer depicted in Figure 2.10 indicates that in contrast to the influence of the first natural frequency the influence of the second natural frequency is so small that it is not visible in Figure A.4.

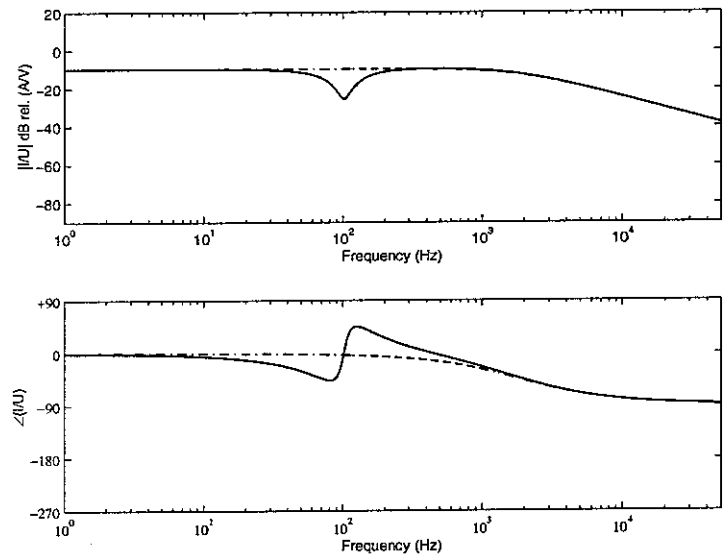

Figure A.4 : *Simulated Bode plot of the FRF from the source voltage to the current for the coupled electromechanical model with accelerometer in figure A.1 (solid line) compared with the FRF of the electrical model with accelerometer(dash dotted line) and w/o coupling*

Nevertheless the effect of the additional accelerometer mass is visible in the Nyquist plot in Figure A.5 as the resonance frequency decreases to about 102.5 Hz from the 120.9 Hz of the FRF depicted in Figure 2.10. But as in the Bode plot the expected second natural frequency is not visible because it lies at frequencies much greater than the electrical frequency where the self-inductance effect of the coil leads to a low-pass filter behaviour.

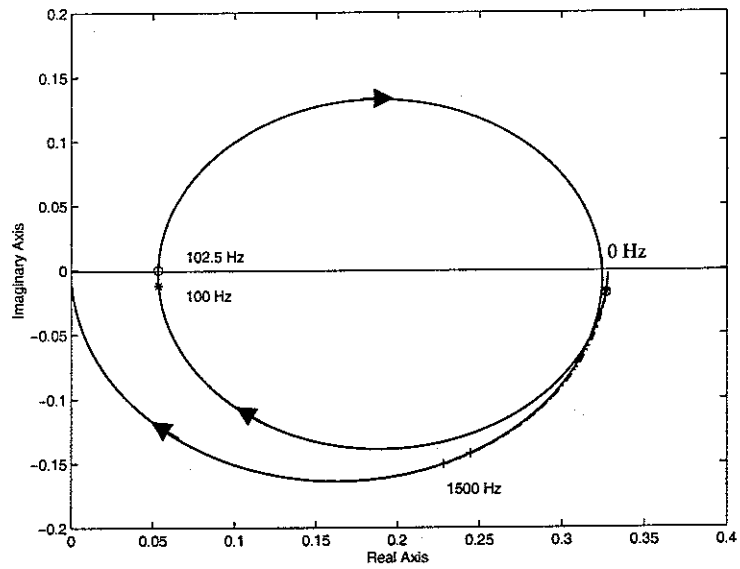

Figure A.5 : *Simulated Nyquist plot of the FRF between the source voltage and the current for the coupled electromechanical model with accelerometer in figure A.1 (solid line) compared to the FRF of the electrical model with accelerometer(dash dotted line) w/o coupling*

Appendix B: Higher frequency effects at identified electrical FRF

In Appendix A it has been noted that the natural frequencies of the mechanical system to be damped have to lie below the electrical, characteristic frequency if no compensation is used. Therefore a detailed model for higher frequencies is necessary if compensation is aimed. One explanation for the high frequency behaviour could be eddy currents induced in the ferromagnetic core that can be modelled following for instance [88] by adding a resistance R_e and a very small inductance L_2 parallel to the coil inductance L and resistance R. However, L_2 is chosen so small that it does not show any influence on the simulations in the considered frequency range and is only needed to allow convenient simulations with Matlab™ state space models.

The resulting model with equations

$$\begin{bmatrix} M_a & 0 & 0 & 0 \\ 0 & M & 0 & 0 \\ 0 & 0 & L & -L \\ 0 & 0 & -L & L_2+L \end{bmatrix} \begin{Bmatrix} \ddot{y} \\ \ddot{x} \\ \dot{i} \\ \dot{i}_2 \end{Bmatrix} + \begin{bmatrix} D_a & -D_a & 0 & 0 \\ -D_a & D+D_a & -\Psi & 0 \\ 0 & \Psi & R & 0 \\ 0 & 0 & 0 & R_e \end{bmatrix} \begin{Bmatrix} \dot{y} \\ \dot{x} \\ i \\ i_2 \end{Bmatrix} + \begin{bmatrix} K_a & -K_a & 0 & 0 \\ -K_a & K+K_a & 0 & 0 \\ 0 & 0 & 0 & 0 \\ 0 & 0 & 0 & 0 \end{bmatrix} \begin{Bmatrix} y \\ x \\ q \\ q_2 \end{Bmatrix} = \begin{Bmatrix} 0 \\ f_p \\ u_d \\ 0 \end{Bmatrix} \tag{B.1}$$

is shown in Figure B.1. Resulting simulations using

$$\frac{I(\omega)}{U_d(\omega)} = \frac{Z_{e2}\left(-Z_m Z_a \omega^2 - Z_t j M_a^2 \omega\right)}{\left(Z_e Z_{e2} + L^2\omega^2\right)\left(-Z_m \omega^2 Z_a - Z_t M_a^2\right) - \Psi^2 \omega^2 Z_{e2} Z_a} \tag{B.2}$$

where $Z_{e2} = (L_2+L)j\omega + R_e$ is an additional equivalent electric impedance with parameters in Table B.1 are shown in Figures B.2 and B.3.

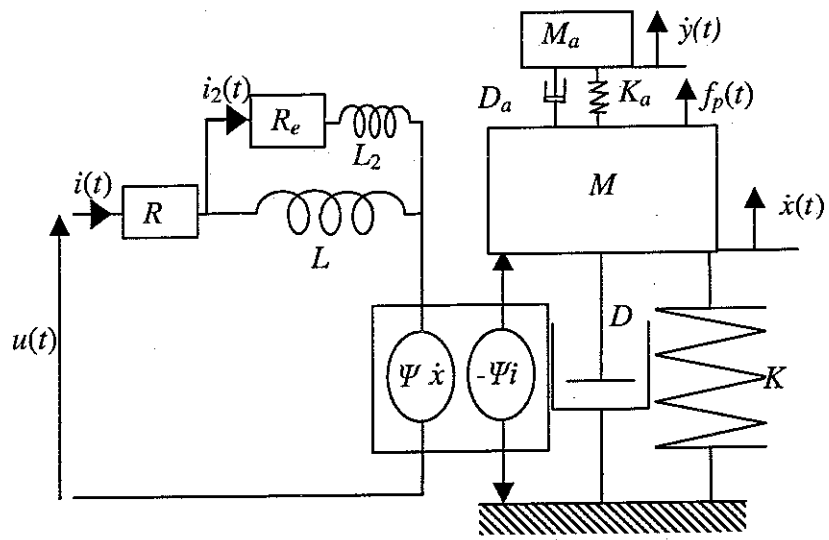

Figure B.1: *Fully coupled electrodynamic model with accelerometer and additional resistance modelling eddy currents in the ferro-magnetic core*

By considering eddy current losses in the magnetic core of the shaker with an additional resistance the correspondence between measurements and simulations can be enhanced at frequencies superior to the characteristic, electrical frequency, but the additional phase and amplitude increment at even higher frequencies shown in Figure B.2 cannot be explained. Still another additional zero seems to be necessary in order to model this behaviour. Furthermore even by changing parameters in a wide range the slope of the measured curve cannot be exactly reached.

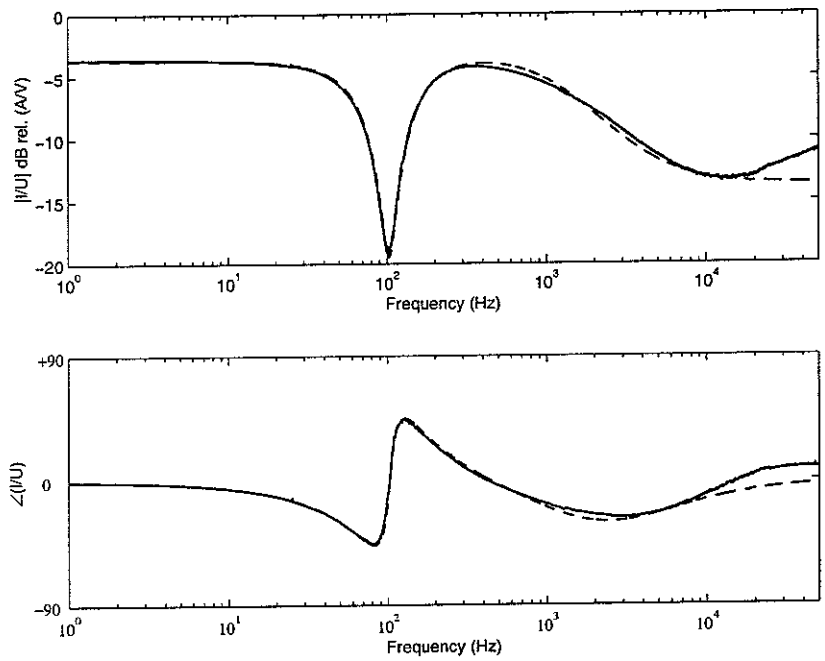

Figure B.2: *Bode plot of the measured (solid line) and simulated (dotted line) FRF between the source voltage and the coil current when considering eddy current losses in the core of the shaker, zoom between 0 and –20 dB*

The Nyquist plot in Figure B.3 of the same FRF also underlines that the simulated amplitude at frequencies between 500 and 1000 Hz should be lower than simulated and an additional capacitive part seems to be missing in order to simulate an additional 90 degrees phase shift. Nevertheless the inwards spiral of the measured locus can be simulated much better.

Table B.1: *Additional electrical parameters when modelling eddy currents*

Parameter		Value
Resistance due to eddy current losses in the ferromagnetic core	R_e	6.6 Ω
Line inductance	L_2	$2.62\ 10^{-10}$ H

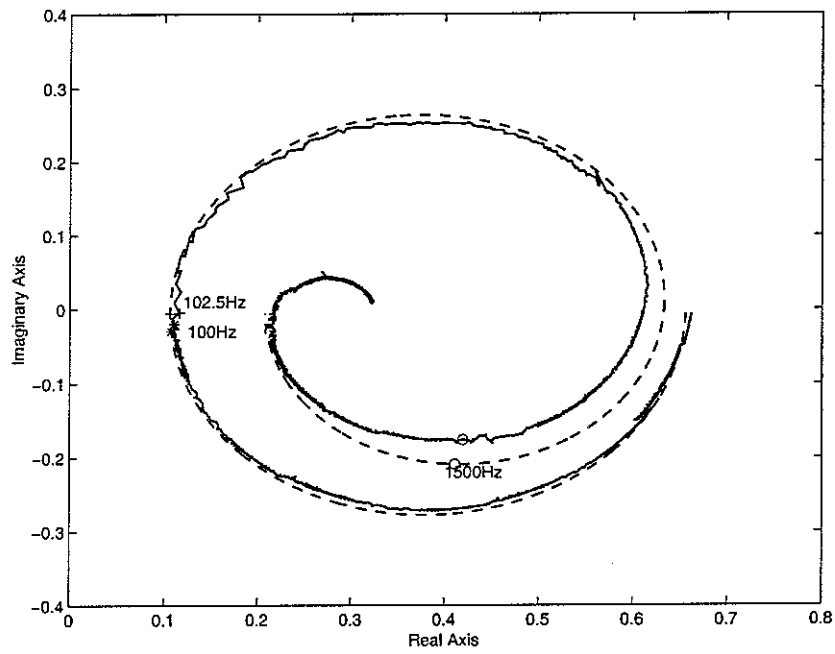

Figure B.3: *Nyquist plot of the measured (solid line) and simulated (dotted line) FRF between the source voltage and the coil current when considering eddy current losses of the ferromagnetic core*

An additional explanation for the additional lead effect at higher frequencies could be an additional capacitance associated to the measurement system. In [88] it is stated on page 205 : "This capacitance arises from the unavoidable self-capacitance of the coil winding and from the capacitance of the cable which connects the transducer to the indicator or to the electronic equipment, usually an amplifier." When actually adding a shunted capacitance C and a second inductance L_1 to the model in Figure B.1 an additional electrical resonance frequency appears at higher frequencies in simulations. Model equations for the model in Figure B.4 are

$$\mathbf{M}\begin{bmatrix}\ddot{y}\\ \ddot{x}\\ \dot{i}\\ \dot{i}_1\\ \dot{i}_2\end{bmatrix}+\mathbf{D}\begin{bmatrix}\dot{y}\\ \dot{x}\\ i\\ i_1\\ i_2\end{bmatrix}+\mathbf{K}\begin{bmatrix}y\\ x\\ q\\ q_1\\ q_2\end{bmatrix}=\begin{bmatrix}0\\ f_p\\ 0\\ u_d\\ 0\end{bmatrix} \tag{B.3}$$

where

$$\mathbf{M}=\begin{bmatrix}M_a & 0 & 0 & 0 & 0\\ 0 & M & 0 & 0 & 0\\ 0 & 0 & L & 0 & -L\\ 0 & 0 & 0 & L_1 & 0\\ 0 & 0 & -L & 0 & L_2+L\end{bmatrix}$$ is the generalized mass matrix,

$$\mathbf{D} = \begin{bmatrix} D_a & -D_a & 0 & 0 & 0 \\ -D_a & D+D_a & -\Psi & 0 & 0 \\ 0 & \Psi & 0 & 0 & 0 \\ 0 & 0 & 0 & R & 0 \\ 0 & 0 & 0 & 0 & R_e \end{bmatrix}$$ is the generalized damping matrix and

$$\mathbf{K} = \begin{bmatrix} K_a & -K_a & 0 & 0 & 0 \\ -K_a & K+K_a & 0 & 0 & 0 \\ 0 & 0 & \frac{1}{C} & -\frac{1}{C} & 0 \\ 0 & 0 & -\frac{1}{C} & \frac{1}{C} & 0 \\ 0 & 0 & 0 & 0 & 0 \end{bmatrix}$$ is the generalized stiffness matrix.

This model is used to derive equation (3.3) and the simulations in Figures 3.5 and 3.6 using additional parameters compiled in Table B.2.

Table B.2: *Electrical parameters when adding a capacitance*

Parameter		Value
Capacitance	C	$2.5\ 10^{-6}$ Fa
Line inductance	L_1	$1.179\ 10^{-5}$ H

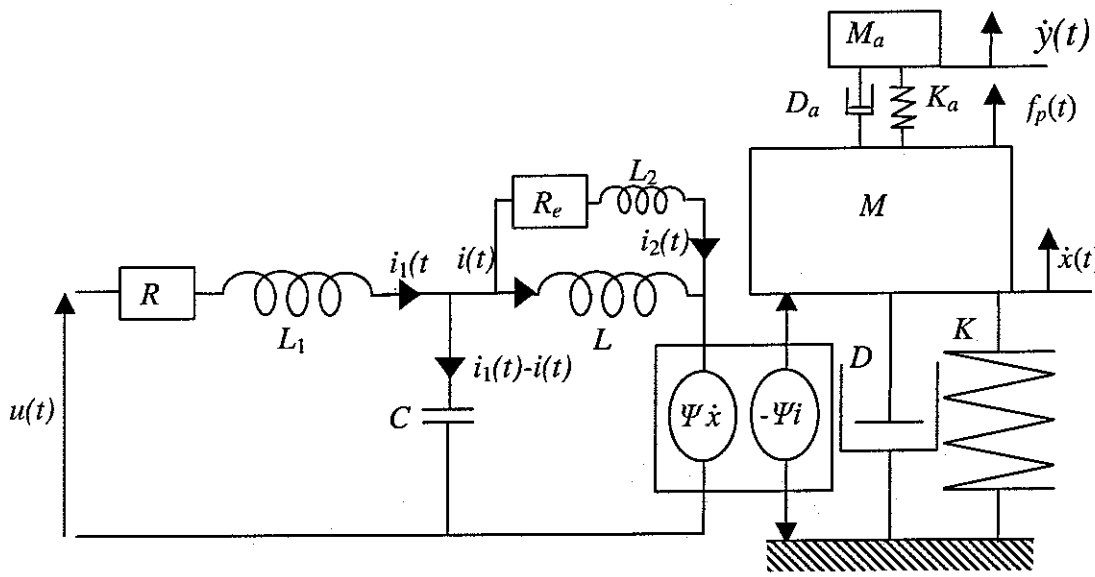

Figure B.4: *Fully coupled electromechanical model with accelerometer and capacitance and additional resistance modelling eddy currents*